NORTHWESTERN UNIVERSITY

Towards modeling closed-loop sensorimotor integration in tactile sensing systems

A DISSERTATION

SUBMITTED TO THE GRADUATE SCHOOL
IN PARTIAL FULFILLMENT OF THE REQUIREMENTS

for the degree

DOCTOR OF PHILOSOPHY

Field of Biomedical Engineering

By

Nadina Olivia Zweifel

EVANSTON, ILLINOIS

September 2022

**Abstract**

The current view in neuroscience holds that the brain, together with its sensory and motor structures and the environment, form a closed-loop system – a sensorimotor loop – in which the brain receives information from the environment and converts it into a motor response while simultaneously making predictions about future sensory events based on the current action. Thus, it is crucial to study the brain in the context of the animal's body and its ecological niche. However, conducting experiments in freely behaving animals is very challenging, and it is often impossible to measure the sensory information real animals acquire. Therefore, neuroscientists often break the loop between the sensory system and the motor system and replace the environment with controlled stimuli and motor tasks. This approach has major drawbacks, including impoverished stimuli and motor actions, forcing the brain to operate outside of its natural context, and breaking the external link between sensory and motor systems. This thesis attempts to address these limitations through simulation and modeling. First, we take a thorough look at the sensorimotor loop to examine how the flow of signals within the loop may affect the animal's ability to predict sensory consequences of motor actions for different modalities. We introduce more precise language to characterize the conceptual differences between "active sensing" modalities, and show that tactile sensing (touch) is unique and therefore especially well-suited to examine the sensorimotor loop. We then use this insight to develop a model of the rat vibrissal (whisker) system that allows us to simulate the complete vibrissotactile sensory input during active sensing behavior. Lastly, we take the first steps to characterize the environmental constraints imposed on the tactile sensorimotor loop. We use information theoretic methods to analyze the tactile statistics of three-dimensional objects and show that there are close similarities to the statistics of sensory inputs to other modalities such as vision and audition.

# Acknowledgment

First and foremost, I thank my advisor, Dr. Mitra Hartmann, for giving me the opportunity to join her lab and letting me discover the extremely diverse and fascinating research field of the rat vibrissal system – her passion for the field has inspired me since the beginning of my PhD program. Thank you for the freedom you have given me throughout the years which allowed me to explore many different aspects and subfields within neuroscience and engineering. Thank you for supporting me in pursuing my own ideas even if they might not have turned out fruitful at the end. Thank you for your confidence in me and encouragement during times I struggled and did not belief in myself and my research. Thank you for your patience that allowed me to acquire new knowledge and skills I could not have otherwise. Lastly, thank you for creating a friendly and supportive lab environment where I felt comfortable and appreciated throughout my PhD experience.

I thank my committee members for their interest in my research and guidance along the way. Especially, I want to thank Dr. Sara Solla who taught me so much in every meeting and for her patience and time to explain the most abstract and difficult problems in simple understandable ways. Besides for being an excellent mentor in science, thank you for your genuine interest in my well-being and your emotional support. I am so grateful that I had the opportunity to work with you more closely in the last two years of my PhD. I also want to thank Dr. Todd Murphey and Dr. Eric Perreault for their critical questions, constructive feedback and great ideas in every committee meeting.

I thank all my lab members Dr. Nick Bush, Dr. Admir Resulaj, Dr. Schnaude Dorizan, Dr. Hannah Janssen, Thomas Janssen, Yifu Luo, Kevin Kleczka, and Alec Lei for their knowledge and willingness to help whenever I needed it. Thank you for creating an environment that was always friendly and collaborative, and for all the fun nights with "Whiskey Whiskers" and Trivia. Special thanks go to Admir and Schnaude for sitting through many "Neuro-Lit" sessions dissecting lengthy papers about the vibrissal system with me. In particular, I would like to thank Alec Lei whose work is included in the discussion and appendix. You were a great mentee, and it was a great pleasure to work with you.

I thank my parents for supporting me in all my endeavors even if that meant moving across the Atlantic and leaving my family behind. I want to thank my mom for always believing in me and my decisions, giving me confidence, encouraging me in difficult times, and being always there for me when I needed emotional support. I want to thank my dad for taking such great interest in my research and career choices, supporting me financially such that my long student journey was possible, and visited me so many times during the years I have lived abroad.

Most importantly, I thank my best friend, partner, and now husband, for entering my life when I most needed it. First as a friend when I moved to Chicago and did not know a single soul, and then as a partner when the world shut down and isolated me from friends and family. Thank you for always being there for me, listening, supporting me, and for being the best partner in crime I could ever wish for.

Lastly, I thank my baby Silas who made working on my thesis the most difficult tasks ever. Thank you for your countless smiles, making me laugh every day, and reminding me that there are more important things in life than success and accomplishments.

**Table of Contents**

# List of Figures and Tables

# CHAPTER 1

## Introduction

The brain has been studied for many years at various levels – from neural circuits to molecules – and each day considerable data is gathered from all levels in dozens of species. And yet, researchers still struggle to understand brain function in organisms with the simplest of nervous systems (Randi and Leifer 2020).

Although technology and experimental methods have advanced at a rapid pace and new insights are gained every day, most experiments are still limited and often require great abstraction and simplification (Lewicki, Olshausen et al. 2014). Often, animals in experiments are anesthetized or constrained, are exposed to artificial stimuli, and neural recordings are often done in localized regions of the brain and only target a small subset of neurons. It is highly questionable whether such reductionist experimentation can provide the means to gain thorough understanding of the nervous system's inner workings (Lewicki, Olshausen et al. 2014, Krakauer, Ghazanfar et al. 2017).

The most prominent figure to voice this concern was Marr (Marr 1982), who advocated for a more holistic approach of neuroscience research. He suggested three levels at which the nervous system can be understood – the computational problem (computational level), the algorithm solving the problem (algorithmic level), and the physical implementation of the algorithm (implementation level) (Krakauer, Ghazanfar et al. 2017). According to Marr, and many others, it is essential to identify the actual problem the nervous system has evolved to solve to gain full understanding of brain functions (algorithms) and their neural implementations. Identifying such a problem often requires considering the biological and environmental context.

For example, "foraging" may seem a similar task across many species – identifying edible items in a cluttered world. However, the biological blueprint and ecological niche of each species is different and shapes the specific sensory and motor tasks required for the nervous system to solve the "foraging" task. On the one hand, the environment determines an animal's access to resources, and on the other hand, the biology and morphology of the body determines an animal's ability and constraints on acquiring sensory information and executing actions. Within these constraints, the sensory and motor systems serve as interfaces between the brain and the environment, forming a closed-loop system often referred to as the sensorimotor loop. Through this sensorimotor loop, the nervous system is in continuous interaction with body and environment, which in turn shape the neural circuitry, its function, and its physiology.

## 1.1 The sensorimotor loop

A long-standing classical view of the nervous system maintains that the sensorimotor loop is a one-way street. Environmental signals from the environment (light, sound, etc.) impinge on the animal's sensors, these signals are converted into a neural signal which then produce a motor command that executes an action within the environment. This does not explain, however, how the nervous system reliably learns to use available sensory signals to infer underlying environmental causes. Theories of predictive coding and Bayesian inference have suggested that the brain solves this problem by using expectations and prior beliefs to predict the environmental causes of sensory stimuli, evaluating these predictions based on the current sensory input, and then updating the expectations and prior beliefs accordingly (Blakemore, Goodbody et al. 1998, Rao and Ballard 1999, Engel, Fries et al. 2001, Friston, Kilner et al. 2006, Clark 2013). So, while the brain receives information from the environment and converts it into a motor response, it also simultaneously makes predictions about future sensory events based on the motor commands used

to perform an action. Deficits in such computation or inaccurate prior beliefs are thought to result in misinterpretations of sensory stimuli and possibly cause delusions and hallucinations that are symptomatic of various psychotic disorders including schizophrenia (Ford, Mathalon et al. 2001, Ford and Mathalon 2012, Adams, Stephan et al. 2013). For example, failing to correctly predict one's own vocalization may lead one to falsely attribute the auditory signal to others, resulting in auditory hallucinations (Ford and Mathalon 2012). Biased prior beliefs about the self may lead to distorted self-image and can cause depression, personality disorders, and paranoia (Moutoussis, Fearon et al. 2014). How each of the various levels of sensory processing, between elemental processing at the periphery (sensor level) and abstract computations in cortex, contributes to the brain's ability to reliably predict forthcoming sensory events is still unclear (Kaliuzhna, Stein et al. 2019).

The somatosensory (tactile) system is ideal to study the sensorimotor loop because tactile signals are themselves induced by the animal's movements. The rat vibrissal (whisker) system is especially well-suited because it involves a series of nested feedback loops that form a closed topology from the level of the brainstem up to the level of the cortex (Kleinfeld, Berg et al. 1999, Kleinfeld, Ahissar et al. 2006).

### 1.1.1 A model system for the sensorimotor loop: the rat vibrissal system

The rat vibrissal (whisker) system is ideal to study sensorimotor circuits because it heavily relies on sensor movement, because it has an extremely regular sensor arrangement that is easily traceable throughout the somatosensory pathway, and because the vibrissae themselves can be easily modeled due to their relatively simple mechanical structure. Rats explore their environment with their vibrissae by actively moving them back and forth several times per second (whisking) and tapping them against surrounding objects (Vincent 1912). Using their whiskers, rats have been

shown to be able to discriminate surfaces (Vincent 1912), roughness (Guicrobles, Jenkins et al. 1992), distance (Shuler, Krupa et al. 2002), and texture (Prigg, Goldreich et al. 2002), as well as localize and recognize objects (Brecht, Preilowski et al. 1997, Polley, Rickert et al. 2005). Each vibrissa is embedded in a follicle densely innervated by the primary afferents of trigeminal ganglion neurons (Vg), which transmit the mechanical signals that are generated in the follicle in response to bending and vibrations of the vibrissa (Vincent 1913).

There are roughly 60 distinct whiskers, 30 on each side of the rat's face, which are arranged in a grid-like manner (Towal, Quist et al. 2011). Each whisker is embedded in a follicle in the skin on the rat's face (Vincent 1913). When the whisker contacts an object, it is deflected and generates a mechanical response at the whisker base (Quist and Hartmann 2012, Quist, Seghete et al. 2014). These signals consist of translational forces and rotational moments that are detected by the mechanoreceptors in the follicle, transduced into a neural signal, and sent through the sensory pathway to higher brain structures (Diamond, von Heimendahl et al. 2008, Diamond and Arabzadeh 2013). At the same time, a motor pathway terminates in muscles that are wrapped around the follicle (Dorfl 1982). There are two groups of muscles, extrinsic and intrinsic muscles (Dorfl 1982); the intrinsic muscles are attached close to the mystacial skin and wrap around the base of the neighboring rostral vibrissa, whereas the extrinsic muscles attach externally to the pad with fibers distributed throughout the pad. Contraction of the intrinsic muscles protracts while the contraction of extrinsic muscles retracts the vibrissae (Berg and Kleinfeld 2003).

The sensory and motor pathways of the vibrissal pathway form many sensorimotor circuits, from small and fast reflex loops at the periphery to complex circuits involving multiple brain structures (Nguyen and Kleinfeld 2005, Mitchinson, Martin et al. 2007, Deutsch, Pietr et al. 2012, Sherman,

Oram et al. 2013, Matthews, Deschênes et al. 2015, Bellavance 2017), which allows the study of the sensorimotor loop at different levels of the brain.

A major drawback of using the vibrissal system as a model system is that the mechanical signals generated at the base of the whiskers cannot be measured directly. Any device small enough to mount on a rat's whisker would significantly alter the way the whisker moves and therefore the mechanical response at the whisker base. Therefore, researchers have used a variety of models to infer the moments and forces at the base of the whiskers (see next section).

### *1.1.1.1 Modeling the mechanical response at the whisker base*

Over the last three decades a variety of mechanical and dynamical models of the rat vibrissa have been developed (Lucianna, Albarracín et al. 2016). Most of these models are limited to two dimensions and choose a quasi-static approach to solve for the mechanical signals at the base of the whisker (Scholz and Rahn 2004, Birdwell, Solomon et al. 2007, Kim and Möller 2007, Boubenec, Shulz et al. 2012, Quist and Hartmann 2012). Only very few models consider the third dimension (Clements and Rahn 2006, Huet, Schroeder et al. 2015).

Although quasi-static models largely explain the forces and moments at the whisker base during collision with objects, they do not capture vibrations of the whisker that are assumed to play a significant role in texture exploration (Hipp, Arabzadeh et al. 2006, Diamond, von Heimendahl et al. 2008, Weber, Saal et al. 2013) or the signals generated during non-contact whisking. These limitations have motivated the development of several dynamical models (Neimark, Andermann et al. 2003, Boubenec, Shulz et al. 2012, Yan, Kan et al. 2013, Quist, Seghete et al. 2014, Vaxenburg, Wyche et al. 2018). All these models are two-dimensional. Studies have shown that the associated neurons respond to deflections of the whisker in all three directions, suggesting that

two-dimensional models are insufficient to describe fully the sensory signals generated at the whisker base (Simons 1978, Simons 1985, Jones, Lee et al. 2004, Hemelt, Kwegyir-Afful et al. 2010).

Modeling of the three-dimensional dynamics of the rat vibrissa is challenging for three reasons. First, the distributions of material properties within the whisker are poorly understood. The size and extreme aspect ratio of the vibrissa make it difficult to study their internal structures such as density and elasticity. Previous studies that tried to measure Young's modulus of rat whiskers directly with nanoindentation and uniaxial tensile tests yielded inconclusive results (Quist, Faruqi et al. 2011, Kan, Rajan et al. 2013). Other studies estimated the Young's modulus from deflection or bending resonance (Hartmann, Johnson et al. 2003, Neimark, Andermann et al. 2003, Birdwell, Solomon et al. 2007). This approach requires knowledge about the geometry of the whisker, which is typically approximated as a circular cone. However, the neglect of the intrinsic curvature of the rat vibrissa almost certainly contributes to the large variability of the results in these experiments.

Second, three-dimensional modeling is challenging because of the unique geometry of the whisker. Methods such as finite element analysis are likely to fail because the thin, narrow shape of the whisker causes singularities. Thus, most studies choose an analytical approach and view the whisker as a conical cantilever beam. This approximation often omits intrinsic curvature, which significantly affects forces and moments at the base (Knutsen, Derdikman et al. 2005, Knutsen, Biess et al. 2008, Quist and Hartmann 2012). Furthermore, during natural whisking behavior the vibrissae rotate out of the horizontal plane (Knutsen, Derdikman et al. 2005, Knutsen, Biess et al. 2008). The rotation about its own axis changes the orientation of the whisker with respect to the surrounding objects, affecting the vibrations and bending of the whisker during collision (Quist and Hartmann 2012).

Third, incorporating collisions into the model is complicated (Boubenec, Shulz et al. 2012, Quist, Seghete et al. 2014). The main function of whiskers is their mechanical response due to collision with surrounding objects but detecting and solving for collisions is analytically and computationally challenging, and typically results in a trade-off between model accuracy and computational efficiency.

### 1.1.1.2 Multi-whisker stimulation

One of the most prominent features of the vibrissal system is that topography is maintained throughout the neural pathway from periphery to the primary somatosensory cortex (barrels) (Woolsey and Van der Loos 1970). This invariance led researchers to study extensively the encoding of single whisker deflections. But early and more recent work has shown that single whisker deflection evoke activity across multiple barrels (Axelrad, Verley et al. 1976, Petersen and Diamond 2000, Ferezou, Bolea et al. 2006, Berger, Borgdorff et al. 2007), which suggests spatial integration of the sensory array. Although natural rodent whisking behavior has been shown to involve many whiskers, little is known about the multi-whisker computations performed in the barrel cortex (Hobbs, Towal et al. 2016).

One reason for this is the complexity of multi-whisker stimulation that requires multiple actuators to stimulate multiple whiskers simultaneously, a challenging task considering the geometry and scale of the whisker pad. But even with the most recently developed multi-whisker stimulators (Jacob, Le Cam et al. 2008, Jacob, Estebanez et al. 2010), it is questionable whether these stimulations can be considered as "natural," especially because they require head-fixed or anesthetized animals. While neural activity can be recorded in freely behaving animals, it is currently impossible to quantify the corresponding sensory input. These are significant limitations when studying neural circuitry that has evolved while using multiple sensors interacting with a

three-dimensional complex world. Behavioral studies have shown that natural rodent whisking behavior involves contact and collisions of many whiskers with the environment. Studies of the barrel cortex suggest that, despite the prevalent topology, neural information is spatially integrated across multiple whiskers, and that the statistics of the stimuli have a significant effect on the receptive fields due to adaptation mechanisms (Ramirez, Pnevmatikakis et al. 2014). These findings indicate that it is crucial to study neural activity in the vibrissal system in the context of natural behavior and the full whisker array.

## 1.1.2 The sensorimotor loop in the context of evolution

Because both the sensory and motor systems are in continuous interaction with the environment, their evolution is strongly driven by the statistics to which they are exposed. An example of coevolution of motor and sensory systems driven by environmental statistics is the spectral energy distribution of vocalization and hearing sensitivity in mammals. Research has shown that mammals living in forest environments produce vocal signals of higher frequency and have better high frequency hearing sensitivity than other terrestrial mammals (Charlton, Owen et al. 2019). These authors suggest that higher frequency vocalization and hearing sensitivity may constitute an advantage in forest environments, as they facilitate sound localization where visibility is poor (Charlton, Owen et al. 2019). A similar example is the concave-eared torrent frog that lives near small rapid streams in Southeast Asia. This species communicates often in the ultrasonic range, possibly to differentiate from the predominantly low-frequency characteristics of its environment (Feng and Narins 2008).

The competition under selection pressure drives the evolution of sensory and nervous systems to select relevant information efficiently in the context of the animal's ecological niche. Based on these assumptions, Barlow hypothesized that sensory pathways are relays, selecting and

transforming incoming information before it is passed on to other parts of the brain (Barlow 1961). He further asserted that the filtering properties of sensory systems must therefore be shaped by the statistics of the sensory input. Since this notion was brought forward, the analysis of natural scene statistics has proven to be a powerful tool to reveal relationships between sensory signals and neural representations (Laughlin 1981, Field 1987, Olshausen and Field 1996, Olshausen and Field 1997, Geisler, Perry et al. 2001, Simoncelli and Olshausen 2001, Lewicki 2002, Smith and Lewicki 2006, Geisler 2008, Geisler and Perry 2009, Hyvärinen 2010, Hausler, Susemihl et al. 2013, Burge and Geisler 2015, Samonds, Geisler et al. 2018).

### *1.1.2.1 Natural scene statistics*

In the early fifties, Attneave was one of the first to point out that redundancy in current sensory signals allows to predict future sensory signals (Attneave 1954). Examples for such redundancies in images are symmetry, homogeneity, or invariances that allow the observer to guess the rest of the image by knowing only a small portion of it. Furthermore, he asserted that most information is contained where predictions about future sensory stimuli are wrong (unexpected). Therefore, contours in images contain most information, and within these contours the information is most concentrated where the contours change most rapidly (Attneave 1954). Because the number of states sensory receptors can assume vastly exceeds the numbers of neurons available to the brain, Attneave (Attneave 1954), and later Barlow (Barlow 1961), suggested that an important role of sensory systems must be reduction of redundancies in the sensory signal. Laughlin tested this hypothesis and found that the responses of large monopolar cells (LMCs) of the fly's visual system are proportional to the cumulative probability distribution of contrast in natural images (Laughlin 1981). Thus, LMCs seem to perform histogram equalization which is consistent with an efficient

coding strategy in which the response range with highest resolution is used for the most frequent events (Laughlin 1981).

Following these findings, several studies examined the statistics of natural images and showed that pixel and contrast intensities of natural images are highly non-random, i.e., they are non-Gaussian, highly correlated, show high kurtosis, and are scale invariant, i.e., the amplitude spectra fall off by 1/frequency (Field 1987, Field 1993, Ruderman 1994). Many different algorithms for redundancy reduction, decorrelation, and optimal encoding to maximize information and reconstruction fidelity were proposed, including principal component analysis, Gabor filters, Gauss-Markov random fields, wavelets, and more (Maloney and Wandell 1986, Field 1987, Atick and Redlich 1992, Hancock, Baddeley et al. 1992, Field 1993, Field 1994, Dong and Atick 1995, Field 1999). The algorithm that received most attention and laid the groundwork for a series of research studies still relevant today was the sparse coding algorithm by Olshausen and Field (Olshausen and Field 1996, Olshausen and Field 1997). The algorithm was essentially a simple two-layer network that receives a small patch of an image, maps it onto an overcomplete set of unknown basis functions, and then reconstructs the image patch from the activation of those basis functions in a linear fashion (Olshausen and Field 1996). The network is trained under the constraint of sparse activations of the basis functions to match the non-Gaussian probability distributions found in natural images. When the network was trained on natural images, the basis functions that emerged were strikingly similar to the receptive fields found in the visual cortex, showing a oriented Gabor-like properties (Olshausen and Field 1996).

Following this study, natural scene statistics and efficient coding became widely used, and similar algorithms such as independent component analysis (ICA) were applied not only to natural images but also natural sound recordings (Bell and Sejnowski 1997, Van Hateren and Ruderman 1998,

van Hateren and van der Schaaf 1998, Hoyer and Hyvärinen 2000, Lewicki 2002, Karklin and Lewicki 2005, Smith and Lewicki 2006, Mlynarski and Jost 2014). However, only few attempts have been made to apply these algorithms to natural tactile scenes (Hafner, Fend et al. 2003, Hafner, Fend et al. 2004, Evans 2013). The challenge to measure natural scenes for tactile sensing is the complexity of measuring the sensory input. To date, it is not possible to measure the mechanical input to the mechanoreceptors in real humans or animals. Although  advances have been made in developing software that can simulate the mechanical input to the human hand (Saal, Delhaye et al. 2017) and the rodent vibrissal system (including chapter 3 of this thesis), lack of data in this field has significantly limited the study of natural *tactile* scenes.

## 1.2 Significance statement

As outlined in the previous sections, it is crucial to study the brain as a closed-loop system that includes the animal's body and its ecological niche. However, conducting experiments in freely behaving animals is very challenging, especially in natural environments, and it is often impossible to measure the sensory information real animals acquire. Therefore, neuroscientists often break the external loop between the motor system and the sensory system, and replace the environment with controlled stimuli and motor tasks. However, this approach has major drawbacks: (1) impoverished stimuli and motor actions, (2) the brain operates outside of its natural context, and (3) it also breaks the direct link between sensory and motor systems.

This thesis attempts to address these drawbacks by using simulation and modeling. The second chapter of this thesis takes a thorough look at the sensorimotor loop and examines how signal flow within the loop may impact the animal's ability to predict sensory consequences of motor actions for different modalities. Our analysis shows that "active sensing" may need more precise language to appreciate the conceptual differences between modalities. Furthermore, we show that tactile

sensing (touch) is unique and especially suited to examine the sensorimotor loop. The work in this chapter provides a theoretical framework to create and test hypotheses about different sensing strategies in simulation.

In the third chapter, we use this insight to develop a model of the rat vibrissal system that allows us to simulate the complete sensory input during active sensing behavior. To our knowledge, the tool presented here is the first to provide simulations that completely characterize the sensory input during naturalistic sensor movement. This allows researchers to generate large amounts of synthetic data for computational models, to understand behavioral data, and to generate input for neural models.

In the fourth chapter, we take the first steps to characterize the environmental constraints imposed on the tactile sensorimotor loop. Using information theoretic methods, we analyze the tactile statistics of three-dimensional objects and show that there are close similarities to other modalities such as vision and audition.

# CHAPTER 2

## Defining "active sensing" through an analysis of sensing energetics: homeoactive and alloactive sensing

Nadina O. Zweifel[1] and Mitra J. Z. Hartmann[1,2]

[1] Department of Biomedical Engineering, Northwestern University, Evanston, IL, 60208, USA
[2] Department of Mechanical Engineering, Northwestern University, Evanston, IL, 60208, USA

## 2.1 Abstract

The term "active sensing" has been defined in multiple ways. Most strictly, the term refers to sensing that uses self-generated energy to sample the environment (e.g., echolocation). More broadly, the definition includes all sensing that occurs when the sensor is moving (e.g., tactile stimuli obtained by an immobile vs. moving fingertip), and broader still, includes all sensing guided by attention or intent (e.g., purposeful eye movements). The present work offers a framework to help disambiguate aspects of the "active sensing" terminology and reveals properties of tactile sensing unique among all modalities. The framework begins with the well-described "sensorimotor loop," which expresses the perceptual process as a cycle involving four subsystems: environment, sensor, nervous system, and actuator. Using system dynamics, we examine how information flows through the loop. This "sensory-energetic loop" reveals two distinct sensing mechanisms that subdivide active sensing into *homeoactive* and *alloactive* sensing. In homeoactive sensing, the animal can change the state of the environment, while in alloactive sensing the animal can alter only the sensor's configurational parameters, and thus the mapping between input and output. Given these new definitions, examination of the sensory-energetic loop helps identify two

unique characteristics of tactile sensing: 1) in tactile systems, alloactive and homeoactive sensing merge to a mutually controlled sensing mechanism, and 2) tactile sensing may require fundamentally different predictions to anticipate reafferent input. We expect this framework may help resolve ambiguities in the active sensing community and form a basis for future theoretical and experimental work regarding alloactive and homeoactive sensing.

## 2.2 Introduction: the varying definitions of active sensing

The goal of this paper is not a comprehensive review of "active sensing," as there are already several review articles on this topic (Bajcsy 1988, Caputi 2004, Nelson and MacIver 2006, Schroeder, Wilson et al. 2010, Mitchinson, Grant et al. 2011, Prescott, Diamond et al. 2011, Hofmann, Sanguinetti-Scheck et al. 2013, Bajcsy, Aloimonos et al. 2017, Yang, Wolpert et al. 2018, Stamper, Madhav et al. 2019). Instead, the present work reviews the use of the term "active sensing" to demonstrate that its meaning has gradually become increasingly ambiguous, in part through implicit redefinitions across the fields of sensory neuroscience, computer science, robotics, and engineering (Kaneko, Kanayama et al. 1998, Konda and Tsitsiklis 1999, Mihaylova, Lefebvre et al. 2002, Wang, Veloso et al. 2016, Yang, Lengyel et al. 2016, Goeckel, Bash et al. 2017, Concha-Miranda, Rios et al. 2019, Leszczynski and Schroeder 2019, Uyanik, Stamper et al. 2019).

This paper identifies the various definitions of "active sensing" that have emerged over the years to highlight the broad and often contradictory use of the term. This ambiguous vocabulary is at odds with the precise language that science typically strives to develop. We therefore offer a proposed terminology based on system dynamics that captures the different aspects of active sensing as it is used across multiple fields.

It is useful to start by identifying three commonly used definitions of active sensing, shown in Table 2-1. The definitions include 1) the use of sensor movement, 2) sensing with intent, and 3) the emission of a self-generated signal. All three of these definitions have been widely used and discussed within and across different sensory modalities and in different fields (Bajcsy 1988, Caputi 2004, Nelson and MacIver 2006, Schroeder, Wilson et al. 2010, Mitchinson, Grant et al. 2011, Prescott, Diamond et al. 2011, Hofmann, Sanguinetti-Scheck et al. 2013, Bajcsy, Aloimonos et al. 2017, Yang, Wolpert et al. 2018, Stamper, Madhav et al. 2019).

**Table 2-1. Varying definitions of active sensing.**

|  | Active Sensing | Passive Sensing |
|---|---|---|
| **Sensor motion*** | sensor is moving | sensor is immobile |
| **Voluntary control over the sensing process** | purposeful/ intentional | *not* purposeful/ intentional |
| **Source of the energy for sensing** | self-generated | externally generated |

*The first definition is particularly relevant to the study of "tactile suppression," in which sensory signals throughout the somatosensory pathway are reduced in amplitude in the presence of movement (Chapman, Bushnell et al. 1987, Chapman 1994). Hence, purely physiological considerations mandate a distinction between the sensory signals acquired when the sensory surface is immobile (passive) from when it is moving (active).

One of the first records to make the distinction between passive and active sensing emerged in Jean-Atoine Nollet's 1743 article on "Leçons de physique expérimentale" (Nollet 1743). Nollet recognized that there is a distinct difference in the experience as well as the mechanism between "being touched" (passive) and "touching" (active). Taking a similar view, Steinbuch recognized that not only touch can be passive or active, but vision can be as well (Steinbuch 1811). Even in these very early days of sensory research, it was already appreciated that both modalities are composed of arrays of receptors which function, in principle, in similar ways (Steinbuch 1811).

Later in the 19th century, Helmholtz objected to the notion that sensory systems can be "passive," emphasizing that sensor motions, such as eye movements, play a crucial role in "observing" (Von

Helmholtz 1867). Helmholtz was one of the first researchers to view sensory systems as predictive engines, learning the physical laws that link (sensory) movements to sensory consequences (von Helmholtz 1879). Hence, he compared sensor movements to a set of ongoing "experiments" in which the animal continuously tests perceptual expectations against incoming sensory data. Helmholtz later elaborated this idea by including attention and intent as another form of changing sensory conditions. Thus, the mere redirection of focus, such as moving the fovea into a region of interest, becomes the means to test predicted changes in the sensory input (von Helmholtz 1879).

Wilhelm Wundt offered a similar perspective at the beginning of the 20th century; he defended the notion that sensing is *active* only when guided by attention and intent (Wundt 1902). According to Wundt, passive perception occurs when "the new content forces itself on the attention suddenly and without preparatory affective influences," whereas during active perception "attention is concentrated upon [new content] even before it arrives" such that "the content is preceded by a feeling of expectation" (Wundt 1902). In this sense, "active sensing" could – in principle – occur in the entirely immobile animal, provided the animal were actively attending to the sensory stimulus.

David Katz later adopted a similar definition, using the terms "active" and "passive" primarily in relation to sensor movement to distinguish between passive and active touch (Katz 1925). According to Katz, touch sensations favoring the "objective pole," typically associated with active touch including exploration and manipulation, are attributed to properties of external objects (e.g., the glass has a smooth texture, the book is rectangular). In contrast, touch sensations favoring the "subjective pole," typically associated with passive touch, are attributed to internal states, and remain essentially sensations.

Summarizing, even the earliest uses of the term "active sensing" confound movement with intent and purposefulness, the definitions in the first two rows of Table 2-1.

Interestingly, the views of James J. Gibson, one of the most influential figures in the history of sensory research, developed through similar stages. Many of his early ideas recapitulate those of Nollet, formulated over two hundred years earlier, and then the early 20th century work of Katz (Nollet 1743, Katz 1925, Gibson 1962). Gibson does not appear to have been aware of these similarities, likely due to language barriers (Wagner 2016).

In his 1950 work *Perception of the Visual World*, Gibson uses the word "active" to mean vision in the presence of head or locomotor motion (Gibson 1950). By 1962, however, in *Observations on Active Touch*, he had mostly, though not entirely, migrated to a view in which "active" touch was used to identify those conditions in which the animal controlled the process of information acquisition. Regrettably, and as previously noted by Loomis and Lederman (Loomis and Lederman 1986), Gibson did not use the terms "active" and "passive" touch consistently. Sometimes he indicated that "passive touch involves only the excitation of receptors in the skin and its underlying tissue…," while other times he distinguished between active and passive touch based on the presence or absence of motor control of the exploratory movement (Gibson 1962). In other words, Gibson also confounds the definitions in the first two rows of Table 2-1.

At other points in his writing, Gibson dismissed the idea that perception can be passive at all. In agreement with Helmholtz, he supported the notion that perception always required exploratory movement to extract information by collecting invariants over time, regardless of modality (von Helmholtz 1879, Gibson 1976). Since then, this view has been widely supported by strong evidence that eye movement is a critical part of the visual perceptual process (Girard and Berthoz

2005, Schroeder, Wilson et al. 2010, Schütz, Braun et al. 2011, Coubard 2013, Leszczynski and Schroeder 2019). Similarly, pinnae and head movements play an important role in auditory perception, and sniffing is critical to olfactory perception (Bremen, van Wanrooij et al. 2010, Schroeder, Wilson et al. 2010, Lefevre, Courtiol et al. 2016, Risoud, Hanson et al. 2018).

In contrast to his predecessors, however, Gibson forgoes using the words "purposeful" or "intentional" in any of his discussions of active perception. Instead, he explicitly describes exploratory sensor movement to be "purposive" (Gibson 1950, Gibson 1962). This word choice ("purposive" instead of "purposeful") is interesting because he thereby deliberately includes the possibility of visceral actions being part of a sensing process, which do not necessarily require the observer's awareness, will, or intent.

Between the publications of Katz (1925) and Gibson (1966), the fields of radar and sonar developed rapidly (Mason 1962). In this engineering context, the term "active sensing" was redefined to distinguish between self and externally generated energy, as shown in the third row of Table 2-1. For example, active sonar systems "ping" the environment by emitting a signal and analyzing the returning echoes, while passive auditory systems only receive acoustical energy. Similarly, depth maps can be estimated either through "passive scanning" using cameras or "active scanning" using profilometry (Kaller, Bolecek et al. 2016).

In the field of biology, this specific use of the term was adopted to describe electroreception in fish, as well as echolocation in bats and dolphins, i.e., the term was sometimes narrowly redefined to include only those sensations caused by the animal's own self-generated signal. In this view, passive sensing refers to sensations elicited by external sources (Bullock 1973). This definition of "active sensing" was first applied to bats in Pye (1960) and to dolphins in Dubrovskii (1976).

Curiously, though as we will see not surprisingly, this definition was also extended to include rat whisking behavior and perhaps some hand movements, which raises the question: why do scientists have the intuition that somehow whisking and fine finger movements should be grouped with the self-emitted energy of bats, dolphins, and electric fish?

Work in robotics and artificial intelligence in the late 1980's called out the difference between active and passive sensing in terms of control and energy emission as listed in the second and third rows of Table 2-1 (Bajcsy 1988, Ballard 1991). These authors were clear that although a narrow definition of "active sensing" uses self-generated energy, it "should be axiomatic" that perception is active, not passive. Simila Helmholtz and Gibson, they see perception as an exploratory process that requires probing and searching the environment. Therefore, even a "passive" sensor (one that does not emit, but only receives energy) can be used in an active fashion, e.g., by purposefully changing sensor parameters according to the sensing strategy. For example, Ballard carefully chooses to use the term "animate vision" instead of "active sensing," because the latter term had already been used for laser range finders (Ballard 1991).

A recent theoretical perspective took steps towards refining the definition of "active sensing" by describing perception as a closed-loop convergence process (Ahissar and Assa 2016). This perspective suggests, first, that most sensory organs are linked to motor circuits through closed brain (sensorimotor) loops, and therefore all modalities are typically "active"; and, second, that natural "passive" sensing exists only within a sufficiently short time window before the sensorimotor loop can be closed, i.e., sensing is passive only when motor components are functionally eliminated (Horev, Saig et al. 2011).

Although this perspective highlights important aspects of the sensing process, it does not differentiate between two categorically distinct sensing mechanisms that animals use to obtain sensory information from the environment: (1) an animal can sample the environment by actively changing the sensor configuration to modify the relationship *between* the sensor and the environment; or (2) by emitting a probing signal to change the sensory signal *in* the environment (Caputi 2004). Using option (1) often means the expense of mechanical energy, which is – with the exception of touch – "different" in form from the sensory energy acquired. For example, mechanical energy is expended to move the eyes, but electromagnetic energy is detected by the retina. In contrast, option (2) requires the animal to emit a signal of the "same" type of energy as the energy that is detected by the sensor. For example, an electric fish emits electromagnetic energy, and its electric organ also senses electromagnetic energy.

To summarize, the term "active sensing" has been redefined and reinterpreted several times over the past two hundred years. In the present work, we offer a framework based on system dynamics to define and explore these two fundamentally different sensing mechanisms. We differentiate between *alloactive* sensing, which actively changes the sensor configuration, without changing the state of the environment; and *homeoactive* sensing, which alters the state of the environment, without necessarily changing the configuration of the sensor.

We first formulate the framework in terms of dynamical systems with some illustrative examples. We then show that, when examined in this framework, the sense of touch exhibits several distinct characteristics that set it apart from all other sensory modalities. Finally, we demonstrate that considerations of reafference indicate physiological and computational differences between *alloactive* and *homeoactive* sensing that should not be simply summarized under a universal term such as "active sensing."

## 2.3 Reformulation of the "sensorimotor loop" in terms of subsystems and energetic channels.

Several previous studies have described the perceptual process as a continuous "sensorimotor loop" involving four main components: environment, sensor, nervous system, and actuators (Neisser 1976, Geisler 2008, Friston, Daunizeau et al. 2010, Ahissar and Assa 2016). For example, Geisler's four domains of natural scenes statistics are referred to as environmental properties, sensory signal, neural response, and behavioral response (Geisler 2008). Similarly, Ahissar and Assa's closed-loop perception process is described by environmental states, sensory, neural, and motor variables (Ahissar and Assa 2016). Similar quantities are used in theories such as the free energy principle: external states, sensations, internal states, and actions (Friston, Daunizeau et al. 2010).

Although this sensorimotor loop is universal across sensory modalities, each modality employs different forms of energy (Caputi 2004). For example, some systems extract information from light (electromagnetic energy) or sound waves (acoustical energy), whereas others respond to electrical fields (electrical energy) or chemical stimuli (chemical energy). Mathematically, one can relate this energy to the integral of the squared magnitude of the signal; for a time-varying signal $\boldsymbol{y}(t)$, the energy within a time window of length $T$ is of the form:

$$\boldsymbol{E} \sim \int_0^T |\boldsymbol{y}(t)|^2 \, dt \qquad \text{(eq. 1)}$$

From this perspective, sensory systems use different *energetic channels* to interact with the environment, and animals have evolved specialized sensors and neural circuitry to facilitate, and presumably optimize, information flow in these channels (Barlow 1961). Across the different sensory modalities, we identify five possible channels: visual (light), acoustical (sound), mechanical (movement), electrical, and chemical (e.g., bioluminescence or odor).
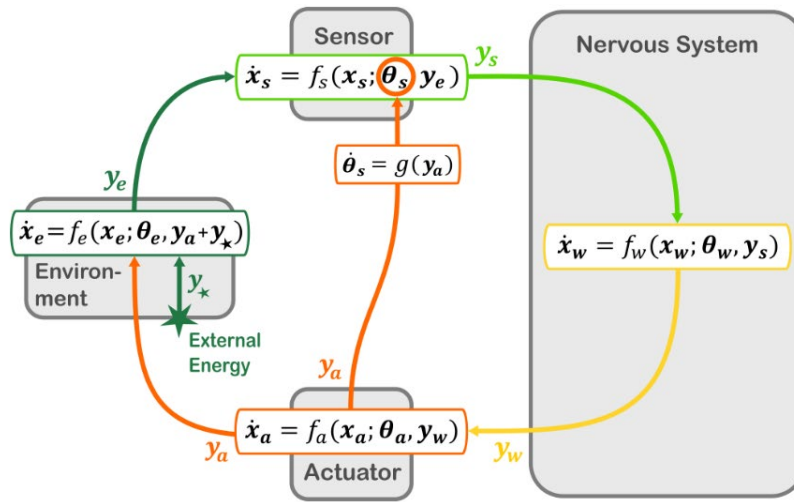
**Figure 2-1. The sensory-energetic loop described in terms of system dynamics.** The sensory-energetic loop is composed of four subsystems: environment, sensor, nervous system, and actuator (grey boxes). In the colored boxes, the differential equations for the evolution of the environmental state ($x_e$; dark green), the sensory state ($x_s$; light green), the neural state ($x_w$; yellow), and the actuator state ($x_a$; orange) are given. The subsystems are connected by channels, through which signals ($y_e$, $y_s$, $y_w$, $y_a$) are sent from one subsystem to the next. In addition, external energy $y_\star$ (green star) might be generated in the environment (by natural phenomena or by the animal). The variable $\dot{x}_e$ is the time derivative of state $x_e(t)$, and the function $f_e(.)$ is the transform function parameterized by $\theta_e$ representing the physical properties of the associated subsystem, in this case the environment. The output signal of the system $y_e$ $(= y_e(t))$, serves as input to the subsequent system in the loop. The same principle applies to the subsystems of sensor, nervous system, and actuator. The orange arrow originating from the actuator and connecting to the sensor indicates that certain actuators can manipulate sensor configurations $\dot{\theta}_s = g(y_a)$, where $g(.)$ describes the relationship between the actuator signal and the caused change in the sensor parameters $\theta_s$.

Within each channel, signals carrying the information pass through each of the four subsystems associated with the sensorimotor loop (environment, sensor, nervous system, and actuator), which transform and route the signals between channels. Because the information flow depends on the sensory mechanism and the used energetic channels, we will refer to it as the *sensory-energetic loop*, described in the next section. We will show that sensing mechanisms express two distinct

energy streams (routes) through the sensory-energetic loop that clearly subdivide "active" sensing into *homeoactive* and *alloactive*.

The cyclic nature of the sensory-energetic loop, and the interdependency between the states of environment, sensor, nervous system, and actuator is best described in terms of dynamical system theory (Arbib 1989, Kiss 1991, Beer and Gallagher 1992, Beer 1997). Accordingly, we can model the sensory-energetic loop as four connected subsystems representing the environment, sensor, nervous system, and actuator (Figure 2-1, grey boxes). The states of the subsystems are denoted as $x_e$, $x_s$, $x_w$, and $x_a$, respectively. Note that none of the four subsystems are considered autonomous, nor is the larger system, which is composed of the four subsystems. The output of each subsystem ($y_e$; dark green arrow, $y_s$; light green arrow, $y_w$ ; yellow arrow, and $y_a$; orange arrow) is connected to the input of the subsequent subsystem, forming a loop for each energetic channel (chemical, electrical, acoustical, visual, and mechanical). Note that bold variables are vectors, summarizing all five channels in a single variable. Consequently, the time evolution of the sensor can be expressed as a dynamical system:

$$\dot{x}_s = f_s(x_s; \boldsymbol{\theta}_s, y_e) \qquad \text{(eq. 2)}$$

where $\dot{x}_s$ is the time derivative of state $x_s(t)$, and $f_s(.)$ describes the function that determines the time evolution of the sensor state (Figure 2-1, light green box). The function $f_s(.)$ is the transform function of the sensor and is parameterized by $\boldsymbol{\theta}_s$, representing the physical properties (material properties, geometry, configuration, etc.) of the sensor. Examples of such sensor parameters are the orientation angle of the eyes or pinnae, the protraction angle or spread of a whisker array, or the body shape of a weakly electric fish. The input signal to the sensor, and therefore to the function $f_s(.)$, is the output signal $y_e$ ($= y_e(t)$) of the previous system, the environment.

The equations for nervous system, actuator, and environment are analogous and shown in Figure 2-1 as yellow, orange, and dark green boxes, respectively. If there is another energy source in the environment (star), the emitted energy $y_\star$ from that source is added to the input signal $y_a$ to the environmental subsystem.

Some of the sensory parameters ($\boldsymbol{\theta}_s$) can be manipulated through specific actuators. For example, extraocular muscles can generate eye movements to change the angle of the eyeballs with respect to the head. Such manipulations of the sensor configuration are achieved through mechanical energy by activating the appropriate muscles. Action resulting in a change of sensory parameters ($\dot{\boldsymbol{\theta}}_s = g(y_a)$) is indicated by the orange arrow branching off from the actuator and connecting to the parameters of the sensor (orange circle).

A more detailed example of the sensory energetic loop is provided in Figure 2 for both homeoactive and alloactive sensing. Figure 2A illustrates the sensory-energetic loop for the case of the auditory system of an owl searching for prey in the environment. The loop begins with an external signal $y_\star$ (blue star) which serves as input to the environmental system. The term "external signal" means a signal from a subsystem separate from the animal, such as prey generating a sound or noise. How this external signal affects the state of the environment $x_e$ depends on the function $f_e(.)$, parameterized by the properties $\boldsymbol{\theta}_e$ associated with that particular environment. For example, an environment of rocks and boulders will reflect and absorb vibrations very differently than will a forest. The output signal $y_e$ represents the vibrational energy available for the owl to acquire with its auditory system in that environment.
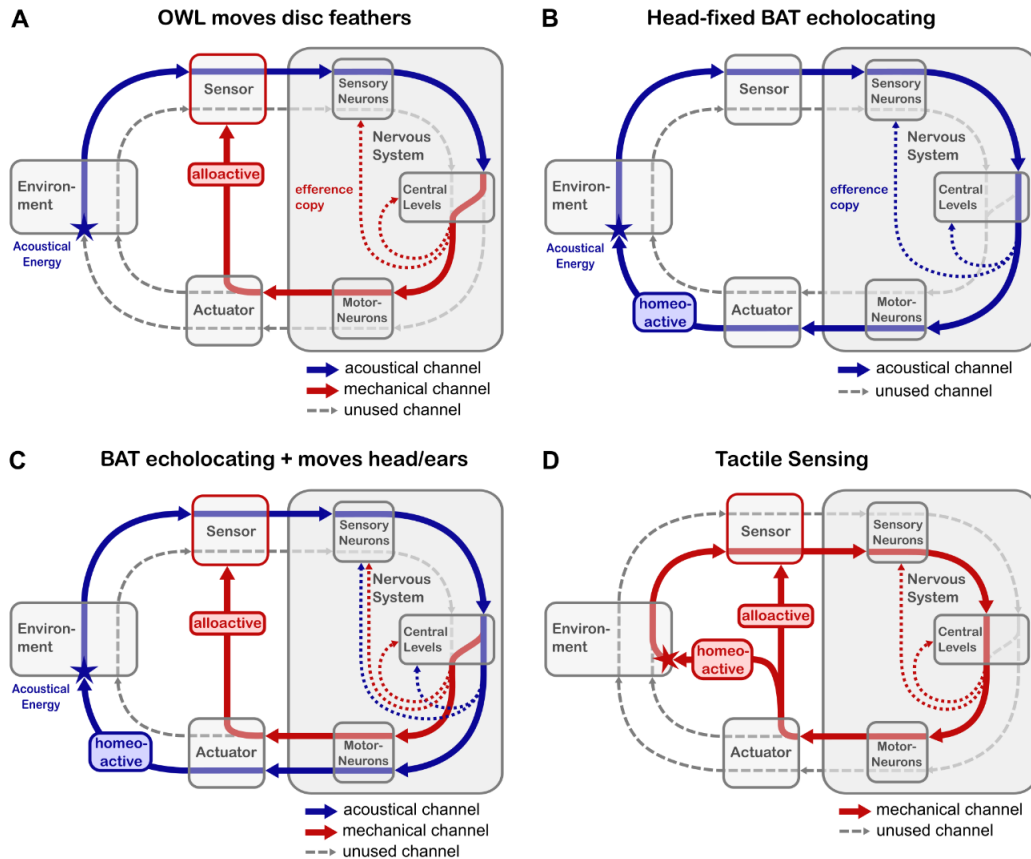
**Figure 2-2. Illustration of the sensory-energetic loop for alloactive and homeoactive sensing.** **(A)** Alloactive sensing as performed by an owl moving its disc feathers to manipulate the configuration of its sensors ($\theta_s$) (red arrow), which changes the mapping between sensor input and output, and consequently the sensor state ($x_s$). As indicated by the blue star, the acoustical signal sensed by the owl is generated by an external energy source (e.g., noise from another animal), and it is then transformed by the environment and the sensor (blue arrow) before it is routed to the mechanical channel by the nervous system to manipulate the sensor parameters. **(B)** Purely homeoactive sensing as performed by an echolocating bat without head or pinna movement emitting acoustical energy (sonar calls) into the environment, and thus changing the state of the environment ($x_e$). In this case, acoustical energy is emitted as well as received (blue arrow). **(C)** Homeoactive sensing combined with alloactive sensing. Homeoactive sensing remains the same as in (B), indicated in blue. In addition, the bat uses mechanical energy to move its head or ears towards a point of interest (red arrows) and thereby perform alloactive sensing. **(D)** Tactile sensing in the sensory-energetic loop, as when exploring an object with the fingertips or hand. The red arrows indicate the flow of mechanical energy, which is generated by the sensor movement. Thus, the actuator signal, which is used to move the sensor (alloactive branch), is also partially injected into the environment as a result of contact with the object (homeoactive branch; star). This diagram shows that tactile sensing merges homeoactive sensing and alloactive sensing.

The loop continues as the environmental signal $y_e$ enters the owl's sensors changing the sensory state $x_s$ determined by the function $f_s(.)$. In this case the parameters $\theta_s$ are the geometric, morphological, and material properties of the owl's facial disc and ears. These organs collect and filter the environmental signal to produce the sensory output $y_s$ delivered to hair cells in the owl's ear. Next, receiving $y_s$ at its input, the owl's nervous system changes its state $x_w$ and puts out the neural signal $y_w$ according to $f_w(.)$. The parameters of the nervous system $\theta_w$ include all properties related to the hair cell receptors, neural connections, neurotransmitters, neuromodulators, and synaptic weights. Finally, the state $x_a$ of the owl's facial muscles, i.e., its actuators, takes as input the neural signal $y_w$ and produces the actuator output $y_a$, which adjusts the feathers of the owl's facial disc.

The muscle movement changes the shape of the facial disc and thus its focal length for sound received at the owl's ears. In other words, the actuator signal changes the properties of the sensors, i.e., $\dot{\theta}_s = g(y_a)$, as indicated by the red arrow in Figure 2-2A. Changing $\theta_s$ in turn changes the mapping $f_s(.)$ between the input signal, i.e. the output signal of the environment $y_e$, and the output signal of the sensor, $y_s$. The process of changing $\theta_s$ so as to change the mapping between $y_e$ and $y_s$ is what we define as *alloactive* sensing. Note that the red arrow bypasses the environmental system and that the loop ends at the sensor parameters.

Now consider a head-fixed echolocating bat operating in the same environment as the owl (Figure 2-2B). The sensory-energetic loop is nearly the same, but in this case, the bat's vocal actuators generate acoustical energy (blue star) that contributes as an input to the environmental system (blue). The mapping of $f_e(.)$, which includes absorption, reflection, scattering, etc. of the bat's emitted sonar calls, describes how the bat can modify the state of the environment $x_e$ and

consequently the signal $y_e$ received at its sensors (echoes). This form of actively changing $x_e$ is what we define as *homeoactive* sensing. Note that, unlike alloactive sensing, homeoactive sensing forms a closed loop.

## **2.4 Remarks on homeoactive and alloactive sensing**

Having now distinguished these two sensing methods, alloactive and homeoactive, the following remarks can be made.

*(1)* Although homeoactive sensing does not directly change the configuration $\boldsymbol{\theta}_s$ of the sensor, it is nearly always combined with alloactive sensing, which does change $\boldsymbol{\theta}_s$. For example, bats adjust the orientation of their heads and pinnae during echolocating behaviors, as diagramed in the sensory-energetic loop of Figure 2-2C. Acoustical energy is released into the environment by the bat's emitted sound and received back by the ear (homeoactive), and $\boldsymbol{\theta}_s$ is changed as muscles move the bat's head and ears (alloactive). In contrast, vision is usually entirely alloactive, since most animals cannot generate light to illuminate a visual scene; an exception is deep sea fish that can emit light to sense their prey (Douglas, Partridge et al. 1999). More generally, all animals use alloactive sensing, while only some species have evolved mechanisms for homeoactive sensing. One could also argue that sensory systems using homeoactive sensing are a subset of sensing systems using alloactive sensing, as similarly argued by Caputi (2004).

*(2)* If an alloactive system senses external energy but the sensor does not move, then the system is no longer active, but functions as a purely passive sensor, analogous to the definition in Ahissar and Assa (2016). For example, the visual system can sense light, even if the eye is immobilized. This definition is in line with the first row of Table 2-1.

*(3)* Although homeoactive sensing modalities do not depend on an external energy source, they certainly can sense such sources. For example, bats can sense sonar calls from conspecifics, and electric fish can sense discharges from adjacent fish (Ulanovsky, Fenton et al. 2004, Tan, Nizar et al. 2005, Bates, Stamper et al. 2008, Stamper, Carrera et al. 2010, Hase, Kadoya et al. 2018, Beleyur and Goerlitz 2019, Yu, Hupe et al. 2019).

*(4)* There are sensing strategies that may not be as obvious as audition or echolocation. For example, a very special sensing technique is used by the blind mole-rat (*Spalax ehrenbergi*), which uses "head drumming" (thumping the head against the tunnel roof) to produce seismic waves, that then are sensed through tactile sensors on the paws (Heth, Frankenberg et al. 1987, Kimchi, Reshef et al. 2005). This sensing strategy allows the animal to locate and estimate size, shape, and density of obstacles, such as stones and ditches. By emitting mechanical energy (seismic vibrations) and detecting the returning seismic "echoes" (closing the sensory-energetic loop), the mole uses homeoactive sensing.

*(5)* As shown in equation 1, the use of the term "energy" implies some integration time of the signals under consideration. The examples above have implicitly assumed that this time window is the duration required to complete one cycle of the sensory-energetic loop, which occurs during the interval between two consecutive actions. For example, a cycle in the visual system may start with the completion of a saccade and end with the initiation of the next (~ 300 ms). In the whisker system, a cycle might be initiated with a protraction of the whisker array and completed with the subsequent retraction (~ 125 ms for rats). At this time scale, energetic phenomena and the associated signals can vary greatly, while the system parameters typically change at a much slower rate (several seconds or more) and are therefore assumed to be constant within one cycle. In the framework of Ahissar and Assa (2016), multiple cycles through the sensory-energetic loop would

be needed before perceptual convergence could be achieved. For example, it has been shown that the rat vibrissal system requires approximately four whisk cycles (i.e., four cycles of the sensory-energetic loop) to converge to a stable percept (Horev, Saig et al. 2011).

## 2.5 The unsolved problem of attention and intent

Intuitively, audition may be viewed as alloactive, because the energy that the animal senses originates from an external source, and the animal's actuators can only change the parameters of the sensors (see the example of the owl in Figure 2-2A). However, even non-echolocating animals can technically use their ability to generate noises to extract information about the environment. For example, you can clap your hands and then use returning echoes to obtain a sense of room size (Schenkman 2017). This type of sensing represents homeoactive sensing because the acoustical energy emitted is also received by the auditory system.

Importantly, however, whether an animal has generated a noise as part of a communication process, or as part of homeoactive sensing, may be completely invisible to an outside observer, especially if the animal has immobile pinnae. It is only the animal's intention or attention that varies. Unless the animal is simply incapable of emitting the form of energy required to allow homeoactive sensing (e.g., vision for nearly all animals), intent and attention remain ambiguous to an external observer.

Ambiguity about the animal's intention may be an edge case for audition. Conscious human echolocation is not common, and only a few nonhuman primate species have been observed to use self-generated sound to locate food, a behavior also called "percussive foraging" (Erickson 1995, Phillips, Goodchild et al. 2004). But the problem of intent is highly relevant for somatosensation (Hartmann 2009). Why is the term "active touch" generally considered to include searching for

your keys in your pocket, but not to include locomotion? Both behaviors involve continuous, muscle-driven stimulation of tactile sensors in contact with the environment to guide ongoing movement.

Gibson addressed this problem by categorizing locomotion as "sense of support," dissociating it from (passive or active) touch (Gibson 1962). He argues that it is clearly different from touch and simply plays the role of a stable reference frame for any sensory information acquired (Gibson 1962). By adding a new category for locomotion, Gibson implicitly recognized that the only distinction between the two behaviors is intent: the intent of searching for keys is to acquire tactile information (a sensory goal), while the intent of locomotion is to change position (a movement, or displacement goal) (Hartmann 2009).

## 2.6 The role of efference copy and prediction

Efference copy mechanisms have been found across many species (Schuller 1979, Blakemore, Goodbody et al. 1998, Poulet and Hedwig 2003, Chapman and Beauchamp 2006, Kilteni, Andersson et al. 2018, Kilteni, Houborg et al. 2019) and have been suggested to play an important role in generating internal forward models to predict the sensory consequences of executed actions (Blakemore, Goodbody et al. 1998, Brooks, Carriot et al. 2015, Brooks and Cullen 2019). The distinction between alloactive and homeoactive sensing made in the present work allows us to reconsider the role of efference copy and prediction in perception.

We observe that during alloactive sensing the forward models and efference copies for sensory prediction are limited to reconfiguration of the sensor, typically in the form of movement (e.g., head movement, eye movement, …). The sensor reconfiguration is indicated by the dashed red arrows in Figure 2-2A. Without the history of the incoming sensory signals, these internal models

must be completely naïve to any changes occurring in the environment (e.g., a moving object, sounds from other animals, etc.). Only through memory of previously encountered sensory events can the nervous system learn models of the external world and predict its evolution over time.

In homeoactive sensing, on the other hand, which uses a self-generated signal to probe the environment, the brain has direct access to the environmental variables that in alloactive sensing can be only inferred from experience. Since the energy that is sensed is not externally generated but emitted by the animal itself, an efference copy of the energy causing the sensory input is available (Figure 2-2B; dashed blue arrows). That animals use this information to predict the sensory input has been shown in bats and weakly electric fish (Schuller 1979, Bell 1982). In the bat, for example, recordings in the interior colliculus have shown that some sensory neurons are sensitized by corollary discharge during vocalization (Schuller 1979). Schuller also discovered that the sensitivity of collicular neurons is adjusted to the frequency range of the expected returning echoes accounting for the Doppler shift. These results suggest the use of a forward model of the environment and executed actions and that they affect the emitted sensory signal.

Moreover, during homeoactive sensing, the animal has full control over the frequency content, duration, and amplitude of the emitted energy, allowing the sensory system to maximize the signal-to-noise ratio and the information obtained from the environment (Caputi 2004). Previous work has shown that bats modulate frequency and duration of their calls in response to the information acquired in the environment (Moss and Surlykke 2010), and that weakly electric fish modulate frequency and amplitude of the electric discharge in the presence of conspecifics (Henninger, Krahe et al. 2018).

Consequently, we conclude that alloactive and homeoactive sensing systems may rely on different sets of internal models and predictions that can be used by the nervous systems to extract information from the environment.

## 2.7 Tactile sensing: a special form of homeoactive sensing

The sense of touch (tactile sensing) exhibits two characteristics unique among all sensory modalities. First, homeoactive and alloactive sensing are merged and do not function independently. Second, the internal forward models for the prediction of tactile input may be conceptually different from other modalities using homeoactive sensing.

Unlike echolocation and electroreception, tactile systems do not generate a radiating probing signal that propagates away from the animal into the environment (one exception is the blind mole-rat; see section 4, remark 4). Instead, the motion of the animal's sensory surfaces generates a reaction force the environment (although it might be very small), and this reaction force is itself the probing signal (Caputi 2004). In other words, every time the actuator energy ($y_a$) moves the sensor (changes $\theta_s$), the motion itself injects mechanical energy into the environment ($x_e$), which the sensor itself then ultimately senses. In this way, tactile systems are the only sensory systems that merge homeoactive sensing and alloactive sensing to a mutually controlled sensing mechanism. This also implies that tactile sensing can only sense pure external movement entirely passively, because as soon as the tactile sensors begin to move, the sensing is also homeoactive.

Returning to the predictive aspects of sensing, we speculate that because homeoactive sensing is almost invariably used in conjunction with alloactive sensing, it typically requires an additional forward model to account for the sensory consequences of the emitted energy (dashed blue arrows in Figure 2-2C). In tactile systems, however, our analysis of the sensory-energetic loop illustrated

in Figure 2-2D implies that tactile systems would only need to learn one model, since the homeoactive and alloactive energy streams are tightly coupled and the sensory consequences are the same for both.

This insight may help provide an answer to the question posed in the introduction: scientists often have the intuition that fine finger movements and rodent whisking, including texture sampling (Ritt, Andermann et al. 2008, Wolfe, Hill et al. 2008, Jadhav, Wolfe et al. 2009, Schwarz 2016), should be grouped with the self-emitted energy of bats, dolphins, and electric fish because the fundamental types of predictions made in these tactile systems are homeoactive.

## 2.8 Conclusion

We have presented a framework that models the information flow through the environment, sensor, nervous system, and actuator as coupled dynamical subsystems in order to examine the mechanisms by which active sensing systems operate. This "sensory-energetic loop" shows that active sensing systems contribute to the information flow in two distinct ways: alloactive and homeoactive sensing. Alloactive sensing uses mechanical energy to change the configuration (parameters) of the sensor without changing the state of the environment. Homeoactive sensing, on the other hand, adds energy to the environment without necessarily changing the sensor configuration.

We showed that the two ways of sensing describe distinct sensing strategies, and that each must have evolved its specialized neural circuitry. We therefore strongly encourage the field to adopt the new terminology presented here, so as to emphasize the behavioral and physiological differences between homeoactive and alloactive sensing. The need for more precise language to describe the two types of "active sensing" is clearly illustrated in literature that has used the term

"active sensing" to indicate homeoactive sensing and "active sensing strategy" or "reafferent sensing" to indicate alloactive sensing (Caputi 2004, Hofmann, Sanguinetti-Scheck et al. 2013).

We are not the first to point out the important differences between the two sensing mechanisms we call alloactive and homeoactive. For example, Caputi (2004) uses the example of the weakly electric fish, to show that "active sensing" and "reafferent sensing" are two possible strategies the brain may use to constrain the large solution space of the ill-posed sensory inverse problem (i.e., the problem of inferring the environmental causes of sensory stimuli by having access only to excitation patterns at the sensory surface). He shows that "reafferent" (alloactive) sensing modifies the sensory input through active and exploratory movement and thereby reduces ambiguity by selecting a subspace of solutions. Conversely, "active" (homeoactive) sensing emits the energy (e.g., sound) used to sense instead of relying on external energy (e.g., light), and thereby takes control over the signal that carries the sensory information. Modulation of the emitted signal allows the nervous system to select regimes that are less cluttered or interfered by conspecifics (Caputi 2004).

In our description of the sensory-energetic loop based on system dynamics, we hope to provide a definition that appreciates the dynamic nature of animal-environment interaction typical for homeoactive and alloactive sensing. The formulation of the sensory-energetic loop not only makes the definition concrete, it also provides the means for future modeling (Beer 1995, Herrmann 2001, Warren 2006, Catenacci Volpi, Quinton et al. 2014, Sussillo 2014) and hypotheses to test about the advantages and disadvantages of the two sensing mechanisms and possible selection pressures that might have given rise to the evolution of each.

# CHAPTER 3

## A dynamical model for generating synthetic data to quantify active tactile sensing behavior in the rat

Nadina O. Zweifel[1], Nicholas E. Bush[2], Ian Abraham[3], Todd D. Murphey[3], Mitra J.Z. Hartmann[1,3]

[1] Department of Biomedical Engineering, Northwestern University, Evanston, Illinois, 60208
[2] Interdepartmental Neuroscience Program, Northwestern University, Evanston, Illinois, 60208
[3] Department of Mechanical Engineering, Northwestern University, Evanston, Illinois, 60208

## 3.1 Abstract

As it becomes possible to simulate increasingly complex neural networks, it becomes correspondingly important to model the sensory information that animals actively acquire: the biomechanics of sensory acquisition directly determines the sensory input and its subsequent neural processing. Here we exploit the tractable mechanics of the well-studied rodent vibrissal ("whisker") system to present the first model that can simulate the signals acquired by a full sensor array actively sampling the environment. Rodents actively "whisk" ~60 vibrissae (whiskers) to obtain tactile information; this system is ideal to study closed-loop sensorimotor processing. The simulation framework presented here, *WHISKiT Physics*, incorporates a realistic morphology of the rat whisker array to predict the time-varying mechanical signals generated at each whisker base during sensory acquisition. Single whisker dynamics are optimized based on experimental data, and then validated against free tip oscillations and dynamic responses to collisions. The model is then extrapolated to include all whiskers in the array, incorporating each whisker's individual

geometry. Simulation examples in laboratory and natural environments demonstrate that *WHISKiT Physics* can predict input signals during various behaviors, in scenarios currently inaccessible in the biological animal. In one example of the use of this model, results suggest that active whisking increases in-plane whisker bending compared to passive stimulation, and that principal component analysis can reveal the relative contributions of whisker identity and mechanics at each whisker base to the vibrissotactile response. These results highlight how interactions between array morphology and individual whisker geometry and dynamics shape the signals that the brain must process.

## 3.2 Introduction

The nervous system of an animal species co-evolves with its sensory and motor systems, through which the animal is in continuous interaction with the environment. Because these sensorimotor and environmental feedback loops are so tightly linked to neural function, there has been increasing effort to study neural processing within the context of the animal's body and environment (e.g., in the fields of neuromechanics and embodied cognition). However, it is challenging to collect neurophysiological data under naturalistic conditions, and thus simulations have become an increasingly important component of neuroscience. A wide variety of software platforms have been developed to enable simulations of neural populations and circuits (Hines and Carnevale 1997, Bowers, Beeman et al. 2000, Gewaltig and Diesmann 2007), the biomechanics of motor systems (Delp, Anderson et al. 2007), and the responses of sensory receptors (Wohrer and Kornprobst 2009, Cessac, Kornprobst et al. 2017, Saal, Delhaye et al. 2017, Okorokova, He et al. 2018, Huckvel 2019). To date, however, no system has been able to fully account for the physical constraints imposed during active sensory acquisition behavior in a natural environment.

Here we describe a novel simulation framework (*WHISKiT Physics*) that can model the dynamics of a complete sensory system – the rodent vibrissal array – operating under ethologically relevant conditions. The rat vibrissal array is one of the most widely used models to study active sensing and cortical processing in neuroscience. Although its biomechanics are relatively simple, the vibrissal array subserves a rich and complex repertoire of tactile sensing behavior. As nocturnal animals, rats are experts in using tactile cues from their whiskers to extract information from the environment, such as object distance (Brecht, Preilowski et al. 1997, Krupa, Matell et al. 2001), orientation (Polley, Rickert et al. 2005), shape (Vincent 1912, Brecht, Preilowski et al. 1997), and texture (Guicrobles, Jenkins et al. 1992, Prigg, Goldreich et al. 2002). During tactile exploration rats often use active, coordinated oscillatory movements of their whiskers (whisking) to sample the immediate space at frequencies between 5-25 Hz (Berg and Kleinfeld 2003). These unique properties make this sensory system ideal to examine the dynamic relationship between motor control and sensory input during goal-directed and exploratory behavior.

A total of approximately 60 whiskers are regularly arranged on both sides of the rat's face (mystacial pad) (Brecht, Preilowski et al. 1997). Each whisker is embedded in a follicle where the mechanical signals generated at the whisker base are transduced by a variety of mechanoreceptors before they enter the sensory (trigeminal) pathway (Patrizi and Munger 1966). Thanks to the clear whisker-based topographic maps reflected in central structures (Woolsey and Van der Loos 1970) and its parallels to human touch (dorsal column-medial lemniscal pathway), the entire pathway – from the primary sensory neurons, through brainstem and thalamus, up to primary somatosensory cortex – has been the subject of extensive research. Nonetheless, to date the field has lacked the ability to simulate such a system operating under naturalistic conditions (i.e., the full whisker array, active control of whiskers, etc.).

*WHISKiT Physics* incorporates a 3D dynamical model of the rat vibrissal array to allow researchers to simulate the complete mechanosensory input during active whisking behavior. The model incorporates the typical shape and curvature of each individual whisker as well as the morphology of the rodent's face and the arrangement of the whiskers on the mystacial pad. Each whisker can be actuated either according to equations of motion for whisking (Knutsen, Biess et al. 2008) or to directly match behavioral data. The simulation environment permits direct control of whisker motion and simultaneous readout of mechanosensory feedback; *WHISKiT Physics* thus enables closed-loop simulations of the entire somatosensory modality in the rat, the first of its kind in any sensory modality. After validating models of individual whiskers in the array against several independent datasets, we use the full-array model to simulate vibrissotactile sensory input in four typical exploratory scenarios, both in the laboratory and in the natural environment, and discuss its use in future neural simulation systems. Each of the four scenarios generates unique patterns of data, illustrating that the model could be used to reveal the mechanisms that allow animals to extract relevant information about their environment. Although results are presented for the rat, they are easily extended to include the mouse.

## 3.3 Results

*WHISKiT Physics* is based on the Bullet Physics Library (Erwin and McCutchan 2008), an open-source physics engine with increasing contributions to game development, robotic simulation, and reinforcement learning (Erez, Tassa et al. 2015). This engine provides our model with reasonable computational efficiency, the ability to model natural environments based on 3D polygon meshes, and visualization of the simulations.

We aimed to model the complete rat vibrissal array, which typically consists of ~60 whiskers, 30 on each side. The whiskers are organized in a grid-like manner on the mystacial pad, in 5 rows (A-

E) and 7 columns (1-6). Whiskers in the "zero" column are typically labeled with Greek letters (α, β, γ, δ); the remaining columns are assigned their numerical values (1 – 6). The organization for an average rat whisker array is schematized in Figure 3-1a. The whisker geometry changes systematically with the whisker's row and column identity, and can be determined by using previously established equations (Belli, Yang et al. 2017, Belli, Bresee et al. 2018). For example, the side and top views of the array in Figure 3-1a (left) illustrate that the arc length of the whisker increases from rostral to caudal, while the curvature decreases. The radius slope of the whisker (i.e., its taper), which depends on its base and tip diameter as well as on its arc length, also decreases from rostral to caudal (Belli, Yang et al. 2017). The whisker's taper is not illustrated in this figure, but is included in the model.

### 3.3.1 Resonant frequencies with optimized material parameters generalize across whisker identities

Before constructing the model of the full rat vibrissal array, we developed a model of a single-whisker (Section 3.6.1 ; Figure 3-7) and optimized its elastic and damping parameters based on experimental data (Section 3.6.2 ). The optimization yielded values of $\theta_E = 5.0$ GPa and $\theta_\zeta = 0.33$, for elastic and damping parameters, respectively (Section 3.6.3 ; Figure 3-8), However, because the geometry of the whiskers varies so widely, it is not at all clear that these parameters will generalize over all whiskers and all geometries. We therefore quantified how well the model generalized over all whiskers in the array, without reoptimizing any parameters.

Using the optimized values for elasticity and damping, we quantified model performance against an experimental dataset that characterized the geometry and resonances of 24 whiskers from a single rat (Hartmann et al., 2003; Dataset S1, source 1). The linear fit between predicted and measured resonant frequencies yields a slope of 1.0 and an intercept of -31 Hz (solid line; Figure

3-1b). The slope of this fit closely matches that obtained from an analytical resonance model, which had a slope of 0.93 and an intercept of 6.4 Hz (Hartmann, Johnson et al. 2003).

Model validation was then extended to incorporate additional experimental data for which only partial geometric and resonance information was available (Dataset S1). The study of Wolfe et al. (2008) extends the dataset by 22 whiskers (δ, D1, D2, D3, D4) from four different rats (Wolfe, Hill et al. 2008). Neimark et al. (2003) provides the resonance frequencies of 10 whiskers of the C-row (left and right), measured both *in vivo* and *ex vivo* (Neimark, Andermann et al. 2003). Because lengths for these whiskers were not published, we estimated them from the equations of Belli et al. 2017 (Belli, Yang et al. 2017). Resonance values for the entire dataset are plotted in the left panel of Figure 3-1c. Note that measurement condition (*in vivo* vs. *ex vivo*) is associated with a large spread in the measurements; these differences provide an intuition for the error range associated with experimental data. Based on the inverse relationship between resonant frequency and whisker length, we fit a negative power function and obtained the model: $y = 8963\, x^{(-1.4)} - 3.8$ with $r^2 = 0.91$ (solid line). The 95% prediction intervals are shown as dashed lines.

Based on this experimental fit, we validated the resonance response across all whiskers of the full array, using average geometry (arc length, base diameter, slope) for each whisker identity as predicted by the models of Belli et al. (Belli, Yang et al. 2017). The whisker identities incorporated in the model are color coded in Figure 3-1a. The right panel of Figure 3-1c illustrates that the resonance frequencies of the averaged whiskers (colors consistent with Figure 3-1a) are well within the prediction intervals obtained from the experimental data in the left panel (dashed lines). In addition, these resonance frequencies do not significantly differ from the resonance frequencies obtained from simulations using the actual geometry shown in Figure 3-1b (2-sample t-test: p=0.93).
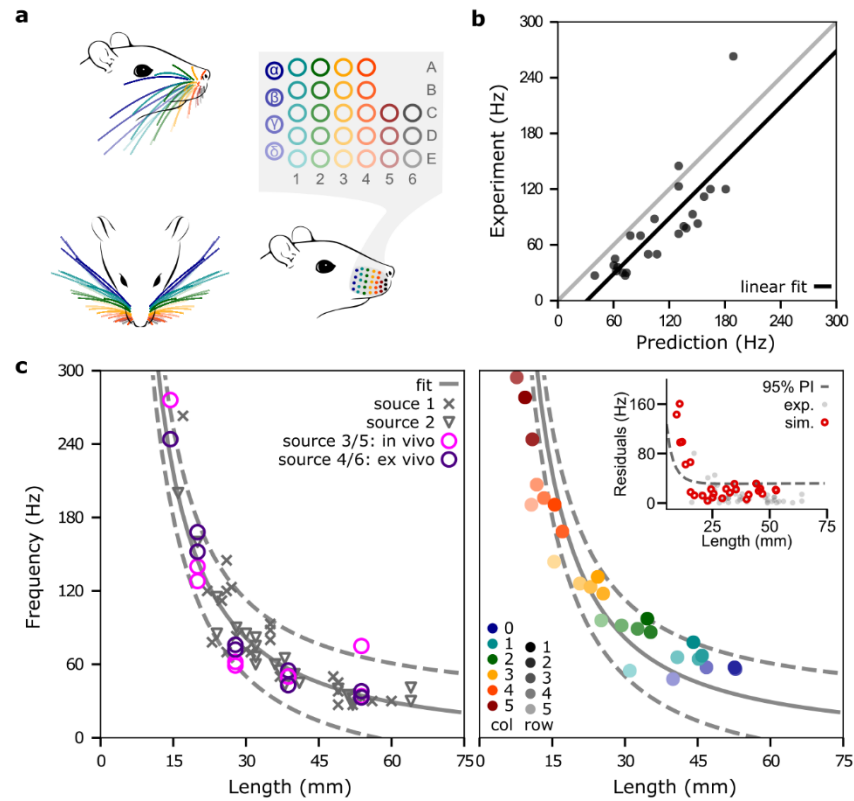
**Figure 3-1. The optimized model of the single whisker generalizes across the array. (a)** The whisker array of an average rat is organized in rows (A-E) and columns (1-6). The whiskers in column "0" are typically denoted by Greek letters (α, β, γ, δ). The side and top view of the array (left) show that the geometry of the whiskers changes considerably depending on the whisker's row and column identity. **(b)** Predicted resonance frequencies from Hartmann et al. (Hartmann, Johnson et al. 2003) (Dataset S1, source 1). Predictions were obtained from simulations that used the experimentally measured arc length and base/tip diameter. The gray line represents y = x. **(c)** The relationship between whisker length and resonance frequency obtained from experimental and simulated data. *Left panel*: Experimentally measured resonance frequencies of the combined dataset from three laboratories including a total of 46 whiskers (Dataset S1). The grey solid line indicates the nonlinear fit (y = 8963 x$^{(-1.4)}$ − 3.8), while the dashed lines indicate the corresponding prediction intervals. *Right panel*: Simulated resonance frequencies of average whiskers for all whiskers on the right side of the array (27 whiskers; left side is identical), color coded by whisker row and column identity. The solid and dashed gray lines are the nonlinear fit and prediction intervals shown in the left panel. *Inset*: Residuals of experimental (grey) and simulated (red) resonance frequencies of the nonlinear fit. The dashed line indicates the prediction interval.

The residuals of the regression model in Figure 3-1c reveal that only whiskers shorter than 15 mm (typically column 5 and higher) fall outside of the prediction intervals (inset). This error is primarily attributable to the high stiffness and small size of these whiskers, which are challenging to simulate. However, note the large deviation in high frequency measurements and sparsity of data points (Figure 3-1c; left), which also contribute to the mismatch between experimental data and simulation results. The whiskers in the most rostral column (column 6) are the smallest in the array and have extremely high resonance frequencies (> 250 Hz) (Hartmann, Johnson et al. 2003, Neimark, Andermann et al. 2003), which lead to large simulation errors. Therefore, this column was omitted from the model (Figure 3-1a; column 6). These whiskers have the lowest probability of making contact with objects during exploratory behavior (Hobbs, Towal et al. 2015, Hobbs, Towal et al. 2016), and thus their removal is not a significant limitation on the model's utility.

### 3.3.2 Dynamic collision behavior matches experimental results for straight and curved whiskers

The results above validate model dynamics during motions of the whisker that do not involve contact. To test the model under conditions of contact and in collision scenarios, we compared it with an analytical model and with experimental data published previously (Boubenec, Shulz et al. 2012). The analytical model of a straight whisker suggests that the mechanical response to a collision event scales with the collision's velocity, while experimental data indicates that the associated deformation wave propagates approximately linearly from tip to base (Boubenec, Shulz et al. 2012).

We selected 12 whiskers from four different rows (A, B, C, D) from the model shown in Figure 3-1 and tested their collision response. To replicate the scenario used to test the analytical model of collision (Boubenec, Shulz et al. 2012), we first simulated each whisker without curvature, as

anchored at its base and rotated it with constant velocity about the vertical axis through the base point until the 19th link (95% of whisker length from the base) collided with a rectangular edge. The collision angle between the whisker and the edge was set to 60° from the horizontal plane, and 45° degrees from the vertical plane to generate mechanical responses in all three dimensions (see schematic in the bottom right of Figure 2a). We simulated collisions at six different speeds.

We then repeated the simulation experiments for the same whiskers but including their intrinsic curvature, as illustrated in Figure 3-1a. One of the main advantages of the present numerical model is the ability to include intrinsic curvature, a whisker feature expected to have a significant influence on the mechanical response at the base during collision (Quist and Hartmann 2012).

Figure 3-2a shows $\dot{M}_z$, the derivative of the moment at the base about the rotation axis for both a straight and curved α whisker, from 5 ms before to 30 ms after collision. In both cases, the first negative peak of $\dot{M}_z$ (shock, $\dot{M}_{z,max}$) occurs ~3 ms after collision, and its magnitude clearly increases with velocity. These results are consistent with analytical solutions of a single straight whisker model (Boubenec, Shulz et al. 2012). We then measured $\dot{M}_{z,max}$ for all trials and whiskers. For each whisker, $\dot{M}_{z,max}$ was normalized by its mean value across the six different-speed trials. This normalization allowed us to compare trends across all 12 whiskers. Figure 3-2b shows the normalized $\dot{M}_{z,max}$ value as a function of angular speed at time of collision. $\dot{M}_{z,max}$ correlates with speed, achieving an adjusted $r^2$ of 0.92 for both straight and curved whiskers. However, the slopes of the regression lines are significantly different (p<0.001).
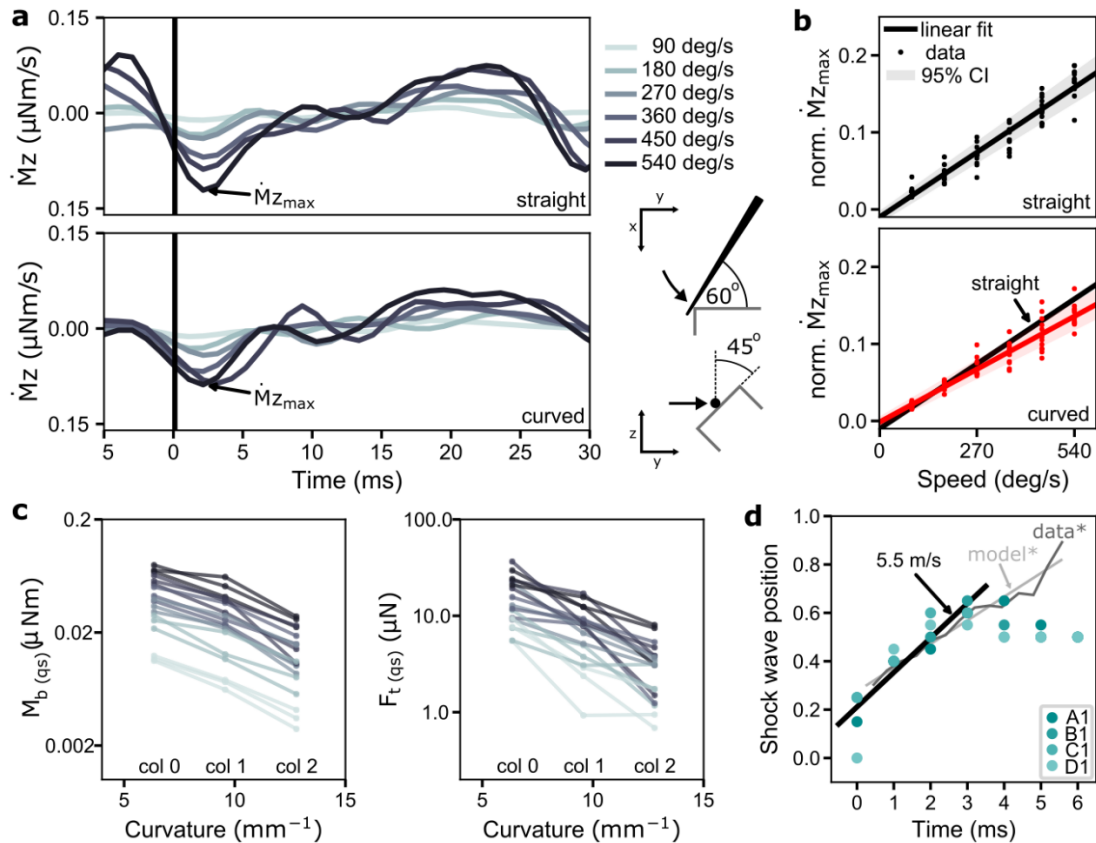
**Figure 3-2. Deformation waves resulting from collisions of straight and curved whiskers against a straight edge. (a)** Mechanical response of a straight and curved whisker in response to a collision. The derivative of the moment at the base of the α-whisker is shown for six different whisker speeds (90, 180, 270, 360, 450, 540 deg/s; color coded). Trials are aligned at time of impact (black line). An illustration of the top and side view of the corresponding experiment is given at the bottom right. **(b)** Relationship between normalized amplitude of the shock ($\dot{M}_{z,max}$) and whisker velocity for 12 straight and 12 curved whiskers (α, A1, A2, β, B1, B2, γ, C1, C2, δ, D1, D2). Linear fit for straight whiskers is represented by a black solid line (95% confidence interval shaded in grey). Note that the slope of the two regression lines is significantly different between straight and curved whiskers. **(c)** Bending moment $M_b$ and transverse force $F_t$ at the time of the shock ($\dot{M}_{z,max}$) versus the curvature of the whisker. Note that $F_t$ and $M_b$ are averaged over the first 30 ms after collision, representing quasi-static (qs) measures. The slope of the linear regression curve is significant for $M_b$ ($r^2 = 0.307$, $p < 0.001$) as well as for $F_t$ ($r^2 = 0.467$, $p < 0.001$). **(d)** Position of maximum deformation normalized to whisker length for whiskers A – D of the first column in the array. The value 0.0 thus represents the tip while 1.0 represents the base of the whisker. A linear fit to the first 4 ms is shown with a solid line and reveals a slope of 5.5 m/s. The light and dark grey lines illustrate the analytical (model*) and experimental (data*) results of Boubenec et al. (Boubenec, Shulz et al. 2012), respectively.

The decrease in $\dot{M}_{z,max}$ for curved whiskers can be explained by the negative correlation between curvature and the transverse force ($F_t = \sqrt{F_y^2 + F_z^2}$) and between curvature and the bending moment ($M_b = \sqrt{M_y^2 + M_z^2}$) at the whisker base (Figure 3-2c). This nearly-linear inverse relationship between the quasi-static mechanical signals at the base and curvature matches predictions from a previous quasi-static numerical model (Quist and Hartmann 2012).

Figure 3-2d shows the position of the maximum deformation (deformation wave) relative to the normalized whisker length within the first 6 ms after collision for 4 whiskers (first 4 rows, first column). A linear regression was performed on the first 4 data points after collision. The slope is significant ($r^2 = 0.90$, $p < 0.001$) and corresponds to a deformation wave velocity of 5.5 m/s, close to the analytical solution of 5.6 m/s and experimentally measured deformation wave velocity of 5.02 m/s (Boubenec, Shulz et al. 2012). The analytical (model*) and experimental (data*) results from Boubenec et al. (Boubenec, Shulz et al. 2012) are illustrated in light and dark grey, respectively. Boubenec et al. found the deformation wave propagation to be linear within the first 6 ms after collision. We attribute the non-linearities in our model after 3 ms to the reduced spatial resolution of the whisker and increasing stiffness towards the whisker base. We found similar results for the Greek column, with a deformation wave velocity of 4.3 m/s ($r^2 = 0.97$, $p < 0.001$).

### 3.3.3 Mechanical signals across the full rat vibrissal array

The organized morphology of the array plays an important role in shaping tactile input (Hobbs, Towal et al. 2015, Hobbs, Towal et al. 2016, Hobbs, Towal et al. 2016). *WHISKiT Physics* incorporates this morphology (Belli, Bresee et al. 2018) to permit simulation of the complete mechanosensory input to the system. The rat vibrissal system, as is the case for human touch, is an *active* sensing system, in which sensing typically occurs in conjunction with context-dependent,

finely controlled sensor movements. To incorporate this essential property in the model, each whisker is actuated at its base, allowing for rotation in three dimensions (pro-/retraction, elevation, and roll). The protraction angle is controlled by the user, while elevation and roll follow from the equations of motion for typical whisking behavior (see *Methods*, section 3.5.4 , eq. 4-5). These choices permit us to simulate passive stimulation (no protraction; Figure 3-3a and Figure 3-3b), stereotyped whisking behavior (equation-based protraction Figure 3-3c and Figure 3-3d), and data-based whisking (e.g., tracking whisker motions from behavioral data). Examples for passive stimulation and equation-based whisking in laboratory and natural environment are given below; an example of simulating whisker motions from tracked behavioral data is available on Github (https://github.com/SeNSE-lab/whiskitphysics).

Figure 3-3 compares the tactile signals of the rat vibrissal array in four scenarios. In Scenario 1 (Figure 3-3a), a vertical peg is simulated to brush through the center of the immobile array. The peg moves at constant speed (0.3 m/s) from rostral to caudal. Scenario 2 (Figure 3-3b) is similar to Scenario 1, but instead of a single sweep through the entire array, the peg oscillates back and forth between its start and end position (in the middle of the array) to repeatedly stimulate the array eight times per second (8Hz). This scenario was carefully designed to replicate as closely as possible the stimulation distances, velocities, and frequencies associated with active whisking (Scenario 3). Scenario 3 (Figure 3-3c) simulates active whisking against a fixed, vertical peg. Each whisker is driven at its base according to established kinematic equations for whisking motion (Knutsen, Biess et al. 2008). One cycle of protraction and retraction of the array lasts 125 ms, equivalent to a whisking frequency of 8 Hz. The peg is positioned laterally, 20 mm from the midline of the head with an offset of 10 mm from the nose tip. Finally, in Scenario 4 (Figure 3-3d), the whiskers perform the identical whisking motion as in Scenario 3, but the array is positioned in
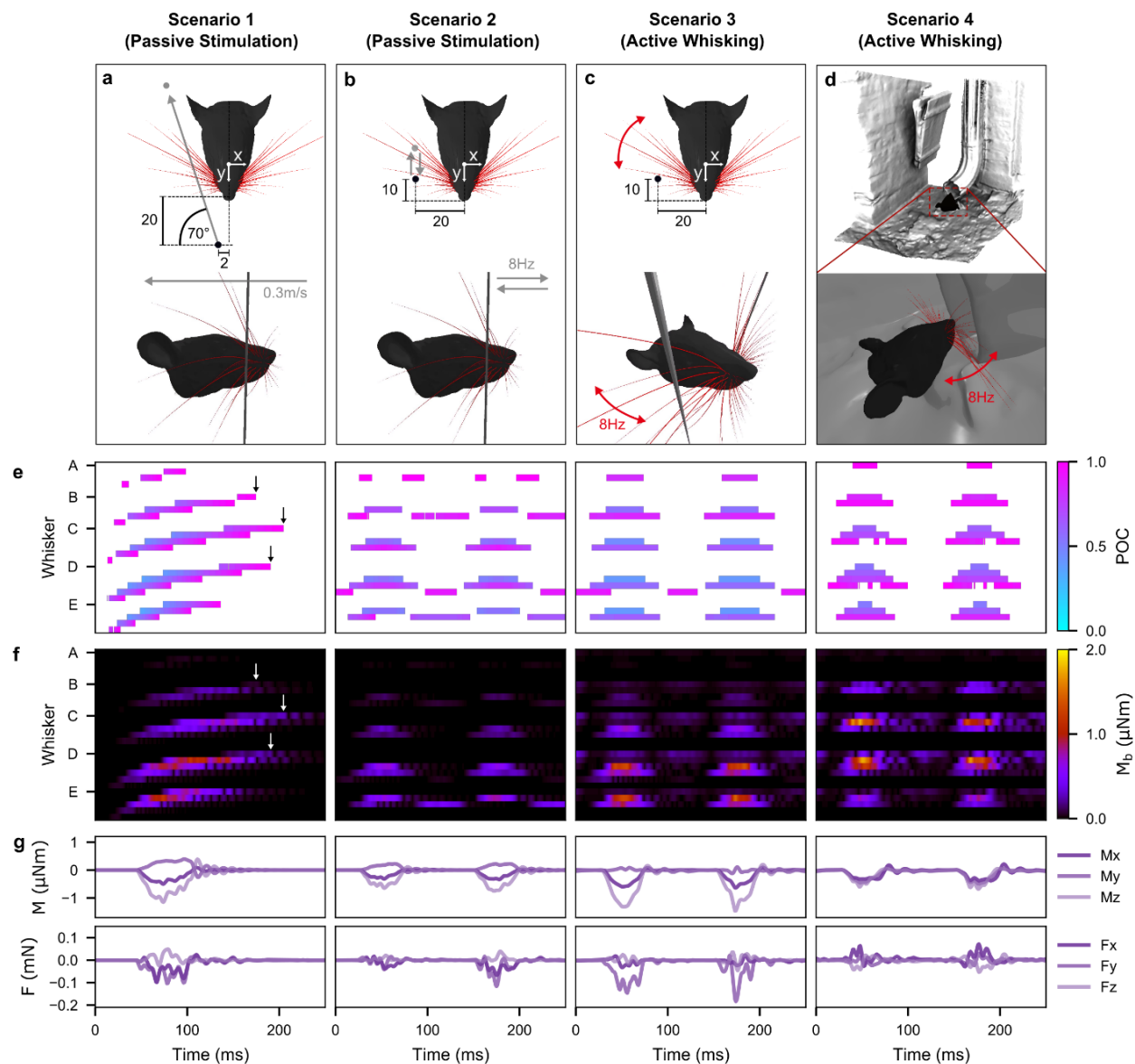
**Figure 3-3. Mechanical response of the full rat whisker array for four scenarios.** For simplicity only results for the right side of the array are shown. Units are in millimeters unless indicated otherwise. **(a)** Visualization of the passive stimulation experiment simulating a vertical peg moving from rostral to caudal through the middle of the immobile right array. **(b)** Visualization of the passive stimulation experiment simulating a vertical peg moving back and forth, in and out of the immobile right array at a pulse frequency of 8Hz. **(c)** Visualization of active whisking against two vertical pegs. The array performed a typical whisking motion as described in (Knutsen, Biess et al. 2008) with a whisking frequency of 8 Hz. **(d)** Visualization of a natural environment experiment. Whisking motions are the same as in (c), but the array palpates the shape of a drainage pipe. **(e)** Points of contact (POCs) for each whisker of the right array over time for each scenario. The POC is normalized to the length of the whisker and indicated by the colormap. The whisker

identities are grouped by row (dorsal to ventral) and sorted by column (caudal to rostral). Each letter on the y axis indicates the first whisker of each group, the most caudal whisker of the corresponding row. **(f)** Magnitude of bending moment ($M_b$) of each whisker indicated by color. The whiskers are sorted as in (e). **(g)** Example of all six signal components at the base of the E2 whisker for each scenario. All panels share the same time scale (x axis).

front of the opening of a 3D scan of a drainpipe, to simulate a rat that actively palpates a typical

object found in its natural habitat. Movies S1-S4 show the simulations of Scenarios 1, 2, 3, and 4,

respectively. Note that for simplicity only the right side of the array is considered.

Figure 3-3e shows the point of collision (POC) of each whisker in the array as a function of time

for each of the four scenarios. The POC is normalized between 0 (whisker base) and 1 (whisker

tip). For passive stimulation during a single sweep through the array (first panel), the spatial

arrangement and geometry of the whiskers result in a systematic pattern of whisker activation. The

moving peg first collides with the most rostral whiskers of the C, D, and E rows. Contact durations

are short because the whiskers are small. As expected, contact durations increase as the peg

collides with the more caudal and larger whiskers. Note that the slip-off of each whisker tip is

clearly visible, as reflected in high POC values at the very end of each whisker contact.

The systematic activation pattern is lost when a subset of whiskers is stimulated periodically, as in

the example of Scenario 2 (Figure 3-3e, second panel). Since the peg moves only about halfway

into the array, it does not collide with the more caudal (Greek and first column) whiskers. Very

short (rostral) whiskers are also missed, which results in activated clusters consisting of the middle

columns 1-3. As deliberately designed in Scenario 2, these contact responses closely resemble

those observed during the active whisking of Scenario 3 (Figure 3-3e, third panel). However, the

passive stimulation (Scenario 2) generates more slip-offs and therefore causes more contact

patterns that are out-of-phase (B3, D4, E3) or doubled (A2), i.e., the whiskers are hit by the peg

during both rostral-caudal and caudal-rostral motion. A comparison of Scenario 2 and Scenarios 3 and 4 suggests that active whisking prevents more whiskers from slipping off the peg, likely because roll and elevation continuously change the orientation of the whiskers relative to the peg throughout the duration of the whisk.

Figure 3-3f shows the magnitudes of the bending moment, $M_b$ ( $= \sqrt{M_y^2 + M_z^2}$ ), at the base of each whisker during the first 250 ms of each behavioral condition. In the first panel, oscillations in the bending moment near the end of several traces reflect the whiskers' vibrations after they have slipped off the peg (black and white arrows). This effect is particularly visible for whiskers β, γ, and δ. Although less distinct, similar vibrations also cause $M_b$ to increase between whisks during both active whisking scenarios (Figure 3-3f, third and fourth panels). Also note that $M_b$ and POC tend to be inversely related, given that a contact closer to the base of the whisker generally results in a greater mechanical response. Finally, because the head was stationary across all simulations, the more caudal whiskers tend to make contact closer to their bases (lower POC) and undergo larger deflections, leading to increased values of $M_b$ in this region of the array.

An example of the individual signal components at the base of a single whisker (in this case E2) is shown in Figure 3-3g. For this whisker, the mechanical signals during active whisking appear qualitatively similar between the peg and drainpipe conditions, with only a slight difference in amplitude. Similar results were found for the majority of the other whiskers in the array. However, these two conditions are clearly distinguishable at the level of the entire array (Figure 3-3e).

### 3.3.4 Passive stimulation and active whisking result in different spatiotemporal patterns of mechanical signals

Quantitative analysis of the four scenarios in Figure 3-3 clearly shows the differences between passive stimulation and active whisking. For example, the contact patterns in Figure 3-3e can be

used to compute the contact probability P(C) of each whisker within each trial (Figure 3-4a), i.e., the fraction of time that each whisker is in contact with the object (peg or natural surface) normalized to the trial duration. The mechanical signals, as shown for the bending moment $M_b$ in Figure 3-3b, can then be used to quantify the relationships between whiskers by computing the Pearson correlation (Pearson r) of $M_b$ across whisker pairs (Figure 3-4b).

As expected for the passive stimulation in Scenario 1, the caudal and longest whiskers in the Greek and first column are more likely to be in contact, while rostral whiskers have a very low probability of contact (Figure 3-4a, panel 1). The corresponding correlation matrix in Figure 3-4b (panel 1) shows the strongest correlations between whiskers in the same column or in neighboring columns. Because the vertical peg moves from rostral to caudal, the whiskers within the given column are stimulated almost simultaneously, causing nearly synchronous oscillations after slip-off and thus high Pearson r values. Depending on the location of slip-off, these correlations can also occur across neighboring columns (e.g., A1 is correlated with B2 and C2). However, the morphology of the array ensures that synchronized oscillations are unlikely beyond neighboring columns, leading to strong negative correlations with more distant whiskers (colored cyan in correlation matrix). We suggest that these types of correlations during a single, passive sweep could potentially be used by the animal to estimate the speed and direction of a moving object.

By design, the repeated peg stimulation of Scenario 2 generates contact probabilities P(C) that closely resemble those observed during active whisking against a peg (compare panels 2 and 3 of Figure 3-4a). However, correlations of the mechanical signals between whiskers are vastly different (Figure 3-4b, panels 2 and 3). Most notably, active whisking increases the correlations for certain subsets of whiskers. For whisker columns 2 and 3, this increase is primarily caused by
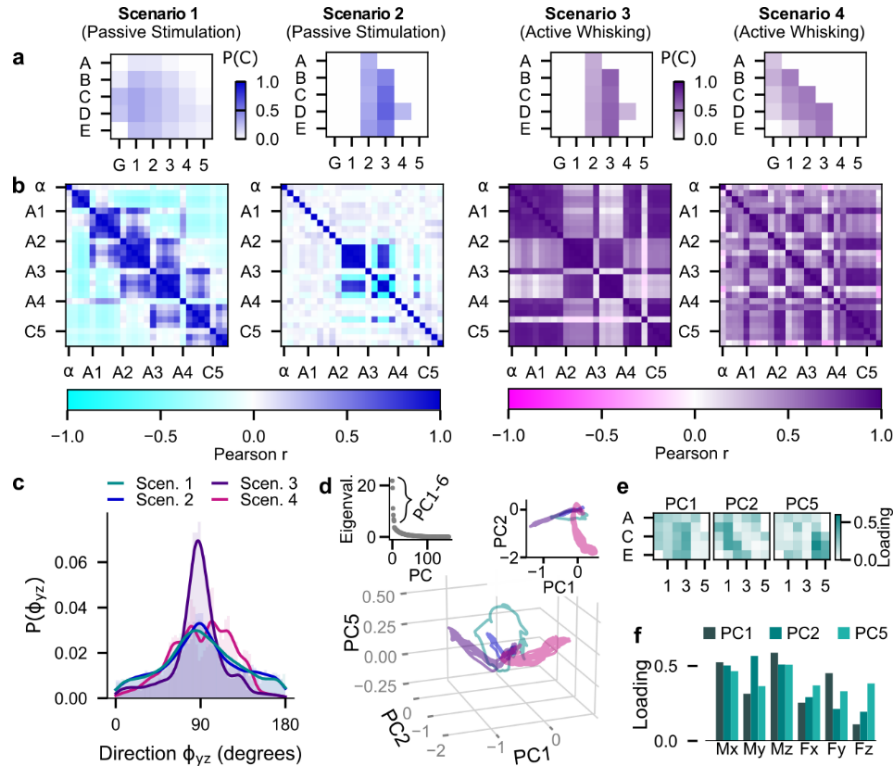
**Figure 3-4. Comparison of the mechanosensory signals acquired during the four example scenarios of Figure 3-3.** Different color schemes are used to illustrate results for the passive and active cases. **(a)** Contact probability P(C) for each whisker is computed as the duration of the interval when the whisker was in contact with the object normalized by the duration of the trial. **(b)** Correlation matrices (Pearson r) of the bending moment ($M_b$) between whisker pairs across the array. The whiskers are arranged in groups of the same column and ordered by row number from dorsal to ventral. The labels indicate the first whisker of each group (most dorsal whisker in each column). **(c)** Histograms (probability distributions) of the direction of the bending moment $\phi_{xy}$ in degrees. The distributions of $\phi_{xy}$ during the two types of passive stimulation with a vertical peg are very similar (2-sample Kolmogorov-Smirnov test; p=0.08). The distribution for active whisking against a vertical peg is peaked sharply at 90°, while the distribution for active whisking against more naturalistic surface is broad and contains many peaks, reflecting the variety of contact angles. The distributions of $\phi_{xy}$ for active whisking are significantly different from those observed during passive stimulation and from each other (2-sample Kolmogorov-Smirnov test; p<0.001). **(d)** Projection of the 162-dimensional signal space (6 mechanical components per whisker * 27 whiskers) onto the principal components PC1, PC2, and PC5, for each of the scenarios. Color code as in (c). *Inset left*: eigenvalues of the principal components (PCs). *Inset right*: projection of the mechanosensory signals into the PC1-PC2 plane. **(e)** Total loadings of PC1, PC2, and PC5 onto individual whiskers, obtained by summing over all 6 mechanical components. **(f)** Total loadings of PC1, PC2, and PC5 onto each of the mechanical components, obtained by summing over all whiskers.

near-simultaneous activation of the whiskers when colliding with the peg. For columns G, 1, 4, and 5, the increased correlations are mainly due to inertial effects caused by the whisking motion.

Similar effects appear in Scenario 4 (Figure 3-4b, panel 4), but for different whisker groups. Notably, even though the whisking motion in Scenarios 3 and 4 only differ in amplitude (see *Methods*), the different shapes of the environment generate very different contact patterns over time and correlation matrices across whiskers (panels 3 and 4 in Figure 3-4a-b). While whisking against the peg stimulates entire columns, whisking against the concave opening of the drainpipe activates the caudal-ventral half of the array.

Differences between active and passive whisking are not limited to signal magnitudes. As observed previously in the analysis of Figure 3-3, natural whisking motion includes protraction-dependent elevation and roll of each whisker, which change the whisker's orientation with respect to the environment during each whisk cycle. These orientation changes are clearly reflected in the direction of $M_b$, as measured by $\phi_{xy} = \left|\tan^{-1}\left(\frac{M_z}{M_y}\right)\right|$ in degrees; the four-quadrant inverse tangent was used such that $\phi_{xy} \in [0,180]$. The distributions of $\phi_{xy}$ for each scenario are shown in Figure 3-4c. Comparing Scenarios 2 and 3 (passive vs. active) reveals that active whisking against the peg shifts $\phi_{xy}$ towards 90°. An angle close to 90° indicates that the $M_y$ component is small and thus $M_b$ points in the direction of $M_z$, which is defined as bending within the plane of the whisker's curvature. These results suggest that active whisking against environmental features with substantial vertical components may help orient the whiskers so that they tend to bend in their plane of curvature, thereby generating a more uniform directional response at the base. In contrast, objects that contain features with multiple orientations (e.g., the drainpipe) result in different distributions of $\phi_{xy}$. Note that the distribution of $\phi_{xy}$ for Scenario 4 has a unique multimodal

shape that is significantly different from the other three scenarios (2-sample Kolmogorov-Smirnov test; p<0.001).

Finally, we performed an analysis that allowed us to capture the mechanical response of the entire array simultaneously. Together, the six mechanical components for each of the 27 whiskers define a 162-dimensional space that can be reduced using principal component analysis (PCA). PCA was performed by combining the data collected over time for each of the 162 variables in each scenario. Note that PCA does not consider the order in which the data was collected. Projection of the mechanosensory signals onto the first six PCs suggests that PC1, PC2, and PC5 capture the differences between the four scenarios most clearly (Figure 3-5). In the corresponding PC space, the trajectories (i.e., path through the PC space determined by the temporal evolution of the projected signals) corresponding to each of the four scenarios are clearly separated and occupy distinct regions of the space (Figure 3-4d).

To understand the meaning of the trajectories in the PC space, it is useful to look at the loadings (i.e., squared coefficients) of each PC. Figure 3-4e depicts the total loadings for each whisker (summed over all six mechanical components) for each of the three PCs. Each PC appears to represent a subset of whiskers. For example, PC1 (Figure 3-4e, left panel) receives the largest contribution from whiskers in column 2 and 3. These whiskers are highly active in Scenarios 2 and 3, thus explaining the corresponding large and overlapping excursions in the direction of PC1 (Figure 3-4d, right inset). The loadings of the signal components indicate that $M_z$ is likely responsible for the larger extent in the negative PC1 direction of the trajectory in Scenario 3 compared to 2 (Figure 3-4f). This PC analysis over all whiskers and all scenarios corroborates the result that active whisking tends to shift the direction of $M_b$ towards the direction of $M_z$, as shown in Figure 3-4c.
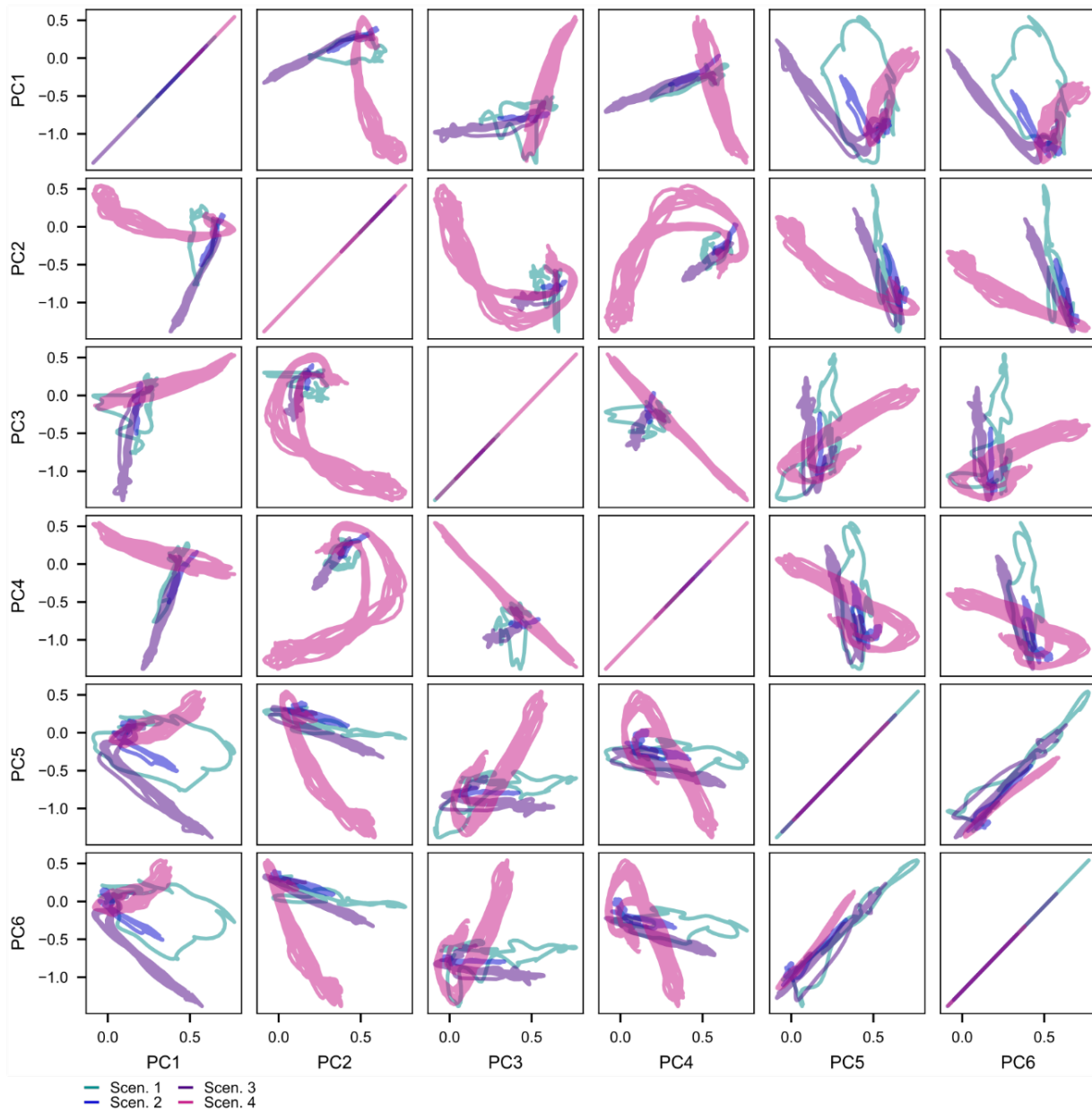
**Figure 3-5. Mechanosensory signals in the principal component (PC) space.** The mechanosensory signals were projected onto pairs of the six leading PCs for each of the four scenarios. The four trajectories separate the best when projected onto PC1 and PC5, while the trajectories for Scenarios 3 and 4 are best separated in the PC1 and PC2 plane.

In contrast, PC2 (Figure 3-4e, middle panel) is most strongly determined by the whiskers in a

diagonal across the first three columns (β, B1, C1, D1, D2, E2). These whiskers are most strongly
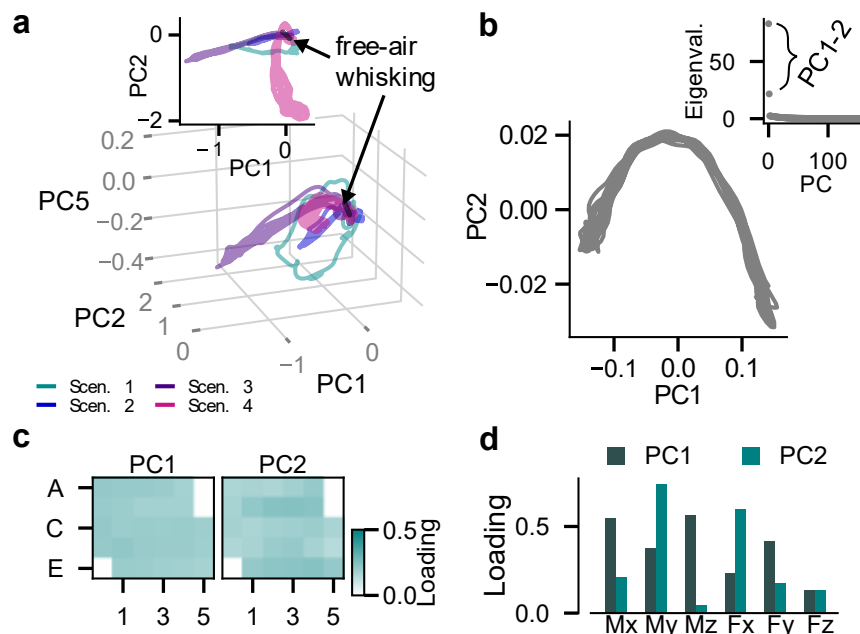


**Figure 3-6. Principal Component Analysis for the mechanical signals generated during non-contact whisking. (a)** Projection of the 162-dimensional signal space (6 mechanical components * 27 whiskers) onto the principal components PC1, PC2, and PC5 for each of the scenarios shown in Figure 3-4d in the main text. Color code matches that of Figure 3-4d. *Inset*: projection of the mechanosensory signals into the PC1-PC2 plane. The projections for non-contact whisking are shown in black as indicated by the arrows. The mechanical signals generated during non-contact whisking stem from the inertial effects of the whiskers and thus are very small in magnitude. **(b)** The mechanical signals projected onto the first two leading PCs as estimated by the data simulated during non-contact whisking, without collision (Scen. 1-4). The periodic nature of the signals stems from the repetitive whisking motion, which changes the orientation of the whiskers and thus the inertial effects throughout the whisking cycle. *Inset*: eigenvalues of the principal components (PCs). **(c)** Total loadings of each whisker for the two leading PCs corresponding to (b), obtained by summing over all 6 mechanical components. In contrast to the four collision scenarios in Figure 3-4e, all whiskers contribute almost equally to the PCs. **(d)** Total loadings for each of the mechanical components for the two leading PCs corresponding to (b), obtained by summing over all whiskers. The loads of the first PC indicate highest contribution from the components $M_x$, $M_z$, and $F_y$. This result makes sense because the largest change occurs in the horizontal plane, which affects $M_z$ and $F_y$ the most. In contrast, $M_x$ responds to torsion and the combination of elevation and protraction of the whisker.

activated in Scenario 4, explaining the large excursion of the corresponding trajectory in the PC2 direction. The increase in variance of the signals in the PC2 direction in Scenario 4 compared to Scenario 1 is likely due to the signal components $M_x$, $M_y$, and $M_z$ (Figure 3-4f). A difference in the magnitude of $M_y$ and $M_z$ manifests itself in a magnitude difference in $M_b$, visible in Figure 3-3f (first and last panel).

Finally, for PC5 (Figure 3-4e, right panel), the loadings are largest for the rostral whiskers in column 4 and 5. In Scenario 2 and 3, these whiskers do not collide with the peg. However, the active whisking motion in Scenario 3 produces inertial signals at the base of these whiskers, which likely explains the offset in the PC5 direction that separates these two scenarios. Inertial effects are the strongest for the signal components $M_x$ and $M_z$, which are the main contributors to PC5 (Figure 3-4f and Figure 3-6d). More details about the inertial signals during free-air whisking (no contact) are shown in Figure 3-6.

### 3.4 Discussion

We have developed a dynamic model of the whisker array of a "prototypical" rat, whose parameters and dynamics fall within the range of biological rats. This model is not intended to replicate the sensory input of a single, individual rat at high precision. Instead, the model has been validated to generate reasonable approximations of real whisker dynamics, well within the naturally occurring variability across animals. Individual rats vary in size, age, sex, and strain, which ultimately manifest in different sizes, scales, shapes, material properties, and spatial arrangement of the vibrissae. Despite this variability, rat brains have found solutions that allow these animals to use their vibrissal systems to accomplish similar tasks in a similar manner.

Understanding the underlying principles of the rat somatosensory pathway therefore cannot rely on modeling the sensors of an individual rat in detail (Marder 2011).

The utility of the present model is that it begins to allow us to study the input to neural circuitry that has evolved to deal with signals generated by multiple sensors interacting with a three-dimensional complex world. Behavioral studies have shown that natural rodent whisking behavior involves contact and collisions of many whiskers with the environment (Hobbs, Towal et al. 2016). Studies of vibrissal-responsive primary somatosensory ("barrel") cortex indicate that neural information is spatially integrated across multiple whiskers and that the statistics of the stimuli have a significant effect on the receptive fields due to adaptation mechanisms (Ramirez, Pnevmatikakis et al. 2014). These findings indicate that it is crucial to study neural activity in the vibrissal system in the context of natural behavior and the full whisker array. Although existing single-whisker models may be able to predict the dynamics of individual whiskers more accurately (Boubenec, Shulz et al. 2012, Quist, Seghete et al. 2014, Vaxenburg, Wyche et al. 2018), the present work offers 3D simulations of the entire array in a wide range of simulated environments and experimental conditions.

Three technical caveats should be noted when using the present model. First, it cannot be used to simulate high frequency vibrations because the spatial resolution of the whisker is limited to 20 data points (i.e., 20 links). Therefore, some dynamic behavior such as higher order resonance modes cannot be simulated. These modes are presumed to play a role in texture discrimination (Arabzadeh, Petersen et al. 2003, Neimark, Andermann et al. 2003, Wolfe, Hill et al. 2008), which lies beyond the scope of the present model. Second, because each node is limited to two degrees of freedom, shear forces cannot be modeled. Beam theory indicates that shear forces are negligible in straight vibrating beams with aspect ratios greater than 100 (Seon M. Han 1999). Whiskers

have aspect ratios of 1000 or greater, but it remains unclear how taper and curvature of the whisker may affect the shear forces at the base, and the extent to which these forces are transduced by the mechanoreceptors embedded in the follicle. These two technical limitations could be addressed in the *WHISKiT Physics* simulator by adding more nodes and an extra degree of freedom to each node, at the expense of increased computational load. Finally, the rostral-most macrovibrissae were not simulated. Previous work has indicated that these whiskers may be important when exploring object features that are small on the scale of the rat's sensory volume (Brecht, Preilowski et al. 1997), but that these whiskers are the least likely to make contact with a surface that is large on the scale of the rat's vibrissal array. When modeling how a rodent explores small objects, users of *WHISKiT Physics* should keep in mind that the simulated contact patterns will omit any potential contact with the most rostral whiskers.

In addition, all model validations are based on kinematic measurements (resonance and damping behavior, whisker shape, etc.) from experiments with real whiskers, or on dynamics predicted from previously published models that have also been validated against kinematic data (Boubenec, Shulz et al. 2012, Quist, Seghete et al. 2014). It is not clear how one could ever obtain ground truth dynamic measurements of forces and moments in the real animal, as any sensor would interfere with the whisker's dynamics. The relationship between kinematics and dynamics is primarily determined by the material properties (density, Young's modulus, damping) of the whisker, and thus dependent on the model assumptions for these parameter values. Previous work has found that density as well as Young's modulus vary between proximal and distal whisker regions (Quist, Faruqi et al. 2011, Belli, Yang et al. 2017, Yang, Belli et al. 2019). In *WHISKiT Physics*, parameters were chosen to be within the range of biological variation: density was

approximated to increase linearly from base to tip, while Young's modulus and damping properties were assumed to be homogeneous within and across whiskers.

Finally, experimental measurements of follicle compliance and translation on the mystacial pad are extremely limited at present (Knutsen 2016). Our simulations showed that rigid boundary conditions in the single whisker model are insufficient to match experimental data obtained when whiskers are deflected *in situ*, on the rat's face (Section 3.6.2 ; Figure 3-9). To model a compliant follicle, torsional springs were incorporated at the whisker base and the spring constants were optimized to match the mechanics observed experimentally in the anesthetized animal (Section 3.6.2 ; Figure 3-9). However, the stiffness of the tissue surrounding the follicle in the awake animal likely depends on the degree of muscle contraction during each whisk cycle (Ashwell 1982). These muscle contractions can also cause translational shifts of the entire mystacial pad in caudal-rostral as well as ventral-dorsal directions (Knutsen 2016). *WHISKiT Physics* does not model these changes in follicle compliance and position during whisking, but could potentially be extended to incorporate them if corresponding experimental data from the awake animal were available. Given that experimental data suggest that translational shifts of the mystacial pad are approximately uniform across whiskers and roughly maintain spatial relationships between whiskers (Knutsen 2016), we expect that changes in follicle stiffness or position would affect deformation magnitude and resonance frequency  relatively uniformly across the array. Thus, incorporating muscle contraction in the model is unlikely to change the results presented here.

The present work (Figure 3-4) shows that *WHISKiT Physics* can be used to examine the spatiotemporal patterns of mechanical signals across the rat whisker array in ways that cannot currently be achieved in the real animal.  For example, active whisking generates notably pulsatile patterns of contact, associated with the whisking periodicity. We have previously proposed that

these discrete patterns of contact suggest that rodents may employ a strategy of "windowed sampling" to extract an object's spatial features (Quist, Seghete et al. 2014, Hobbs, Towal et al. 2016). More specifically, we have proposed that the rat ensures that the whiskers remain in contact with an object for a sufficiently long duration (20 – 50 ms) so that the vibrations generated by collision with the object damp out (Quist, Seghete et al. 2014). The animal could then spatially integrate quasi-static mechanical signals across whiskers to determine the object's spatial features. Such a strategy closely resembles the periodic sampling strategy associated with sniffing behavior (Kepecs, Uchida et al. 2006), an important means by which animals can identify elements and gradients within an olfactory plume.

Importantly, Figure 3-4b demonstrates that even when a passive touch experiment is deliberately designed to match the periodic patterns of whisker-object contact observed in the awake animal, correlations between mechanical signals across whiskers are quite different. The results further suggest that active whisking helps to minimize slip-off, and to ensure that the whisker deflects within its plane of curvature. Moreover, the principal components reveal how whisker identity and the mechanics at the base uniquely shape the signal trajectories, which is only possible with a model that captures the full input space of the sensor array.

We anticipate that *WHISKiT Physics* will soon allow us to examine how these patterns can be used to distinguish between stationary and moving objects, how the patterns would differ if the whisker array were altered, and what are the advantages of active compared to passive sensing. We also expect it to enable the field to leverage techniques such as information theory, virtual reality, and reinforcement and machine learning. These approaches will allow researchers to model both sensory information processing as well as control circuits, learning, and environmental interactions. For example, a similar but unvalidated model has already been used to make

predictions about the processing architectures in the trigeminal pathway based on a goal-driven deep neural network approach (Zhuang, Kubilius et al. 2017). Finally, we expect that the simulation system can be used to bootstrap hardware implementation of artificial whisker systems, which could potentially accelerate and facilitate the design process of robots (Clements and Rahn 2006, Kim and Möller 2007, Evans, Fox et al. 2009, Solomon and Hartmann 2010, Evans 2013).

## 3.5 Methods

All experiments involving animals were approved in advance by the Animal Care and Use Committee of Northwestern University.

### 3.5.1 Extrapolation of optimized material parameters across whiskers with varying geometries

After optimizing and validating dynamics for the single whisker model (*Supplementary Information*), we validated the resonance behavior of all whiskers across the array. To perform this validation, we searched the literature for studies that had published values of whisker resonance along with whisker length, base diameter, and tip diameter. We could find no study that had published values for all of these variables for a given set of whiskers. However, Hartmann et al. (Hartmann, Johnson et al. 2003) published resonance frequencies, arc length, and base diameter for 24 whiskers, and we were able to obtain tip diameter measurements for the same 24 whiskers from the original 2003 experiment (Dataset S1).

Based on these data, we simulated 24 straight whiskers with the measured arc lengths and base and tip diameters. The material parameters were set to the optimized values $\theta_E = 5.0$ and $\theta_\zeta = 0.33$. In simulation, the base of each whisker was rigidly clamped to a motor (defined as the origin) such that the whisker lay in the horizontal (x-y) plane and was aligned with the x-axis. The motor rotated the whisker about the vertical (z) axis. Each simulation lasted 1 second, sampled at 1kHz.

The angle from the original position $v(t)$ was changed according to a Gaussian-like function with $v_0 = \frac{\pi}{3}$, $\mu = 4\sigma$ and $\sigma = 0.025$, to ensure smooth motor movement at the beginning of the actuation according to eq. 1:

$$v(t) = v_0 e^{-\frac{1}{2}\left(\frac{t-\mu}{\sigma}\right)^2} \qquad \text{(eq. 1)}$$

The rotation of the motor was terminated abruptly after 0.128 seconds to induce vibrations of the whisker. The simulation was performed once for each whisker geometry.

The x, y, and z position of all 20 links was recorded at each time step, but only the y-component of the whisker tip (link 20) was used for further analysis. The data was cropped to contain only free whisker oscillations, whereas FFT was performed to find the first resonant mode.

### 3.5.2 Extrapolation of optimized material parameters to the average rat vibrissal array

The arc length (S), base radius ($r_{base}$), and the radius slope of the whisker can be approximated as functions of whisker position (row, column) from which the tip radius can be calculated (Belli, Yang et al. 2017). The intrinsic curvature of the whisker is approximated by a quadratic function $y = Ax^2$ in the x-y plane according to Belli et al. 2018 (Belli, Bresee et al. 2018), where $A$ represents the curvature coefficient. The value for $A$ can be calculated by using the relationship between intrinsic curvature and arc length of the whisker. In our model, $N$ equidistant points along this quadratic curve represent the position of the nodes.

We tested whether the simulations using optimized parameters would generalize to explain the dynamics of all whiskers within the average whisker array as described by the equations found in Belli et al. (Belli, Yang et al. 2017). The simulations were identical to those described in section

3.5.1 , but all 27 whiskers comprising the right side of the array (rows A-E, columns Greek-5) were simulated.

The experimental data for comparison (resonance frequency and arc length) was compiled from Hartmann et al. (Hartmann, Johnson et al. 2003), Wolfe et al. (Wolfe, Hill et al. 2008), and Neimark et al. (Neimark, Andermann et al. 2003), see (Dataset S1).

### 3.5.3 Collision with a straight edge

To validate simulation dynamics during collision, we compared results with a previously published analytical model (Boubenec, Shulz et al. 2012) that simulated a straight whisker colliding with the edge of an object. For this purpose, each simulated whisker was rotated at its base at constant angular velocity about the vertical axis through the base point until the 19th link (95% of whisker length from the base) collided with a rectangular edge. Initial angular displacement from the edge was set to 5.6° $\left(\frac{\pi}{32} \, rad\right)$. When contact with the object was detected, the driving force at the base was set to zero, allowing natural deceleration of the whisker. Collision was set to be inelastic to avoid rebound.

The collision angle between whisker and edge was defined to be 60° in the horizontal, and 45° in the vertical plane to generate mechanical responses in all three dimensions. We performed simulations with 12 whiskers from 4 different rows (α, A2, A2, β, B1, B2, γ, C1, C2, δ, D1, D2). In the first set of simulations, intrinsic curvature was omitted, i.e., 12 straight whiskers replicated the experiment described in Boubenec et al. (Boubenec, Shulz et al. 2012). In the second set of simulations, all whiskers were curved according to the model in Belli et al. (Belli, Bresee et al. 2018). For each whisker, we simulated collisions for 6 velocities (90, 180, 270, 360, 450, 540 deg/s) while recording all six components of the mechanical signals at the base

$(Fx, Fy, Fz, Mx, My, Mz)$ as well as a binary "contact vector" $C$, which indicated contact state (0 or 1) for each whisker link. Simulation output was sampled at 1 kHz and simulations were terminated after 0.2 seconds.

For signal analysis, the mechanical components $F_x, F_y, F_z, M_x, M_y, M_z$ were smoothed by convolving a $10^{th}$ order Hanning window. Time of collision was obtained by finding the first nonzero value of $C$ of any whisker link.

To determine the magnitude of the shock immediately after collision for each whisker, the derivative of the signal $M_z$ was rectified and the maximum $\dot{M}_{z,max}$ at time $t_{max}$ within the first 10 ms after collision was found. The shock magnitude $\dot{M}_{z,max}$ was normalized for each whisker by dividing by the average across all six speeds. Bending moment and transverse force at time $t_{max}$ were computed using eq. 2-3.

$$M_b = \sqrt{M_y^2 + M_z^2} \qquad \text{(eq. 2)}$$

$$F_t = \sqrt{F_y^2 + F_z^2} \qquad \text{(eq. 3)}$$

Propagation of the deformation wave from tip to base was determined for the two longest whiskers in each of the four rows (α, β, γ, δ, A1, B1, C1, D1). Whiskers A2, B2, C2, D2 were too small and stiff to exhibit a measurable deformation wave. To track the propagation of the deformation wave, the location of maximum deflection point of each whisker relative to whisker length was measured relative to the position of first contact for 5 subsequent time samples.

### 3.5.4 Simulation of complete vibrissotactile input across the array

The mechanical signals at the base of each whisker of the full rat whisker array were simulated for three scenarios: motion of a vertical peg through the immobile array, active whisking against two fixed pegs, and active whisking against the 3D shape of a drainpipe representing the natural environment. In all three scenarios, the whiskers were arranged according to the morphology of the rat whisker array described in Belli et al. (Belli, Bresee et al. 2018). For visualization purposes, a scanned rat head was used to model the head to which the array is attached. In all simulations, collisions between the head and other objects were suppressed to increase the simulation speed.

*Scenario 1 (passive stimulation)*: the origin of the whisker array (base point average) was placed at the origin of the world frame and oriented such that the average row plane was approximately parallel to the horizontal plane. The whiskers remained at resting position while a vertical peg moved with constant speed (0.3 m/s) from rostral to caudal through the middle of the array. The peg had a diameter of 1 mm and a length of 80 mm. An illustration of the simulation experiment is given in Figure 3-3a and Movie 1.

*Scenario 2 (passive stimulation)*: same as Scenario 1, but the peg was repeatedly moved back and forth between the starting position and the middle of the array. The peg was moved with a velocity following a sinusoidal function with a maximum velocity of 0.3 m/s. An illustration of the simulation experiment is given in Figure 3-3b and Movie 2.

*Scenario 3 (active whisking against peg)*: the origin of the whisker array (base point average) was placed at the origin of the world frame and oriented such that the average row plane was approximately parallel to the horizontal plane. Two vertical pegs were placed bilaterally with an offset of ±30 mm in the x axis and -10mm in the y axis to cause collisions with the protracted

whiskers. Position and orientation of the array and the pegs remain fixed while the whiskers perform a typical whisking motion with a retraction angle of 15 degrees and protraction angle of 30 degrees, as described below. An illustration of the simulation experiment is given in Figure 3-3c and Movie 3.

*Scenario 4 (active whisking in natural environment):* the position and orientation of the rat model was manually selected to ensure sufficient but not extreme contact between the surface of the 3D scan and the whisker array. The positions of the rat head and the 3D surface were held fixed while the whiskers performed a typical whisking motion. To model the natural environment of a rat, we collected 3D representations of a typical rat habitat (drainpipe) in the Evanston, IL area with a KINECT™ for Xbox V2 (Microsoft) and a Predator Helios 300 Laptop (Acer). The scans collected covered a volume of approximately 2 cubic meters. In Geomagic® Design X™ (3D Systems, Inc.), the point cloud data was manually edited to remove holes and erroneous points before triangulation to generate a mesh with maximum edge length of 3mm. An illustration of the simulation experiment is given in Figure 3-3d and Movie 4.

For both active whisking scenarios (Scenarios 3 and 4), the whiskers performed sinusoidal whisking motion at a frequency of 8 Hz with a maximum protraction angle of 30 and 40 degrees, respectively, and a maximum retraction angle of 15 degrees from rest. Previous work (Knutsen, Biess and Ahissar, 2008) found that natural whisking behavior involves elevation $\varphi\ (t)$ and torsion $\zeta\ (t)$ of the whisker, both of which show a row-wise dependency on the angle of protraction $\theta\ (t)$. Based on these findings (Knutsen, Biess and Ahissar, 2008), we constructed equations of motion (eq. 4-5) for each row (A-E) that are used to drive angular rotation at the base point during active whisking.

$$\varphi(t) = \theta(t)\Delta\varphi_j \quad \Delta\varphi_j = \{0.398, 0.591, 0.578, 0.393, 0.217\}, j = A, B, \dots E \qquad \text{(eq. 4)}$$

$$\zeta(t) = \theta(t)\Delta\zeta_j \quad \Delta\zeta_j = \{-0.9, -0.284, 0.243, 0.449, 0.744\}, j = A, B, \dots E \qquad \text{(eq. 5)}$$

Each simulation lasted 250 ms involving 2 whisk cycles, and was sampled at 1kHz. All six components of the mechanical signals at the base of each whisker $(F_x, F_y, F_z, M_x, M_y, M_z)$ and a binary vector $C$ indicating contact (1) or no contact (0) for each whisker link were recorded. For signal analysis, the mechanical components $F_x, F_y, F_z, M_x, M_y, M_z$ were smoothed by convolving a 10th order Hanning window. The magnitude of the bending moment was computed according to equation eq. 2.

Point of contact $(POC)$ was determined by the number of the links in contact relative to the total number of links (base: $POC = 0.0$, tip: $POC = 1.0$).

### 3.6 Supplemental Materials

### 3.6.1 Model of a single whisker

The model of a single whisker was created using the Bullet Physics Library (Coumans 2015) and extends a previous two-dimensional (2D) model (Quist, Seghete et al. 2014) to three dimensions (3D). The whisker is modeled as a chain of N conical frustums (links) connected by N-1 equidistant joints (nodes). The length of the links $l_{link} = S/N$ depends on the whisker arclength S and the number of links N, while the radius at each node $r_n$ decreases linearly from the whisker base to the tip (eq. S1). Schematics of two views of the model are shown in Figure 3-7.

$$r_n = r_{base} - \left(\frac{n-1}{N}\right)(r_{base} - r_{tip}), \text{where } n = 1, \dots, N + 1 \qquad \text{(eq. S1)}$$

Each link has mass $m_n = \rho_n \frac{\pi\, l_{link}}{3} (r_n^2 + r_n r_{n+1} + r_{n+1}^2)$, where density $\rho_n = \rho_{base} - \left(\frac{n-1}{N}\right)(\rho_{base} - \rho_{tip})$ increases linearly from base to tip. Values for density at the base $(\rho_{base})$ and the tip $(\rho_{tip})$ were obtained from a previous study (Yang, Belli et al. 2019).
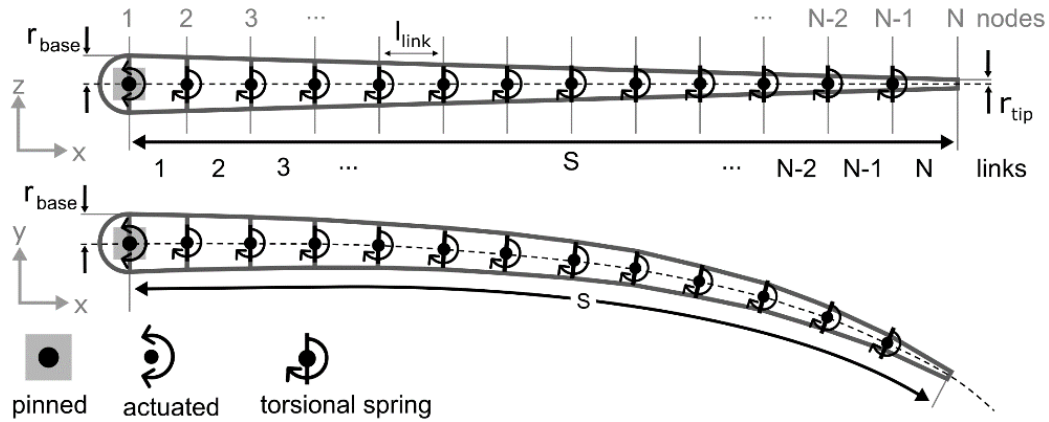


**Figure 3-7. Schematics illustrate the whisker model used in all simulations.** The whisker is rigidly driven from node 1, which represents the follicle. The node is pinned so that it can rotate but not translate. Nodes 2-N each represent a 3D torsional spring damper. The whisker is straight in the x-z plane and has intrinsic curvature in the x-y plane. In each simulation, the curvature was chosen to be appropriate for the specific whisker being simulated (see text for details). For the optimization of spring stiffness and damping parameters of nodes 2-N, the geometry of the whisker (arc length S, base radius r_base, and tip radius r_tip) were obtained from the real whiskers used in the experiments.

Nodes 2 through $N$ are modeled as torsional spring-dampers with two degrees of freedom, permitting rotations about the y and z axes. Parameters $k_n$ and $c_n$ represent stiffness of the spring and damping in the two bending directions (rotations about the y and z axes). Twist of the whisker (rotation about the x-axis) was omitted. The whisker follicle is represented by node 1. The follicle is pinned (cannot translate) and its rotation about all three axes is rigidly controlled. As described in section 3.6.2 , a torsional spring-damper was later added to model the tissue elasticity of the follicle in the skin, allowing rotations about the y and z axes.

Theoretically, each node can be viewed as the pivot point of a pendulum (Quist, Seghete et al. 2014). The adjacent distal portion of the whisker has mass $M_n$, which determines the mass of the pendulum, and the distance $L_{com,n}$ between its center of mass (com) and the $n^{th}$ node determines the length of the pendulum. Thus, the stiffness and damping of the spring associated with the node can be calculated as:

$$k_n = \frac{E_n I_n}{l_{link}} \qquad\qquad\qquad (\text{eq. S2})$$

$$c_n = 2\zeta_n L_{com,n}\sqrt{M_n k_n} \qquad\qquad\qquad (\text{eq. S3})$$

where $E_n$ is Youngs's modulus and $I_n$ is the area moment of inertia of the associated link. The variable $\zeta_n$ represents the damping ratio of the spring of the $n^{th}$ node.

From equations S2 and S3 and given that $I_n = \frac{\pi r_n^4}{4}$, it follows that the stiffness and damping at each node are primarily determined by the geometry of the whisker. Following previous studies (Hartmann, Johnson et al. 2003, Neimark, Andermann et al. 2003, Quist, Faruqi et al. 2011, Boubenec, Shulz et al. 2012, Carl, Hild et al. 2012, Yan, Kan et al. 2013, Quist, Seghete et al. 2014, Vaxenburg, Wyche et al. 2018), our model assumes uniform Young's modulus and uniform damping ratio, i.e., $E_0 = E_1 = \cdots = E_N$ and $\zeta_0 = \zeta_1 = \cdots = \zeta_N$. We denote the corresponding model parameters as $\theta_E$ and $\theta_\zeta$. We optimized the parameters $\theta_E$ and $\theta_\zeta$ using kinematic data obtained from a real whisker.

### 3.6.2 Experiments for model optimization

To optimize and validate the model we performed two separate experiments. The first experiment (Experiment 1) involved rotating whiskers on a motor in the horizontal plane, resulting in motion

that was approximately 2D although 3D motion was quantified. Data from this first experiment were used to optimize material parameters (Young's modulus and damping coefficient) for the model. The second experiment involved manual deflections of different whiskers in the anesthetized animal. The whiskers were deflected in several different directions, and these data were used to optimize the constants of the spring modeling the elasticity of the follicle.

**Table 3-1. Dimensions of the whiskers and motor parameters used in Experiment 1**

| Dimensions of the whiskers | | | |
|---|---|---|---|
| **Whisker** | **Arc length (mm)** | **Base diameter (μm)** | **Tip diameter (μm)** |
| α | 29.6 | 120 | 35 |
| B1 | 34.1 | 131 | 30 |

| Motor parameters | | |
|---|---|---|
| **Parameter** | **Variable** | **Values** |
| Driving signal | N/A | $\varphi(A, \omega) = Ae^{-\omega(t-t_0)^2}$ |
| Amplitude (deg) | A | 45 |
| Speed (deg/s) | ω | 900, 2000, 3500 |
| Frequency (Hz) | f | - |
| Time offset (s) | $t_0$ | 45/200 |

The first experiment used two whiskers, α and B1, whose geometric parameters are listed in Table 3-1. Both whiskers were trimmed so that their tips could be clearly seen in the video, therefore they both have a shorter arc length and larger tip diameter than typical. The base of each whisker was fixed to the vertical shaft of a DC motor and rotated in a "gaussian pulse" motion. The whisker was oriented so that its intrinsic curvature coincided approximately with the horizontal plane. The motor was controlled using a microcontroller (PIC32) running a feedback controller at 5 kHz. At the beginning of each trial, the initial motor position was set to 0° and the microcontroller was synchronized with two orthogonally mounted high-speed video cameras (Mikrotron 4CXP; E1:

1000fps; E2: 500 fps, later upsampled to 1000 fps) used to track the whisker's motion. The amplitude, speed and frequency of the driving signal was varied (Table 3-1), and each parameter combination was repeated five times. After data collection, the whisker was removed from the motor and the base diameter (at the fixation point on the motor) and length were measured using a microscope (Leica DM750).

The second set of experiments (Experiment 2) was performed in the anesthetized rat as part of a separate study (Bush, Solla et al. 2021). All whiskers except for one were trimmed down to the length of the fur. The spared whisker was manually deflected with a graphite probe in eight cardinal directions, at two or three different contact points along its length, at two different speeds. Five different whisker identities from 11 different animals were used.

In both Experiments 1 and 2, the 3D whisker reconstruction from the two orthogonal camera views was performed in three steps. First, the whiskers were tracked in 2D using the software "Whisk" (Clack, O'Connor et al. 2012). In each view, the 2D tracked whisker shapes were cleaned and smoothed. Second, the two cameras were calibrated with the Caltech Camera Calibration Toolbox, OpenCV, and custom Matlab and python code. Finally, an iterative optimization was used to find the best 3D whisker shape that minimized the 2D back-projection error, defined as the Euclidean distance between the back-projected whisker and the actual, imaged whisker, summed over all back-projected points.

To analyze the manual deflections in Experiment 2, we used semi-automated tracking code to determine the 3D contact point and the time at which the graphite probe made contact with the whisker. The 3D tracking data was filtered with a thresholded median (Hampel) filter using a window size of 3 frames and a threshold of 1.5 standard deviations for outliers.

Finally, the best trials were manually selected for each whisker in both experiments. The resulting

datasets are shown in Table 3-2.

**Table 3-2. Datasets for Experiment 1 and Experiment 2**

|  | Whisker identities | Number of trials |
|---|---|---|
| Experiment 1 | α | 10 |
|  | B1 | 6 |
| Experiment 2 | B1 | 83 |
|  | B2 | 63 |
|  | C3 | 13 |
|  | D0 | 28 |
|  | D2 | 74 |

### 3.6.3 Model optimization

Two optimizations were performed to match the simulated dynamics with the dynamics of real

whiskers. The first optimization determined optimal values of the parameters of the single whisker

model ($\theta_E$ and $\theta_\zeta$) using data collected *ex vivo* (Experiment 1), while the second optimization was

used to find the optimal values for the follicle parameters (stiffness and damping) using data

collected *in vivo* (Experiment 2).

### 3.6.3.1 *Optimization of single-whisker dynamics in two dimensions*

In order to optimize the parameters $\theta_E$ and $\theta_\zeta$, the motor setup described for Experiment 1 was

replicated in simulation using Bullet Physics Library (Erwin and McCutchan 2008, Coumans

2015).

Because whisker dynamics depended on the geometry of the whisker, the single whisker model

was modified to accurately match the dimensions and shape of the real whisker in the experiment

(Table 3-1). The 3D data points of the first frame were used to reconstruct the whisker in

simulation. These data points defined the locations of the nodes and the length of the links between

them, respectively. The smoothed driving signal of the motor was used to control the angular displacement of the whisker base about the axis of rotation.

The mechanical signals at the whisker base are primarily determined by its geometry and its material properties, stiffness and damping. In the single-whisker model, stiffness and damping of the whisker are set by stiffness and damping at each node, which are a function of Young's modulus ($E$) and damping ratio ($\zeta$), respectively (eq. S2 and S3). The true values of $E$ and $\zeta$ are unknown and therefore constitute the free parameters of our model, denoted as $\theta_E$ and $\theta_\zeta$. We assume that $\theta_E$ and $\theta_\zeta$ are constant and the same for all nodes and all whiskers, so they only approximate $E$ and $\zeta$, respectively. The parameters $\theta_E$ and $\theta_\zeta$ were optimized using experimental data from two large, caudal rat whiskers, obtained from array positions α and B1. Each whisker was attached to a motor and driven with a Gaussian pulse at three different speeds, which allowed us to quantify the dynamic behavior of the whisker based on the resonance frequency ($f_n$) and logarithmic decrement ($\delta$) of the induced oscillations.

The experiment was then replicated in simulation using the single-whisker model with the known arc length, curvature, and base diameter of the real whiskers. To avoid local minima, we used a brute-force approach to iterate through 1296 combinations of $\theta_E$ and $\theta_\zeta$ values within a specific range ($\theta_E$ was varied between 2.0 and 6.5 GPa, and $\theta_\zeta$ between 0.15 and 0.6). For each pair of parameter values, five trials were randomly sampled for each of the two whiskers. Then each trial was simulated and evaluated in terms of its first-mode resonant frequency (FRF), logarithmic decrement δ, and peak amplitude A, computed from the y trajectory of the whisker tip evolving over 1000 samples (= 1 second). The FRF was determined by finding the peak of the power spectrum computed via the Fast Fourier Transform (FFT). The value of δ was calculated in the

time domain: given the magnitudes of the first two adjacent peaks, $y_0$ and $y_1$, $\delta = \ln\left(\frac{y_0}{y_1}\right)$. The value of $y_0$ was used as measurement for peak amplitude A.

We used the median symmetric accuracy (MSA) (Morley, Brito et al. 2018) to quantify the total error of the simulations across the 10 trials. The MSA was computed using eq. S4a, where simulated and experimental measurements are denoted by the subscript $_{sim}$ and $_{exp}$, respectively. The median was calculated from the pooled FRF, $\delta$, and A measurements across all 10 trials.

$$MSA(\theta_E, \theta_\zeta) = exp\left\{median\left(\left|\ln\left(\frac{FRF_{sim}(\theta_E,\theta_\zeta)}{FRF_{exp}(\theta_E,\theta_\zeta)}\right)\right|, \left|\ln\left(\frac{\delta_{sim}(\theta_E,\theta_\zeta)}{\delta_{exp}(\theta_E,\theta_\zeta)}\right)\right|, \left|\ln\left(\frac{A_{sim}(\theta_E,\theta_\zeta)}{A_{exp}(\theta_E,\theta_\zeta)}\right)\right|\right)\right\} - 1 \quad \text{(eq. S4a)}$$

The optimal parameter values $\theta_E^*$ and $\theta_\zeta^*$ were obtained by finding the parameter combination yielding the minimum MSA across the range of parameter evaluation:

$$\theta_\zeta^*, \theta_E^* = \underset{\substack{\theta_E \in [2.0, 6.5], \\ \theta_\zeta \in [0.15, 0.6]}}{\operatorname{argmin}} MSA(\theta_E, \theta_\zeta) \qquad \text{(eq. S5)}.$$

As shown in Figure 3-8a, the minimum of the error surface was found to be located at $\theta_E = 5.0$ GPa and $\theta_\zeta = 0.33$. Values of the true Young's modulus have been reported to fall between 1.3-7.8 GPa (Hartmann, Johnson et al. 2003, Neimark, Andermann et al. 2003, Quist, Faruqi et al. 2011, Kan, Rajan et al. 2013, Adineh, Liu et al. 2015), while the true damping ratio has been estimated between 0.05 and 0.28 (Hartmann, Johnson et al. 2003, Neimark, Andermann et al. 2003, Vaxenburg, Wyche et al. 2018).

Given these optimized parameters, the actual dynamic properties measured from simulated trajectories were in good agreement with values observed experimentally (Table 3-3). Moreover,

the resonance frequencies of 65 Hz and 59 Hz and damping ratio of 0.08 and 0.04 for the simulated

α and B1 whisker, respectively, are well within observed biological variability.
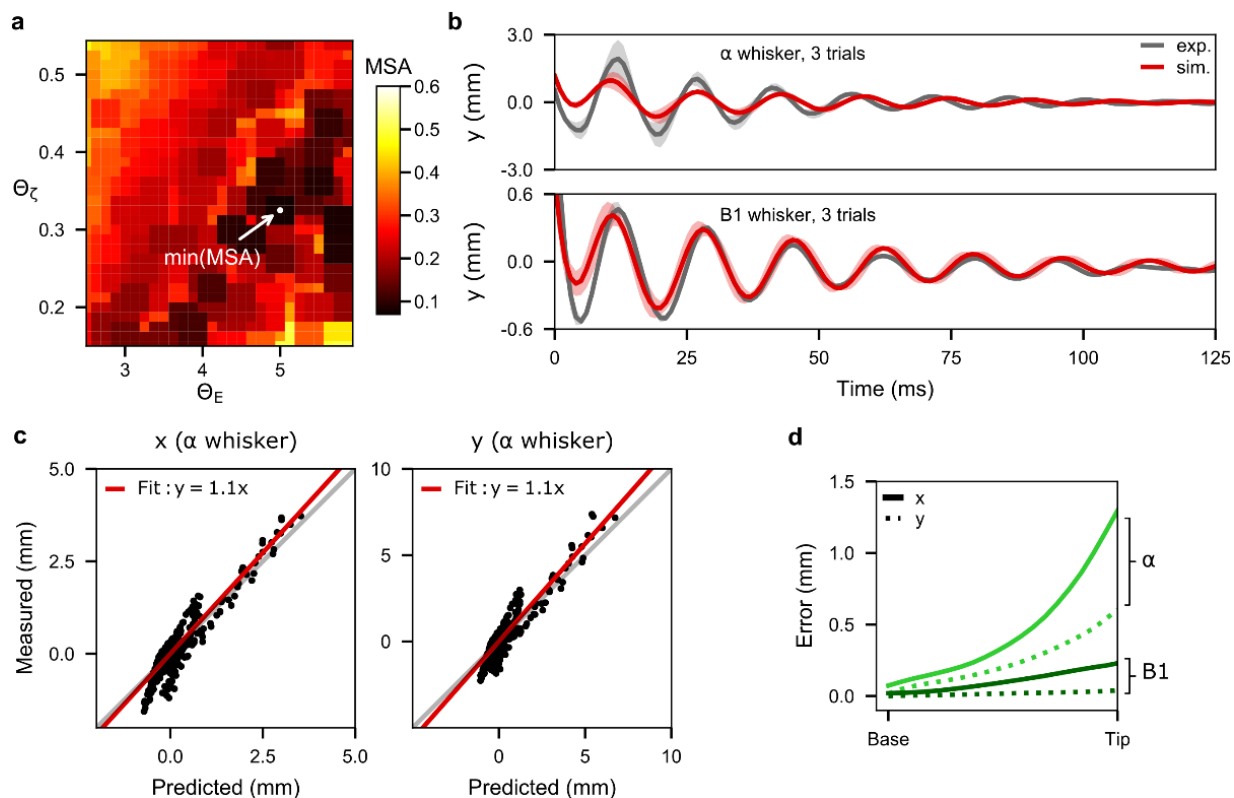


**Figure 3-8. Parameter optimization with a single whisker yields good match with experimental data.** **(a)** Error surface generated by optimizing the parameters $\theta_\zeta$ and $\theta_E$. Color represents error between simulated and experimental data. Note the linear relationship between $\theta_E$ and $\theta_\zeta$, reflecting the tradeoff between fitting the resonance frequency and fitting the log-decrement. **(b)** Averaged trajectory of the whisker tip in the y-direction for three trials in which the α and B1 whiskers were driven at the same speed in experiment and simulation. The variability indicated by the standard deviation across the trials occurs because the motor angle is non-deterministic. **(c)** Measured versus predicted trajectory (x- and y- coordinates) of the α whisker tip in the horizontal plane over all trials used for the optimization. **(d)** Displacement error increases as a function of link position (distance from whisker base). Note that the error of the tip, which was used for optimization, is largest; error decreases rapidly to less than 0.3 mm at 50% of the whisker length. Data are shown for the α (green) and B1 (black) whiskers; x- and y- coordinates are shown as dashed and solid lines, respectively.

Whiskers with dimensions similar to those of the α whisker have first-mode resonance frequencies between 59 – 83 Hz; for whiskers with dimensions similar to B1, between 50 – 59 Hz (Hartmann, Johnson et al. 2003, Neimark, Andermann et al. 2003). The damping ratio calculated from the kinematic behavior of the whisker is smaller than the optimized value for parameter $\theta_\zeta$. This difference is likely attributable to the assumption that the damping ratio is uniform along the whisker, as previous studies have suggested that the damping ratio decreases from base to tip (Hartmann, Johnson et al. 2003, Boubenec, Shulz et al. 2012, Vaxenburg, Wyche et al. 2018).

**Table 3-3. Dynamic measurements of experiment and optimized simulation.**

| Variable and units | whisker | Experiment | Simulation | Absolute Error |
|---|---|---|---|---|
| $f_n$ (Hz) | α | 67.6 (±0.72) | 64.87 (±1.12) | 2.73 (±1.28) |
| | B1 | 59.38 (±0.44) | 58.96 (±0.68) | 0.86 (±0.61) |
| $\delta$ (dimensionless) | α | 0.32 (±0.23) | 0.50 (±0.4) | 0.26 (±0.37) |
| | B1 | 0.25 (±0.08) | 0.23 (±0.08) | 0.04 (±0.06) |
| $\zeta$ (dimensionless) | α | 0.05 (±0.04) | 0.08 (±0.06) | 0.04 (±0.06) |
| | B1 | 0.04 (±0.01) | 0.04 (±0.01) | 0.01 (±0.01) |

Matching material properties between simulation and experiment does not guarantee that simulated dynamics will accurately match experimental data. Nevertheless, simulated trajectories of the whisker tip closely followed experimentally obtained trajectories (Figure 3-8b). The high accuracy of the predictions is confirmed by a fit close to the identity line in Figure 3-8c for the α whisker, with a slope of 1.1 for both x- and y- coordinates. Results for the B1 whisker were similar but had a slightly larger bias in the y direction, with a slope of 1.3. High Pearson correlation coefficients for both whiskers, α (x: 0.92, y: 0.92) and B1 (x: 0.99, y: 0.78) also indicate a close match between simulation and experiment for both whiskers. Note that the trajectory error shown in Figure 3-8b and Figure 3-8c are the largest observed, because the error increases with the distance to the actuation point, i.e., the whisker base (Figure 3-8d). The maximum error at the tip

is 1.6 mm and decreases rapidly to less than 1 mm at 80% of the whisker length. At 50%, the error

is already less than 0.3 mm and nearly zero (< 0.1 mm) at the base.

### 3.6.3.2  Optimization of damping properties of the follicle

The *ex vivo* model described above assumes that the whisker is rigidly anchored in the follicle

(Figure 3-9a, rigid base).  However, a preliminary analysis indicated that simulations assuming a

rigid follicle generated deflections that were nearly an order of magnitude larger than those

observed in Experiment 2 (whisker deflections *in vivo* in the anesthetized animal.).   The

discrepancy between rigid-base simulations and experimental results are clearly shown in Figure

3-9; the experimental trajectory of the whisker tip was considerably more damped than for the

rigidly anchored whisker simulations.

We therefore aimed to incorporate elasticity at the whisker base, simulating the insertion of the

whisker-follicle complex into compliant skin tissue (Figure 3-9a, compliant base).  We added two

identical torsional springs about the y and z axis of the base of the whisker to account for the

compliant tissue properties of the follicle.

In contrast to the original single whisker model, the stiffness and damping parameters of the

torsional spring-damper system in the follicle are not directly related to any specific material

properties. These parameters were instead optimized using similar procedures as for the

optimization of model parameters $\theta_E$ and $\theta_\zeta$.  Randomly selected trials from the B1, B2, and D2

whiskers from Experiment 2 were used for this optimization.   Because the oscillations of the

whiskers in Experiment 2 were very small, the logarithmic decrement $\delta$ was difficult to measure.

The error metric was therefore adjusted to include only the error in FRF and the error in the

magnitude of the first two adjacent peaks $y_0$ and $y_1$ of the whisker tip oscillations (eq. S4b).
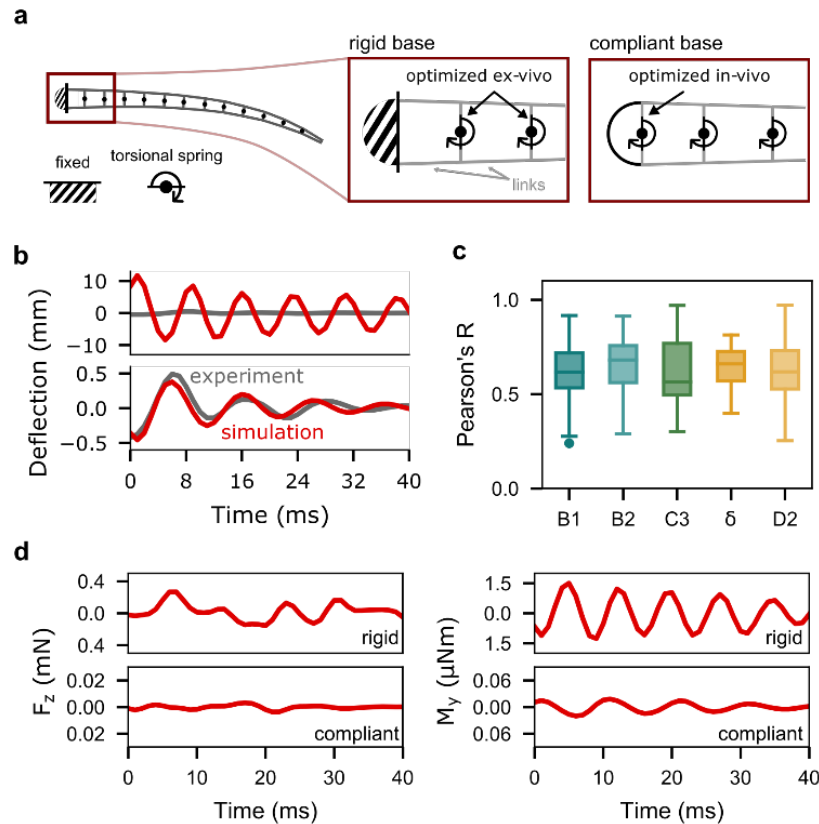
**Figure 3-9. Mechanical properties of the follicle significantly affect whisker dynamics and mechanical signals at the whisker base. (a)** Schematic of the single-whisker model and the constraints used for the rigid base (fixed) and the compliant base (torsional spring). The red square indicates the magnified part to the right. A whisker attached to a motor was used to optimize the torsional springs connecting the individual links of the whisker body while the base was fixed (middle). In a second step the fixed constraint at the base was replaced with a torsional spring that was optimized using deflection data from an in-vivo experiment (right). **(b)** Displacement of the whisker tip of a representative trial in which the B1 whisker was deflected. The grey traces in both panels show the oscillations measured experimentally, which include the compliant properties of the follicle. The red traces show simulation results when assuming a rigid follicle condition for experiment (upper panel) and after incorporating the compliant properties of the follicle (lower panel). Note the change in vertical scale between panels. **(c)** Pearson correlation between experimental and simulated trajectory of the most distal link for five different whiskers, labeled on the x-axis, pooled over horizontal and vertical directions. Simulated trajectories were obtained in compliant conditions. Distributions were computed across all trials for each whisker. R = 0.61 (±0.14) for B1 whisker, R = 0.66 (±0.15) for B2 whisker, R = 0.61 (±0.19) for C3, R = 0.63 (±0.12) for D0 whisker, and R = 0.61 (±0.12) for D2 whisker. **(d)** Force in bending direction $F_z$ (left), and moment about the bending axis $M_y$ (right), in rigid (upper panel) and compliant (lower panel) follicle condition. Note the change in vertical scale between panels.

$$MSA(\theta_E, \theta_\zeta) = exp\left\{median\left(\left|\ln\left(\frac{FRF_{sim}(\theta_E,\theta_\zeta)}{FRF_{exp}(\theta_E,\theta_\zeta)}\right)\right|, \left|\ln\left(\frac{y_{0,sim}(\theta_E,\theta_\zeta)}{y_{0,exp}(\theta_E,\theta_\zeta)}\right)\right|, \left|\ln\left(\frac{y_{1,sim}(\theta_E,\theta_\zeta)}{y_{1,exp}(\theta_E,\theta_\zeta)}\right)\right|\right)\right\} - 1 \qquad \text{(eq. S4b)}$$

For each parameter combination, three trials were randomly sampled for each whisker and the MSA computed according to eq. S4b. The optimal parameter values were determined by finding the minimum error across all simulated parameter combinations.

After optimization, the trajectory of the whisker much more closely resembled the experimental data (Figure 3-9b, bottom panel). In addition, as shown in Figure 3-9c, the Pearson correlation coefficients between experiment and simulation for both horizontal and vertical deflections for each whisker achieve an average R value of 0.63 (±0.15). These results indicate that the model can robustly predict dynamics at the whisker tip after accounting for the compliant properties of the follicle embedded within the tissue.

As expected, the difference between rigid and compliant follicle is also evident in the mechanical signals predicted to occur at the whisker base. Figure 3-9d shows an example of the forces in bending direction ($F_z$) and moment about the axis of rotation ($M_y$) for a B1 whisker, corresponding to the tip trajectory in Figure 3-9b. Compared to the rigid follicle model, the compliant follicle model reduces $F_z$ and $M_y$ by more than an order of magnitude while it also exhibits low pass properties smoothing the mechanical response (bottom plots).

**3.6.4 Supplemental Videos**

**Movie 1. Visualization of the passive stimulation experiment (Scenario 1).**
A vertical peg was simulated to move from rostral to caudal through the middle of the immobile right array. The peg moves at constant speed (0.3 m/s) from rostral to caudal. The right upper panel displays the visualization of the 3D simulation, showing the rat head and the right whisker array. The upper left quadrant shows two illustrations of the mystacial pad, each circle representing a follicle. The color scale on the left indicates the magnitude of the of the bending moment $M_b$ ($= \sqrt{M_y^2 + M_z^2}$) whereas the color scale on the right indicates the magnitude of the transverse force $F_t$ ($= \sqrt{F_y^2 + F_z^2}$) generated at the base of each whisker. Underneath, the whisker basepoints are plotted in 3D (white dots), while the 3D vectors of the mechanical signals are superimposed at each basepoint. Note that the view angle is different from the visualization. The bottom left panel shows $M_b$ (same color scale) evolving over time for each of the whiskers (y-axis). The bottom right panel shows the point of contact for each whisker over time, indicated by the grey color scale. The point of contact is normalized to the length of the whisker, i.e., tip = 1.0.

**Movie 2. Visualization of active whisking against two vertical pegs (Scenario 2).**
Same as in Movie 1, but instead of a single sweep through the entire array, the peg oscillates back and forth between its start and end positions in the middle of the array, to repeatedly stimulate the array eight times per second (8Hz). This scenario was carefully designed to replicate as closely as possible the stimulation distances, velocities, and frequencies associated with active whisking (Scenario 3).

**Movie 3. Visualization of active whisking against two vertical pegs (Scenario 3).**
Simulation of active whisking against a fixed, vertical peg. Each whisker is driven at its base according to established kinematic equations for whisking motion (19). One cycle of protraction and retraction of the array lasts 125 ms, equivalent to a whisking frequency of 8 Hz. The peg is positioned laterally, 20 mm from the midline of the head with an offset of 10 mm from the nose tip.

**Movie 4. Visualization of natural environment experiment (Scenario 4).**
Whiskers perform the identical whisking motion as in Movie 3 (Scenario 3), but the array is positioned in front of the opening of a 3D scan of a drainpipe, so that the rat is simulated to actively palpate a typical object found in its natural habitat.

**Dataset 1 (separate file).**
Experimental data used in Figure 3-1 in the main text. The dataset consists of three different datasets compiled from the literature; they include measurements of whisker resonances and whisker arc length. The first dataset is from Hartmann et al., 2003, including data of 24 whiskers from one rat (Hartmann, Johnson et al. 2003). The second from Wolfe et al., (2008) consisting of

22 whiskers (δ, D1, D2, D3, D4) from four different rats (Wolfe, Hill et al. 2008). The third dataset is from Neimark et al. (2003) providing resonance frequencies of 10 whiskers of the C-row (left and right) measured both in vivo and ex vivo (Neimark, Andermann et al. 2003).

# CHAPTER 4

## Statistical characterization of tactile scenes in three-dimensional environments reveals filter properties of somatosensory cortical neurons

Nadina O. Zweifel[1], Sara A. Solla[2,3], and Mitra J. Z. Hartmann[1,4]

[1]Department of Biomedical Engineering, Northwestern University, Evanston, IL, 60208, USA
[2]Department of Physics and Astronomy, Northwestern University, Evanston, IL, 60208, USA
[3]Department of Neuroscience, Northwestern University, Chicago, IL, 60611, USA
[4]Department of Mechanical Engineering, Northwestern University, Evanston, IL, 60208, USA

## 4.1 Abstract

Natural scenes statistics have been studied extensively using collections of natural images and sound recordings. These studies have yielded important insights about how the brain might exploit regularities and redundancies in visual and auditory stimuli. In contrast, natural scenes for somatosensation have remained largely unexplored. Here we use three-dimensional scans of natural and human-made objects to quantify natural scene statistics at the scale of the human fingertip. Using measurements of distance, slope, and curvature from the object surfaces, we show that the first order statistics follow similar trends as have been observed for images of natural and human-made environments. In addition, independent component analysis of curvature measurements reveals Gabor-like basis vectors similar to those found in natural images. A simple neural model using these filters showed responses that accurately capture the statistics of responses in primate primary somatosensory cortex.

**4.2 Introduction**

An animal's only access to the environment is through the signals provided by the activation of its sensors as they interact with the external world. These sensory signals typically represent compressed and nonlinear transformations of physical quantities in the environment. Nonetheless, nervous systems can efficiently and reliably infer relevant information about the original environmental variables from the sensory input signals they evoke. It has been hypothesized that these successful inferences are achieved by exploiting regularities and redundancies present both in the environment and in the resulting sensory input signals (Attneave 1954, Barlow 1961).

Over the last five decades, a large body of research on the statistics of visual and auditory natural scenes has generated strong evidence in support of this hypothesis (Field 1987, Atick and Redlich 1992, Olshausen and Field 1996, Ruderman, Cronin et al. 1998, Lewicki 2002, Hafner, Fend et al. 2003, Smith and Lewicki 2006, Barnett, Nordstrom et al. 2010, Hyvärinen 2010, Evans 2013, Hausler, Susemihl et al. 2013, Stansbury, Naselaris et al. 2013, Manfredi, Saal et al. 2014, Parise, Knorre et al. 2014, Traer and McDermott 2016, Dyakova and Nordstrom 2017, Huang and Elhilali 2017, Samonds, Geisler et al. 2018, Dodds and DeWeese 2019). Statistical models that predict the coding schemes and representations characteristic of cortical neurons (basis functions, basis vectors, receptive fields) have received considerable attention, and different algorithms to fit the models to sensory data have been proposed (Olshausen and Field 1996, Van Hateren and Ruderman 1998, Hoyer and Hyvärinen 2000, Hyvärinen and Hoyer 2000, Hyvärinen and Hoyer 2001, Lewicki 2002, Hyvarinen, Gutmann et al. 2005, Smith and Lewicki 2006, Hyvärinen 2010). The underlying assumption of these models is that sensory systems process incoming information by simultaneously activating a small subset of neurons while the majority remain silent. Some modeling approaches directly impose this constraint by maximizing the sparseness of the

optimized representations (sparse coding) (Olshausen and Field 1996), while others indirectly achieve similar results by maximizing the independence of the predicted basis functions (independent component analysis) (van Hateren and van der Schaaf 1998, Lewicki 2002).

The data used to train these models typically originate from a collection of natural scenes in the form of visual images or sound recordings; these represent the ensemble of inputs that the sensory system may encounter. For images, a large number of small regions within these images is then used to mimic receptor-like sampling of the scene. The basis functions that emerge from the fitted model thus represent the features of the sensory signal encoded by individual cortical neurons; these have been found to be very similar to cortical receptive fields recorded experimentally (Olshausen and Field 1996, van Hateren and van der Schaaf 1998, Lewicki 2002). The features thus selected can give insight into the neural tuning that gives rise to an efficient code. In vision, these features resemble edge detectors and Gabor filters (Olshausen and Field 1996, van Hateren and van der Schaaf 1998, Hyvärinen and Hoyer 2001).

In contrast to vision and audition, the natural scene statistics of somatosensation have remained largely unexplored (Hafner, Fend et al. 2003, Evans 2013, Manfredi, Saal et al. 2014, Hobbs, Towal et al. 2015). Tactile sensors are unique in that the signals they acquire result from direct physical contact with the environment: it is impossible to "feel" an object without touching it. The interactive nature of touch makes tactile environmental statistics extremely challenging to quantify, as evidenced by the small number of studies that have attempted to measure these parameters *in vivo* (Manfredi, Saal et al. 2014) or *in silico* (Hafner, Fend et al. 2003, Evans 2013, Saal, Delhaye et al. 2017). To date, psychophysical, neurophysiological, and self-report experiments have primarily focused on the physical and qualitative dimensions of tactile perception in the environment (e.g., roughness, smoothness, compliance, curvature, etc.)

(Srinivasan and Lamotte 1991, Lamotte, Srinivasan et al. 1994, Goodwin, Macefield et al. 1997, Khalsa, Friedman et al. 1998, van der Horst and Kappers 2008, Shao, Chen et al. 2010, Cheeseman, Norman et al. 2016, Sakamoto and Watanabe 2017). Despite substantial groundwork from these studies, the environmental statistics of somatosensation are still poorly documented (Hobbs, Towal et al. 2015).

The present study aims to shed light on the environmental statistics of the natural *tactile* scene by quantifying geometrical properties of the natural environment in three-dimensional (3D) space. We focus specifically on three different Cartesian-based metrics: local distance, slope, and curvature. We begin by quantifying the statistics of each of these metrics at the level of individual objects as well as the entire population of objects, and then use independent component analysis (ICA) in two different ways. First, ICA is used to find the leading statistically independent dimensions in local distance measurements, revealing that 95% of the variance in local distance data is predominantly accounted for by curvature. Second, ICA is used to estimate the filter characteristics of somatosensory cortical neurons. This analysis shows that the ICA basis vectors estimated from curvature patches have Gabor-like filter properties and are consistent with orientation sensitivity found in neurons in areas 1 and 3b of primary somatosensory cortex (S1).

## 4.3 Results

We collected 3D representations of 96 natural objects such as rocks, leaves, bark, fruits, vegetables, etc., as well as 41 human-made objects including scissors, knifes, purses, mugs, etc. (Figure 4-1ab). To quantify the local shape of these data, we randomly sampled 100-150 circular surface patches with a radius of 6 mm, similar to the size of a human fingertip (van Kuilenburg, Masen et al. 2013) (Figure 4-1c, *left*). This procedure resulted in a total of 12,309 and 5,788 patches for natural and human-made objects, respectively. For each surface patch we computed maps of

distance, slope, and curvature; details for calculating these metrics are found in *Methods*. Briefly,

the distance of the surface points was computed with respect to a reference plane (Figure 4-1c,

*middle*), yielding a circular distance map $P(D)$ with a total of 448 points for each patch. From
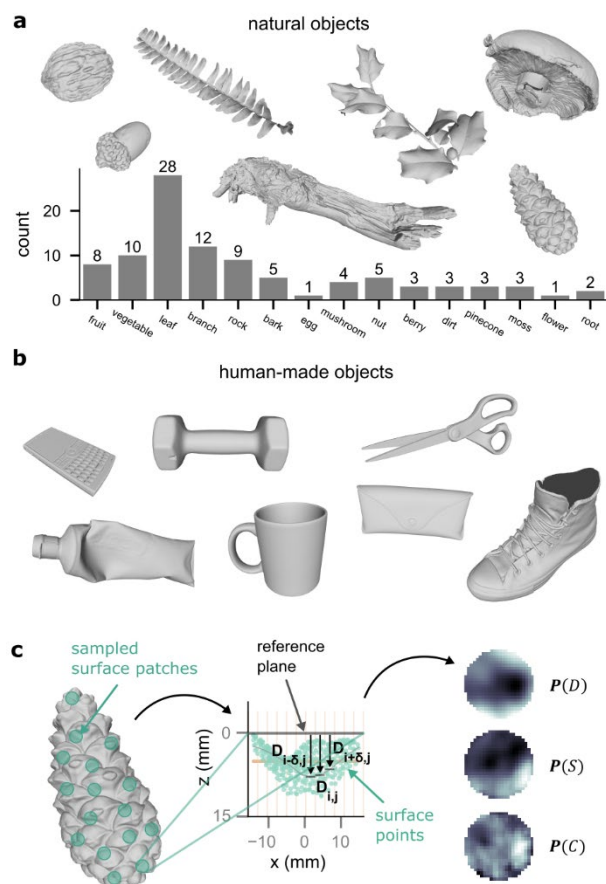


**Figure 4-1. The 3D datasets include a total of 96 natural objects and 41 human-made objects, cleaned and processed following procedures described in *Methods*. (a)** Examples of 3D scanned natural objects, and a histogram of the number of objects in each of 15 categories. **(b)** Examples of 3D scanned human-made objects. **(c)** To sample the 3D data, approximately 100-150 circular surface patches were randomly selected from each object (left). For each surface patch, the distance of the surface points was measured with respect to a reference plane (middle). From these measurements, a circular distance map $P(D)$ of 448 points was created (right). Using forward and central differencing, a 421-dimensional slope map and a 384-dimensional curvature map, $P(S)$ and $P(C)$, were computed for each patch (see *Methods*).

$P(D)$ we computed a 421-dimensional slope map $P(S)$ using first-order forward difference, and a 384-dimensional curvature map $P(C)$ using second-order central difference. Examples of $P(D)$, $P(S)$, $P(C)$ for an example patch are shown on the right in Figure 4-1c.

### 4.3.1 First-order statistics of natural and human-made objects

We examined the first-order statistics of natural and human-made objects in terms of the local metrics: distance, slope, and curvature ($D$, $S$, and $C$). Figure 4-2a compares the probability distributions of these metrics for two natural objects (bark, leaf) and two human-made objects (mug, purse). The distributions were computed from all patches for each object. As expected, human-made objects tend to have larger flat and low-curvature regions (e.g., the body of the mug); the probability distributions for all three metrics are correspondingly skewed towards zero. At the same time, small distinct regions of human-made objects exhibit higher curvature values (e.g., rim and handle of the mug) that affect the shape of the corresponding distributions. The effect of the rim and handle of the mug is particularly obvious in the distribution of $C$, in which additional modes appear at large positive and negative values. In contrast, the distributions for natural objects are clearly unimodal with a smooth decay towards the tails, indicating that the measured local metrics are more continuous across the surface than for human-made objects.

To generalize this analysis, we computed the average probability distributions across all $P(\cdot)$ for each metric (Figure 4-2b). Both natural and human-made objects result in super-Gaussian distributions, i.e., distributions with higher peaks at zero and heavier tails than a Gaussian distribution with the same mean and variance. Although the average distributions for human-made objects smooth over irregularities present in the distributions for individual human-made objects, the average distributions for human-made objects remain heavily skewed towards zero and are significantly different from the distributions for natural objects distance $D$ (Kolmogorov-Smirnov

test: D = 0.303, p < 0.001), slope $S$ (Kolmogorov-Smirnov test: D = 0.100, p < 0.001), and curvature $C$ (Kolmogorov-Smirnov test: D = 0.149, p < 0.001).
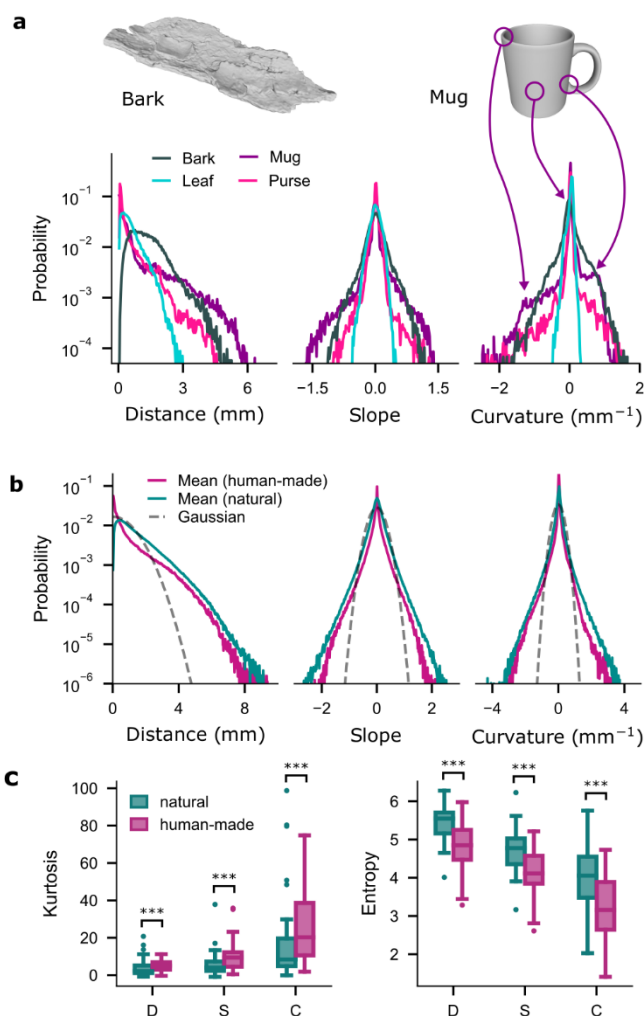


**Figure 4-2. Probability distributions of the three metrics $D$, $S$, and $C$ for both natural and human-made objects. (a)** Four example objects (two illustrated, not to scale) and their corresponding distributions of $D$ (left), $S$ (middle), and $C$ (right). Distributions were computed from the ensemble of patches with $R = 6$ mm associated with each object. Note that the vertical axis is logarithmic. **(b)** Average probability distribution of $D$ (left), $S$ (middle), and $C$ (right) across all sampled patches with $R = 6$ mm for natural (turquoise) and human-made (magenta) objects. The black dashed lines show a zero-mean Gaussian distribution of the same variance for comparison. Only the positive half of the Gaussian is used for distance $D$. **(c)** Distributions of kurtosis (left) and entropy (right, measured in bits) for the distribution for each object class and each metric.

Differences between natural and human-made objects can also be quantified in terms of kurtosis: human-made objects result in significantly higher kurtosis values than natural objects (Figure 4-2c, left) in terms of $D$ (Mann-Whitney rank test: U = 1029, p < 0.001), $S$ (Mann-Whitney rank test: U = 892, p < 0.001), and $C$ (Mann-Whitney rank test: U = 984, p < 0.001). The average distributions of $D$, $S$, and $C$ have kurtosis values of 2.8, 6.1, and 17.9 for natural objects, and 4.4, 8.9, and 24.3 for human-made objects, respectively. Kurtosis is related to regularity (correlations) in the data and is inversely related to entropy, i.e., high kurtosis values correspond to low entropy, shown in the right panel of Figure 4-2c. Entropy is significantly lower for human-made objects than for natural objects for all three metrics $D$ (Mann-Whitney rank test: U = 508, p < 0.001), $S$ (Mann-Whitney rank test:, U = 791: p < 0.001), $C$ (Mann-Whitney rank test: U = 696, p < 0.001). From an information-theoretical perspective, this result suggests that fewer bits are necessary to encode information about human-made objects than for natural objects when the objects are characterized through the chosen metrics $D$, $S$, and $C$. In addition, the right plot in Figure 4-2c also indicates that entropy decreases with the order of the derivative: $D$ results in higher entropy and $C$ in lower entropy across individual objects. This result implies that a metric such as $C$ may provide more regularities that could potentially be exploited by a sensory system to efficiently encode information about tactile images present in the world.

### 4.3.2 ICA analysis for the various metrics

The first-order statistics of three local metrics that characterize the shape of $R$ = 6mm surface patches: distance, slope, and curvature are highly regular and super-Gaussian, congruent with the statistics observed in natural images (Ruderman 1994, Huang, Lee et al. 2000). However, it remains unclear which of these metrics may be the best candidate to provide information about the world to a tactile sensory system. To investigate this question, we used an unsupervised learning

algorithm, Independent Component Analysis (ICA), to identify the fundamental features of natural data in terms of distance $D$, the least processed metric that characterizes local shape.

As described in (Bell and Sejnowski 1995), ICA is a linear model that maps a data vector $\boldsymbol{x}$ consisting of a set of features $[x_1, \dots, x_n]$ to a set of components $\boldsymbol{s} = [s_1, \dots, s_n]$ through a square mixing matrix $\boldsymbol{A}$, such that the sensory signal $\boldsymbol{x}$ can be linearly reconstructed from the components by

$$\boldsymbol{x} = \boldsymbol{A}\boldsymbol{s}. \qquad \text{eq. (1)}$$

Both the mixing matrix $\boldsymbol{A}$ and the components $\boldsymbol{s}$ are unknown. The matrix $\boldsymbol{A}$ is estimated from the statistics of the observed data vectors $\boldsymbol{x}$ under the assumptions that $\boldsymbol{A}$ is square, the components $\boldsymbol{s}$ are statistically independent, and $\boldsymbol{x}$ can be reconstructed linearly (Hyvärinen and Oja 2000). The independent components $\boldsymbol{s}$ are then obtained by using the matrix $\boldsymbol{W}$, the inverse of $\boldsymbol{A}$:

$$\boldsymbol{s} = \boldsymbol{W}\boldsymbol{x}. \qquad \text{eq. (2)}$$

The columns in $\boldsymbol{A}$ are called basis vectors; each basis vector is associated with one of the components in $\boldsymbol{s}$. The rows in $\boldsymbol{W}$ play the roles of filters that act on the data vector $\boldsymbol{x}$ to obtain the corresponding component (van Hateren and van der Schaaf 1998). The matrix $\boldsymbol{W}$ contains the coefficients or weights for each of the features in $\boldsymbol{x}$ to recover each independent component in $\boldsymbol{s}$. The set of weights associated with a particular component $s_i$, which correspond to the $i$th row of $\boldsymbol{W}$, can thus be interpreted as the receptive field for that component (van Hateren and van der Schaaf 1998). In contrast, the column basis vectors in $\boldsymbol{A}$ represent fundamental features that can be linearly combined to compose the observed signal $\boldsymbol{x}$. The amplitude of each such feature is determined by the coefficients of the corresponding component of $\boldsymbol{s}$; these components are

typically sparsely distributed (van Hateren and van der Schaaf 1998). There are many different ways to implement ICA; we used one of the most popular and computationally efficient algorithms, FastICA, proposed by Hyvarinen and Oja (Hyvärinen and Oja 2000).

In our scenario, $x$ represents a 448-dimensional vector of distances from a map $P(D)$ sampled from a natural object. Examples of $P(D)$ used for fitting the ICA model are shown in Figure 4-3a.The FastICA algorithm does not sort the estimated basis vectors (columns of $A$), so we used a sorting algorithm proposed by Cheung and Xu (Cheung and Xu 2001) to order the basis vectors according to their contribution to reconstruction accuracy. The first 100 of the sorted basis vectors are shown in Figure 4-3b. The cumulative reconstruction accuracy as sorted basis vectors are added is shown in Figure 4-3c; this plot indicates that the leading 113 basis vectors suffice to achieve a reconstruction accuracy of 0.95. Based on this result, we determined the filtering properties of the leading 113 basis vectors by convolving each of them with a test image (Figure 4-3d, *left inset*). The convolution output allowed for a categorization of the basis vectors into $1^{st}$, $2^{nd}$, and $3^{rd}$-order derivative filters. Examples of each category with the corresponding convolved images are shown in Figure 3d. Note that $1^{st}$-order filters, associated with slope, are notably scarce, rising slowly in number as basis vectors are added. Within the first 113 basis vectors, only four $1^{st}$-order filters were present (Figure 4-3e). In contrast, $2^{nd}$-order filters, associated with curvature, were the most common.

To further assess the relevance of the different types of basis vectors, each category was separately tested for reconstruction accuracy. The $2^{nd}$-order category resulted in significantly smaller reconstruction error than either the $1^{st}$-order (Mann-Whitney rank test: U = 18042, p < 0.001) or $3^{rd}$-order categories (Mann-Whitney rank test: U = 1507754, p < 0.001). Unsurprisingly,
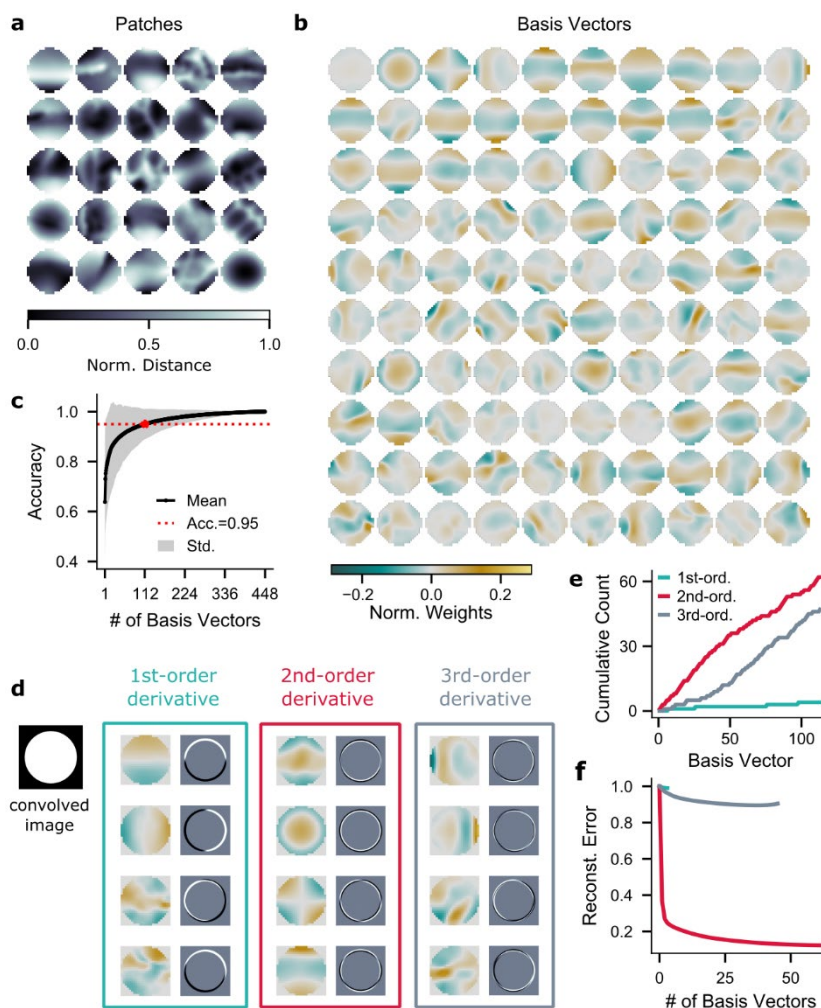
**Figure 4-3. Basis vectors estimated by ICA for surface patches characterized by distance $D$ to the reference plane. (a)** Example surface patches ($R = 6$mm) randomly sampled from natural 3D data that show spatial maps of the distance $D$. Grey scale is normalized to maximum distance within each patch. **(b)** The leading 100 basis vectors (columns of the mixing matrix $A$) as estimated by ICA from the distance $D$ data. The mean was subtracted from each basis vector, and the norm of each basis vector was scaled to 1. The basis vectors are sorted by their contribution to reconstruction accuracy as shown in (c). **(c)** Cumulative reconstruction accuracy of the sorted basis vectors. **(d)** The basis vectors are classified as $1^{st}$, $2^{nd}$, or $3^{rd}$ order by convolving each with a simple image: a white circle on black background (left). Representative examples selected from the first 113 basis vectors are shown in the three boxes. *Left box*: basis vectors with $1^{st}$-order derivative characteristics in detecting the change in distance $D$ (slope). *Middle box*: basis vectors with $2^{nd}$-order derivative characteristics in detecting the rate of change in distance $D$ (curvature). *Right box*: basis vectors with $3^{rd}$-order derivative characteristics (change in curvature). **(e)** Cumulative count of basis vectors for each category shown in (d). **(f)** Reconstruction error of the basis vectors for each category identified in (d). The basis vectors in each category are sorted by their contribution to the reconstruction error.

reconstruction accuracy for the 1$^{st}$-order category was by far the lowest of the three (Median = 0.003).

Within the first 113 leading basis vectors, the 1$^{st}$-order category includes a total of 4 basis vectors, the 2$^{nd}$-order category includes 62, and the 3$^{rd}$-order category includes 47 basis vectors. Given that reconstruction accuracy typically correlates with the number of basis vectors, one possibility is that the differences in reconstruction error between categories may just be an artifact of the different number of basis vectors in each category. However, sorting the basis vectors in each category by their contribution to the reconstruction error, we find that there is an intrinsic difference in the amount of information carried by the basis vectors in each category. The results in Figure 4-3f show that the reconstruction error drops the fastest with additional basis vectors for those in the 2$^{nd}$-order category while the slowest for those in the 1$^{st}$-order category. This result indicates that the 2$^{nd}$-order basis vectors carry more information about the original patch than the 1$^{st}$ or 3$^{rd}$ order basis vectors. Thus, even though the number of basis vectors in each category does affect the reconstruction accuracy, the order of the basis vector plays a significant role in the observed reconstruction errors shown in Figure 4-3f.

### 2.3. Tactile coding model based on curvature information

Sparse coding and ICA are powerful statistical models that seem to capture aspects of the coding strategies in visual as well as auditory cortices (Olshausen and Field 1996, van Hateren and van der Schaaf 1998, Lewicki 2002). The sparse coding algorithm originally introduced by Olshausen and Field (1997) used data from natural images to estimate basis functions that had striking similarities to the receptive fields of simple cells in the primary visual cortex (Olshausen and Field 1997).

Because the ICA results identified curvature as a good candidate to represent 3D shape information, we used a similar approach and applied the FastICA algorithm to the 384-dimensional curvature maps $P(C)$ of natural objects. Examples of $P(C)$ used to obtaining the ICs are shown in
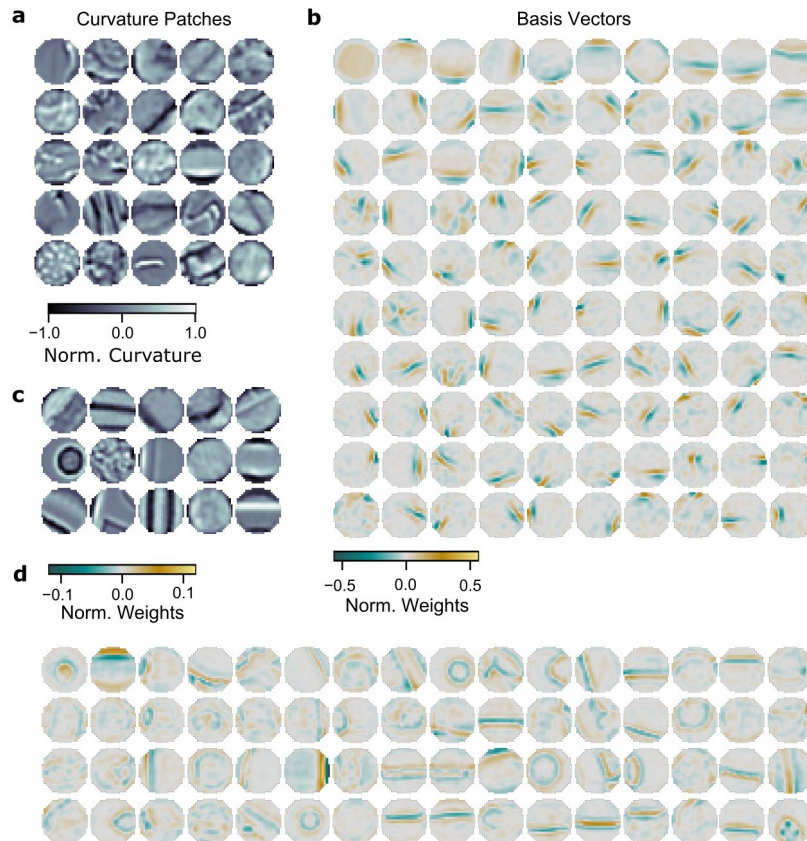


**Figure 4-4. Basis vectors estimated by ICA for surface patches characterized by curvature $C$. (a)** Example surface patches ($R = 6$ mm) randomly sampled from natural 3D data that show spatial maps of the curvature $C$. Grey scale is normalized to the maximum absolute value of the curvature within each patch. **(b)** The leading 100 basis vectors (columns of mixing matrix $A$) as estimated by ICA from the curvature $C$ of natural 3D data shown in (a). The mean of each basis vector was subtracted, and the norm of the basis vectors was scaled to 1. **(c)** Same as (a) but for human-made 3D data. **(d)** Subset of 64 basis vectors (columns of mixing matrix $A$) as estimated by ICA from curvature $C$ of human-made 3D data shown in (c). The mean of each basis vector was subtracted, and the norm of the basis vectors was scaled to 1.

Figure 4-4a. The leading 100 basis vectors for the curvature map, sorted again by the method proposed in (Cheung and Xu 2001), are shown in Figure 4-4b. In contrast to the results for the

distance-based analysis (Figure 4-3b), the basis vectors for the curvature map show localized

Gabor-like properties similar to those found for natural images (Olshausen and Field 1996, van

Hateren and van der Schaaf 1998). This result is consistent with experimental work that identified

oriented Gabor filters as good predictors for the filter properties of S1 neurons (DiCarlo and

Johnson 2000, Bensmaia, Denchev et al. 2008).

Even more importantly, the same analysis applied to data for human-made objects (Figure 4-4c)

does not generate basis vectors with localized, Gabor-like patterns (Figure 4-4d). Instead, basis

vectors estimated from human-made objects have very regular characteristics, extending across

the entirety of the patches and are even sometimes curved. Notably, these basis vectors seem to

mimic the geometrical properties of the original curvature patches sampled from human-made

objects (see Figure 4-4c-d). Thus, although the first-order statistics of natural and human-made

objects are similar (Figure 4-2), these objects clearly differ in their second-order statistics.

### *4.3.2.1 Filter properties of S1 model neurons*

To test whether the curvature-based basis vectors identified above might be associated with filter

properties of S1 neurons, we used the neural model of Bensmaia et al. (Bensmaia, Denchev et al.

2008) to investigate the orientation selectivity of the corresponding ICA filters (rows of unmixing

matrix $W$). The proposed neural model (Bensmaia, Denchev et al. 2008) is described by the

equation:

$$R(x) = \left| \alpha \left( f_\phi * x \right) + \beta \right| \qquad \text{eq. (3)}$$

where $x$ is the stimulus, $R(x)$ is the neural response, $f_\phi$ is a filter characterized by a set of

parameters $\phi$, and $\alpha$ and $\beta$ are scalar coefficients. The * operator symbolizes convolution; the

parameters $\phi$, $\alpha$, and $\beta$ are fit to model the response of each neuron. Bensmaia et al. (Bensmaia,

Denchev et al. 2008) showed that the use of Gabor filters for $f_\phi$ accounted for 57% to 68% of the

variance in individual neural responses.
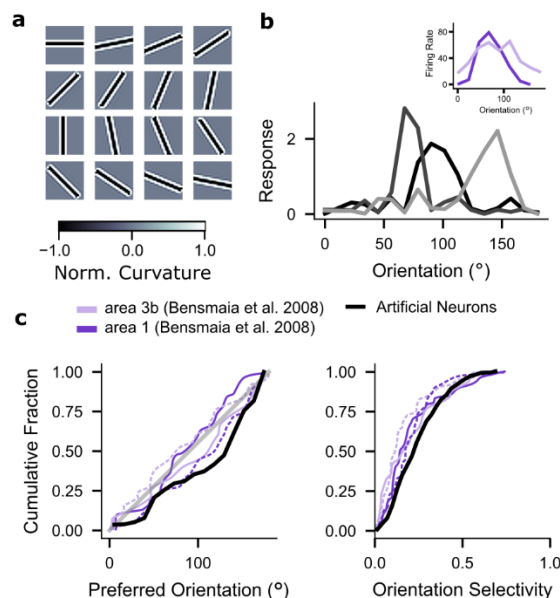


**Figure 4-5. Orientation selectivity of model neurons based on ICA filters. (a)** Curvature maps of the bar stimuli used to test artificial neurons based on ICA filters for the curvature analysis of natural objects. The orientation varies between 0 (top left) and 168.75 degrees (bottom right) in steps of 11.25 degrees. **(b)** Responses of three example artificial neurons with the highest orientation selectivity as a function of bar orientation in degrees. *Inset*: Example neurons in area 1 and 3b of S1 from experiments conducted by Bensmaia et al. (Bensmaia, Denchev et al. 2008). **(c)** Cumulative distributions of neural responses across all 384 artificial neurons, each based on one of the ICA filters. *Left:* Cumulative fraction of artificial neurons as a function of their preferred orientation (solid black). Experimental results from area 1 and area 3b in S1 by Bensmaia et al. are shown in purple for bars indented into the fingertip (solid lines) and bars scanned over the fingertip (dashed lines). The 45-degree line representing a uniform distribution is shown in solid grey. *Right*: Same as *left* but cumulative fraction as a function of orientation selectivity.

To test our estimated filters, we generated model neurons by replacing $f_\phi$ with each of the rows

of $W$ as estimated by ICA, and set $\alpha = 1$ and $\beta = 0$. This procedure resulted in a population of

384 artificial neurons, each one based on one of the estimated ICA filters corresponding to the

basis vectors for the curvature analysis of natural objects (the leading 100 of these filters are shown

in Figure 4-4b). To characterize the response of these artificial neurons we generated a set of bar stimuli with 16 different orientations between 0 and 180 degrees, similar to those used in the experiments of Bensmaia et al. (Figure 4-5a). These stimuli, represented in terms of curvature, were used as input to the artificial neurons. For each artificial neuron, we measured the preferred direction, defined as the orientation resulting in maximum neural response, and the orientation selectivity, defined as the ratio of the neuron's response in the preferred direction to its response in all other directions (see *Methods*).

Figure 4-5b shows three artificial neurons that are strongly orientation selective (95th percentile); they have preferred directions at approximately 65, 90, and 145 degrees. Examples of cortical neurons in area 1 and 3b from Bensmaia et al. (Bensmaia, Denchev et al. 2008) are shown in the inset for comparison. The cumulative fraction of the preferred orientation across all artificial neurons is shown in the left panel of Figure 4-5c (black). The experimental results by Bensmaia et al. (Bensmaia, Denchev et al. 2008) are shown in purple, with solid lines indicating neural responses elicited by bars indented into the fingertip and dashed lines indicating neural responses activated by bars scanned across the fingertip. The selectivity of the artificial neurons closely approximates the experimental data in Bensmaia et al. (Bensmaia, Denchev et al. 2008). In the right panel of Figure 4-5c, we compare the cumulative fraction of orientation selectivity of the artificial neurons (black) with that of the recorded S1 neurons (purple, same as in left panel). Although the model neurons have not been fit to any neural data and result only from the statistical analysis of curvatures in natural objects, the cumulative fraction of orientation selectivity shows trends similar to those of neurons recorded in areas 1 and 3b in S1 (Bensmaia, Denchev et al. 2008).

**4.4  Discussion**

The statistical properties of visual scenes have been extensively studied, including studies of the global statistics of images in terms of luminance (Field 1987, Ruderman 1994, Fine, MacLeod et al. 2003), contrast (Field 1987, Ruderman 1994, Brady and Field 2000), and color (Su, Bovik et al. 2011, Nascimento, Amano et al. 2016), as well as contours (Geisler, Perry et al. 2001, Geisler and Perry 2009), occlusion (Lee, Huang et al. 2000, Huang, Lee et al. 2001, Geisler and Perry 2009, Vilankar, Golden et al. 2014), and eye movement (Geisler and Perry 2009). However, all these studies primarily focus on the statistics of two-dimensional (2D) images, as proxies for 2D representations of the retinal image. Only a few attempts have been made to capture and describe the statistics of the 3D visual world (Huang, Lee et al. 2000).

For somatosensation, it is crucial to consider the 3D geometry of the environment with which the sensors interact. The work presented here has taken the first steps to quantify the statistics of 3D natural and human-made tactile scenes at the scale of human touch. The first-order statistics of local shape measurements (distance, slope, curvature) follow trends similar to those previously quantified for both camera and range images. Previous work showed that both these types of images exhibit different first-order statistics for natural (vegetation) and human-made (urban) scenes, mainly showing higher kurtosis for human-made scenes (Lee, Huang et al. 2000). Other work showed that spatial low-frequency components are much more prominent in human-made scenes than in natural scenes (Torralba and Oliva 2003). We observed similar trends in our data.

The ICA analysis of higher order statistics reveals that basis vectors with second-order filter characteristics contribute significantly to accurate reconstruction of the data. These results suggest that curvature is an important metric to represent the 3D shape of objects at the spatial scale of a fingertip. Previous experimental work supports this hypothesis. Experiments in monkeys have

shown that the spike rate of cutaneous mechanoreceptors in the finger pad respond to the amount of curvature and its rate of change, both for slowly adapting and rapidly adapting afferent fibers (Srinivasan and Lamotte 1991, Goodwin, Macefield et al. 1997, Khalsa, Friedman et al. 1998). In addition, areas in human somatosensory cortex have been found to be active during a shape discrimination task that specifically tested for surface curvature (Bodegård, Geyer et al. 2001). A study in macaque inferior temporal cortex found neurons that are tuned to the amount of curvature and to curvature direction (Kayaert, Biederman et al. 2005). Correlations between curvature direction and neural activity were also found in a study that examined shape coding in visual V4 and somatosensory cortices, suggesting that these areas use similar mechanisms to encode shape (Pasupathy, Fitzgerald et al. 2009).

The ICA of natural curvature data revealed basis vectors with Gabor-like characteristics similar to those found for natural images (Olshausen and Field 1997). Further analysis with a simple model based on artificially generated neurons that use the IC filters showed simulated neural responses that accurately capture the statistics of S1 neural responses in primates (Bensmaia, Denchev et al. 2008). These results suggest that efficient coding algorithms such as ICA may yield insights about the filter properties of cortical neurons that go beyond those identified by receptive field measurements (Bensmaia, Denchev et al. 2008).

Although the present analysis of tactile scenes has focused on the scale relevant to human touch, the methods used are not restricted to that scale or to a specific strategy for sampling the environment. Our approach can be extended to patches of different sizes explored with different degrees of spatial resolution. As such, the data presented in this study is best considered as a small subset of the data that an organism might be exposed to over a lifetime or even over generations. Another important extension to the framework developed here is to incorporate the temporal

component that is crucial to tactile systems. Movement allows animals to gather information over time, as tactile sensors are moved over a surface. Here we have limited our analysis to a static component that describes the aggregated tactile information obtained over such a sweep by concentrating on the intrinsic properties of object patches.

This work examined the statistics of three metrics: distance, slope, and curvature, as intrinsic properties of external objects; patches were randomly sampled from each object's surface. However, animals and humans sample the world with a goal in mind (such as identifying an object) and combine past and current sensory information both to predict future sensory input as well as increase search efficiency. Therefore, we expect that subjects would sample a set of patches that differs from the randomly sampled ones used here. This hypothesis could be tested by asking human subjects to identify objects based only on tactile input in a situation where the object is behind a screen and thus visually inaccessible. To approximate the conditions of the work presented here, the subject would be allowed to use only one finger to touch the surface of the objects. An efficient exploration could be enforced by limiting the time available for object identification. The objects would be the same ones used in the presented study; here we have characterized the statistics $P(W)$ of these objects as representative of the world W. In the experiment with human subjects, the places on the object's surface explored by the subject as they try to identify the object would be tracked. This data would allow for a characterization of the statistics of the world when sampled by volitional exploration E. This $P(W|E)$ could then be compared to the $P(W)$ analyzed here.

**4.5 Methods**

**4.5.1 Data acquisition**

We used a *EinScan Pro 2X* scanner to capture 3D point cloud representations of the surface of both natural objects and human-made objects. The scanner was mounted on a *Shining 3D* desktop tripod while the objects were placed on the *Shining 3D* turntable. The *EXScan Pro* software was used to capture the scans in "Fixed Scan" mode as "Non-Texture Scans" (without color information). For each scan, the turntable performed 30-50 steps for one rotation and one rotation per scan. Typically, each object was scanned in 2-3 different orientations and the scans were then combined into a single point cloud. One of the objects was very small in size and was therefore scanned using "Handheld Rapid Scan" mode with highest resolution.

**4.5.2 Data cleaning**

Each point cloud was imported to *Geomagic Design X* software for cleaning and meshing. First, the standard meshing algorithm of *Geomagic Design X* (*Mesh Buildup Wizard™*) was used to triangulate the point cloud. Outlier data (non-manifold triangles, small clusters, and isolated triangles) were removed manually or using the *Healing Wizard* software. Holes in the scan were filled using the *Fill Holes* tool. For larger holes or for holes at the boundary, the *Add Bridge* tool was used to segment the holes to ensure better reconstruction with the subsequent use of the *Fill Holes* tool. After all holes were filled and unusable parts of the mesh had been removed, the scan was remeshed targeting an average edge length of 0.1mm. After remeshing, the mesh was enhanced (smoothed and sharpened) with medium settings and optimized to improve curvature flow at medium settings with a maximum of 10 iterations. Finally, the centroid of the mesh was redefined to be the origin and exported in *Binary STL* format, which stores each triangle as a collection of three edge points and the corresponding face normal. The resulting dataset consisted

of 137 scans, of which 96 represented natural scenes and 41 represented human made objects (SI Dataset).

### 4.5.3 Sampling and computation of shape metrics

The method used to compute the distance ($D$), slope ($S$), and curvature ($C$) metrics is illustrated in Figure 4-6. First, we randomly sampled 100-150 circular surface patches of radius $R$ from each object (Figure 4-6a). The point cloud for each sampled surfaced patch was analyzed using Principal Component Analysis (PCA). The plane spanned by the two leading PCs was found, and the points in the surface cloud were projected onto this reference plane (Figure 4-6b). The location of the projected points within the plane was digitized to a 24x24 grid (Figure 4-6c). The position of the grid cell in the $i^{\text{th}}$ row and $j^{\text{th}}$ column is denoted as $p_{i,j}$; the width of the grid cells is $\delta = R/12$.

The plane was then translated in the direction of its outward normal vector, away from the surface of the object just until all surface sampled points were below it. For each point $(i, j)$ on the surface cloud, the distance $D_{i,j}$ to the reference plane was computed as the orthogonal distance from that point to its projection (Figure 4-6d). The distances $D$ were then interpolated over the entire grid, smoothed, and cropped to a circular patch of radius $R$ to obtain a map $\boldsymbol{P}(D)$ over 448 grid points. Patches that filled less than 75% of the circular area before interpolation were rejected.

The metrics $S$ and $C$ were computed from the interpolated and smoothed square grid before cropping it to a circular patch. The slope $S$ was calculated as the forward difference in $D$ between neighboring points in the grid (Eq. 1), resulting in a circular map of 421 slope values $\boldsymbol{P}(S)$. Similarly, $C$ was calculated as the second-order central difference in $D$ (Eq. 2), resulting in a circular map of 384 curvature values $\boldsymbol{P}(C)$. The resulting maps for one example patch are shown in Figure 4-6e.

Since the square grid size is fixed at 24x24 before cropping it to a circular patch, the spatial resolution of the resulting circular maps is determined by the patch radius $R$. Each circular patch can be viewed as a sensory surface with a fixed number of receptors represented by the grid. A larger $R$ leads to a grid that covers a larger area sampled at a lower spatial resolution. Based on the average contact area of a finger pad (~120 mm$^2$ at 1N normal load (van Kuilenburg, Masen et al. 2013)), we chose $R$ to be 6 mm (corresponding to 113 mm$^2$ of circular contact area) for the results
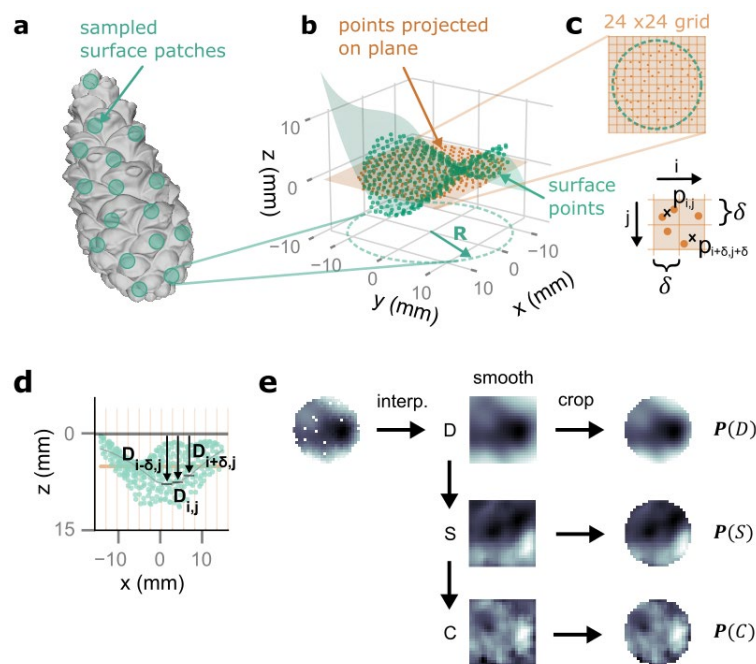


**Figure 4-6. Processing of 3D data. (a)** Approximately 100-150 circular surface patches of radius $R$ were randomly sampled from each object scan. **(b)** For each surface patch, the average plane of the point cloud (orange) was found by using Principal Component Analysis (PCA). **(c)** The points in the cloud were then projected onto the plane, and their location within the plane digitized to a 24x24 grid. The position of the grid cell in the $j^{th}$ row and $i^{th}$ column was indicated as $p_{i,j}$. The cells are of linear size $\delta = R/12$. **(d)** For each cell $(i,j)$ the distance $D_{i,j}$ to the reference plane describes the local shape of the patch. **(e)** The distances $D$ were interpolated to the entire grid, smoothed, and cropped to a circular patch. The metrics slope $S$ and curvature $C$ were computed from the interpolated and smoothed grid before cropping it to a circular patch.

presented here. The choice of a grid size of 24x24 is based on the average edge length of the 3D

meshes of the data (~0.1 mm) rather than on biologically plausible receptor density. With an $R$ of

6 mm, the datasets for natural and human-made objects consisted of a total of 12,309 and 5,788

patches, respectively.

Because the slope of a surface depends on the direction along which it is taken, its value for a

given grid cell was computed by averaging the slope in the x direction ($S_{i,j}^x$) and the slope in the y

direction ($S_{i,j}^y$). The equations for $S_{i,j}^x$ and $S_{i,j}^y$ are:

$$S_{i,j}^x = \frac{D_{i+\delta,j} - D_{i,j}}{\delta}$$

$$S_{i,j}^y = \frac{D_{i,j+\delta} - D_{i,j}}{\delta} \qquad \text{(Eq. 1)}$$

The curvature of a surface is also direction dependent and was again computed as the average of

the curvature in the x direction ($C_{i,j}^x$) and the curvature in the y direction ($C_{i,j}^y$). The equations for

$C_{i,j}^x$ and $C_{i,j}^y$ are:

$$C_{i,j}^x = \frac{D_{i+\delta,j} - 2D_{i,j} + D_{i-\delta,j}}{\delta^2}$$

$$C_{i,j}^y = \frac{D_{i,j+\delta} - 2D_{i,j} + D_{i,j-\delta}}{\delta^2} \qquad \text{(Eq. 2)}$$

### 4.5.4 Neural model

The orientation selectivity $os$ is computed as:

$$os = \frac{\sqrt{[\sum_i R(\theta_i) \sin(2\theta_i)]^2 + [\sum_i R(\theta_i) \cos(2\theta_i)]^2}}{\sum_i R(\theta_i)} \qquad \text{(Eq. 3)}$$

where $R(\theta_i)$ represents the response of the artificial neuron to a bar stimulus with orientation $\theta_i$. Stimulus orientation ranged from 0 to 180 degrees in intervals of 11.25 degrees, for $i = [1, 2, \ldots 16]$. The orientation selectivity of a neuron ranges from 0 to 1, where 0 indicates a uniform response to all orientations and 1 indicates that the neuron responds only to a single stimulus orientation. For more details about this measure of orientation selectivity see (Bensmaia, Denchev et al. 2008).

# CHAPTER 5

# Discussion

This dissertation examined the sensorimotor loop at various levels. In the second chapter, a theoretical framework was developed to study the different strategies used by active sensing systems – alloactive and homeoactive sensing. Within this framework, we found that touch is unique among the different modalities as it strongly links alloactive and homeoactive sensing. In the third chapter, a simulation tool was developed for the most commonly used model system of active touch, the rat vibrissal system. The software models the mechanosensory signals of the full whisker array in response to contact with three dimensional objects. Furthermore, while simulating the incoming sensory signals at the whisker base, the software is able to actuate each whisker and thus to simulate active whisking while allowing for modeling natural environments using 3D scans. In the fourth chapter, we used 3D scans to collect data of natural objects and analyzed their geometrical statistics in terms of distance, slope, and curvature. Using independent component analysis, we showed that curvature is the most informative of the three metrics and produces filters that may represent properties of neurons in the primary somatosensory cortex.

In the following sections, the results described in each of these chapters will be discussed.

## 5.1 Study active sensing strategies using genetic algorithms and continuous-time recurrent neural networks

In chapter 2, we proposed a theoretical framework for active sensing that appreciates the differences in energy flow during two different sensing strategies – alloactive and homeoactive sensing. While alloactive sensing uses mechanical energy to change the configuration (parameters)

of the sensor without changing the state of the environment, homeoactive sensing adds energy to the environment without necessarily changing the sensor configuration.

An important point that has not been specifically addressed in chapter 2 is the dependence of alloactive sensing on mechanical energy. Since actuators of the body are powered by muscle activation, animals can manipulate their sensor configurations only through mechanical energy. This limits the extent to which an animal can change the properties of the sensor. For example, an animal can activate muscles to move its eyes or change the pupil size to manipulate the visual field and focal length of its visual system, but the animal cannot change the filter properties of the retina and thus its sensitivity to a specific spectral range. This limits to how much the animal can increase signal-to-noise ratio through sensor manipulation. For example, an animal might be able to orient towards a signal source to eliminate noise distant from the source. But if the noise source is close to the signal source, changing the sensor configuration is insufficient and additional neural processing is required to isolate the signal from the noise.

During homeoactive sensing, however, the animal generates the signal itself and thereby can select regimes that offer a better signal-to-noise ratio (Caputi 2004, Surlykke, Ghose et al. 2009, Brinkløv, Kalko et al. 2010). This makes the animal much more adaptive to immediate changes in the environment and offers a clear advantage over alloactive sensing strategies. It would therefore not be surprising if homeoactive sensing strategies evolved in environments that provide a low signal-to-noise ratio for alloactive sensing (e.g., murky water, darkness, clutter).

Based on the above, I hypothesize that alloactive sensing strategies may evolve more easily under high signal-to-noise ratio conditions because they do not require the generation of a signal, but when the signal-to-noise ratio decreases homeoactive sensing strategies become more and more

favorable. With the framework proposed in chapter 2, we can now test this hypothesis in computational experiments.

One possible approach to conduct such computational experiments is inspired by Randall D. Beer's work (Beer and Gallagher 1992) and uses a genetic algorithm to evolve simple agents that are equipped with the most basic functions necessary to model alloactive and homeoactive sensing strategies. To model the agents, Beer uses continuous-time recurrent neural networks (CTRNNs), which are among the simplest neural models that have nonlinear and continuous properties (Beer 1995, Beer 2006, Ward and Ward 2009). CTRNNs are able to mimic most neural behaviors and are known to be universal function approximators for smooth dynamics, which makes them ideal to model general neural mechanisms (Beer 2006). To find network parameters that allow the network to exhibit certain behaviors, one can use a genetic algorithm that explores the parameter space through selection by the network's fitness to perform a specific task (Beer and Gallagher 1992). This approach is ideal to examine the dynamics emerging from the interaction between an animal represented by the agent and the environment modeled by the task.

### 5.1.1 Possible experiments to investigate alloactive and homeoactive sensing

A possible task to evolve agents with alloactive and homeoactive sensing strategies is illustrated in Figure 5-1A. The agent is at a fixed location but has two actuators that allow it to rotate within a two-dimensional plane. The agent also has two sensors that can detect a signal; the agent has the ability to manipulate the sensitivity of the sensors by changing the mean frequency $f_{in}$ of a Gaussian filter with shape $N(f_{in}, \sigma)$ and $\sigma = 1$. Changing $f_{in}$ represents alloactive sensing, as it changes the properties of the sensor. To allow the agent to use homeoactive sensing strategies, it is equipped with the ability to emit a signal of the frequency $f_{out}$. The network controlling the agent is shown in Figure 5-1B. It has two sensory neurons S1 and S2 that have connections to four

interneurons N1, N2, N3, and N4. The interneurons have recurrent connections between each other. They all connect to six motor neurons: M1 and M2 control the angular velocity of the agent, M3 and M4 control the change in filter frequency $f_{in}$, and M5 and M6 control the change of the emitted signal frequency $f_{out}$. The equations used to calculate the orientation angle of the agent $\varphi$, and the frequencies $f_{in}$, and $f_{out}$ are given in Figure 5-1B. The network is fully connected and leverages the symmetry of the task. This means that there are 6 groups of neurons – the sensory neurons (S1 and S2), two groups of interneurons (N1 and N2, N3 and N4), and three groups of motor neurons (M1 and M2, M3 and M4, M5 and M6). In each group the bias, time constant, and weights are shared, which results in a total of 84 free parameters (6 parameters for bias, 6 parameters for time constant, and 72 parameters for the weights). Each neuron is connected to all other neurons and has a recurrent connection to itself (not shown).

The task for the agent is to orient towards a target that is located on a semicircle with the center at the agent's location. A noise source is located on the same semicircle. The target emits a signal of frequency $f_t$ and the noise source emits a signal of frequency $f_n$. The fitness of the agent is measured by the difference between the agent's orientation angle and the angle of the target after 30 seconds. Thus, the objective of the agent is to minimize the angle between itself and the target within the given time period. To eliminate the distracting noise, the agent can either adjust the filter frequency $f_{in}$ to the frequency of the target $f_t$, or adjust the filter frequency $f_{in}$ to the freely chosen signal frequency $f_{out}$. The expectation is that it is easier to only change the filter frequency $f_{in}$ as long as the noise frequency $f_n$ does not obscure the target frequency $f_t$. This would represent a high signal-to-noise scenario. However, when the noise frequency is too close to the target frequency such that it cannot be attenuated by changing the filter frequency $f_{in}$ (i.e., low signal-

to-noise scenario), matching the filter and signal frequency in a noise-free range would be more beneficial.
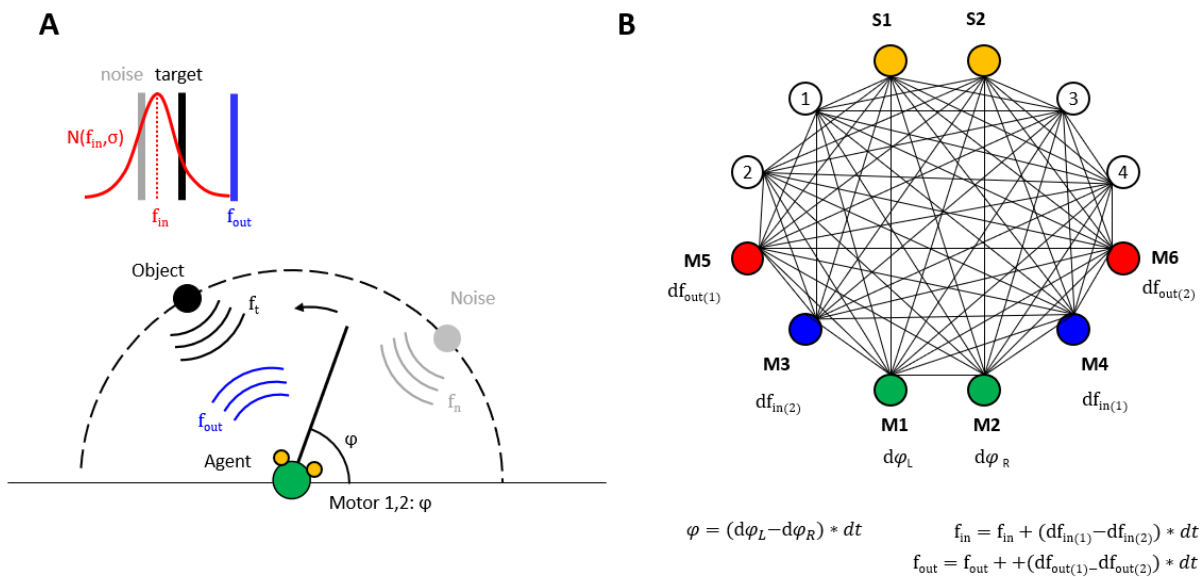


**Figure 5-1. Experimental setup and agent design to test alloactive and homeoactive sensing in noisy environments.** (A) Experimental setup to evolve agents in noisy environments. The agent is at a fixed location but has two actuators that allow it to rotate within a two-dimensional plane. The agent also has two sensors that can detect a signal; the agent also has the ability to manipulate the sensitivity of the sensors by changing the mean frequency $f_{in}$ of a Gaussian filter with t shape $N(f_{in}, \sigma)$ with $\sigma = 1$. The agent is also equipped with the ability to emit a signal of frequency $f_{out}$. The task for the agent is to orient towards a target that is located on a semicircle with the center at the agent's location. The target emits a signal of frequency $f_t$. The noise source is located on the same semicircle as the target and emits a signal of frequency $f_n$. While here only one is shown, three noise sources were used in the experiments. (B) The network controlling the agent has two sensory neurons S1 and S2 that have connections to four interneurons N1, N2, N3, and N4. The interneurons have recurrent connections between each other. They all connect to four motor neurons: M1 and M2 control the angular velocity of the agent, M3 and M4 control the change in filter frequency $f_{in}$, and M5 and M6 control the change of the emitted signal frequency $f_{out}$. The network is fully connected while leveraging the symmetry (i.e. N1 and N2, N3 and N4, M1 and M2, M3 and M4, M5 and M6 share their weights) of the task which results in a total of 84 free parameters. Each neuron also has a recurrent connection to itself (not shown).

The parameters of the network architecture shown in Figure 5-1B were evolved with the genetic algorithm proposed in (Beer and Gallagher 1992) using an initial population of 500 randomly initialized networks. The mutation variance was set to 0.1, whereas the fraction of the best individuals copied to the next generation was set to 10%. In each generation, the selected individuals would increase the population by 10%. The full list of parameter values used in this numerical experiment is shown in Table 5-1 and the documentation of the algorithm used can be found at https://rdbeer.pages.iu.edu/Software/EvolutionaryAgents/SearchDoc.pdf.

**Table 5-1. Parameter configuration for the genetic algorithm to evolve the CTRNNs.**

| Parameter | Value |
|---|---|
| Selection Mode | FITNESS_PROPORTIONATE |
| Reproduction Mode | GENETIC_ALGORITHM |
| Population Size | 1000 |
| Maximum Generations | 2000 |
| Mutation Variance | 0.1 |
| Crossover Mode | TWO_POINT |
| Crossover Probability | 0.5 |
| Maximum Expected Offspring | 1.1 |
| Elitist Fraction | 0.1 |
| Re-evaluation | 1 |

**5.1.2 High SNR environments facilitate evolution of alloactive sensing strategies**

In the first experiment, a high SNR scenario was modeled using three noise sources with frequencies $f_n = [0, 6, 20]$. The angle of the noise sources $\varphi_{n,i}$ on the semicircle were chosen randomly from seven angles $\varphi_{n,i} = \frac{k\pi}{8}$, where $k = 1, 2, \ldots 7$. The target frequency $f_t$ was set to 10.

Using random initialization, 30 agents were evolved using the same parameters. Six agents evolved successfully to a fitness above 0.93; of these, five agents evolved alloactive behavior and one agent evolved homeoactive behavior. The dynamics of the best alloactive agent achieving a fitness of

0.94 is shown in Figure 5-2A. The trajectory in the top panel shows how the agent minimizes the

angle difference between itself and the target. The middle and bottom panel show that the agent

matches the filter frequency $f_{in}$ with the target frequency $f_t$ to avoid the noise signal. The input to

the sensory neurons (S1, S2), the state of interneurons (N1, N2, N3, and N4), and the output of the

motor neurons (M1, M2, M3, M4, M5 and M6) as a function of time are shown in Figure 5-2B.
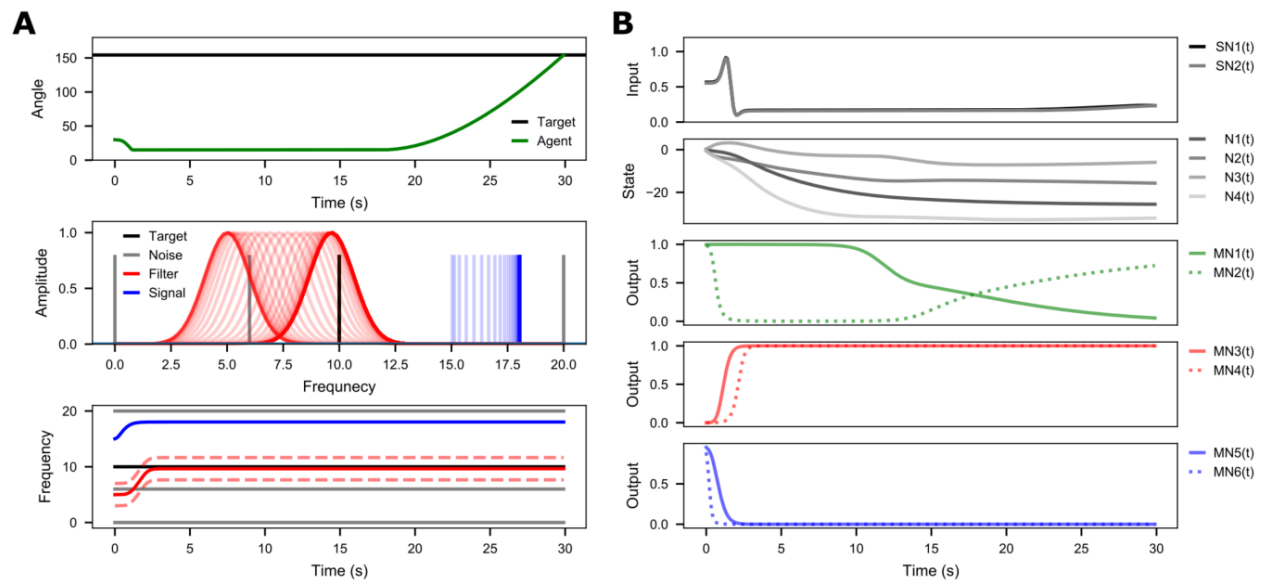


**Figure 5-2. Dynamics of the best alloactive agent evolved under high SNR conditions.** (A)
*Top panel*: Trajectories of the angular position for the agent (green) and the target (black).
*Middle/Bottom panel*: The agent's filter (red) and signal frequency (blue) in the frequency and the
time domain. The frequencies of the target and the three noise sources are shown in black and
grey, respectively. The red dotted line shows two standard deviations from the mean for the
Gaussian filter shape. (B) Dynamics of each neuron. *Top panel*: Input signal to the sensory
neurons. *Second panel*: State of the interneurons. *Bottom panels*: Output of the motor neurons.

The agent that evolved homeoactive behavior achieved the highest fitness of 0.94. The results of

the best trial are shown in Figure 5-3. Instead of moving the filter's frequency to match that of the

target signal, the agent moves both the filter frequency $f_{in}$ and the signal frequency $f_{out}$ out of the

noisy range. Interestingly, the network only overlaps the emitted signal with the filter in the first

half of the trial, and then orients towards the target in the second half of the trial. This indicates

that the network is able to store information from the sensory neurons to produce a motor response later on.
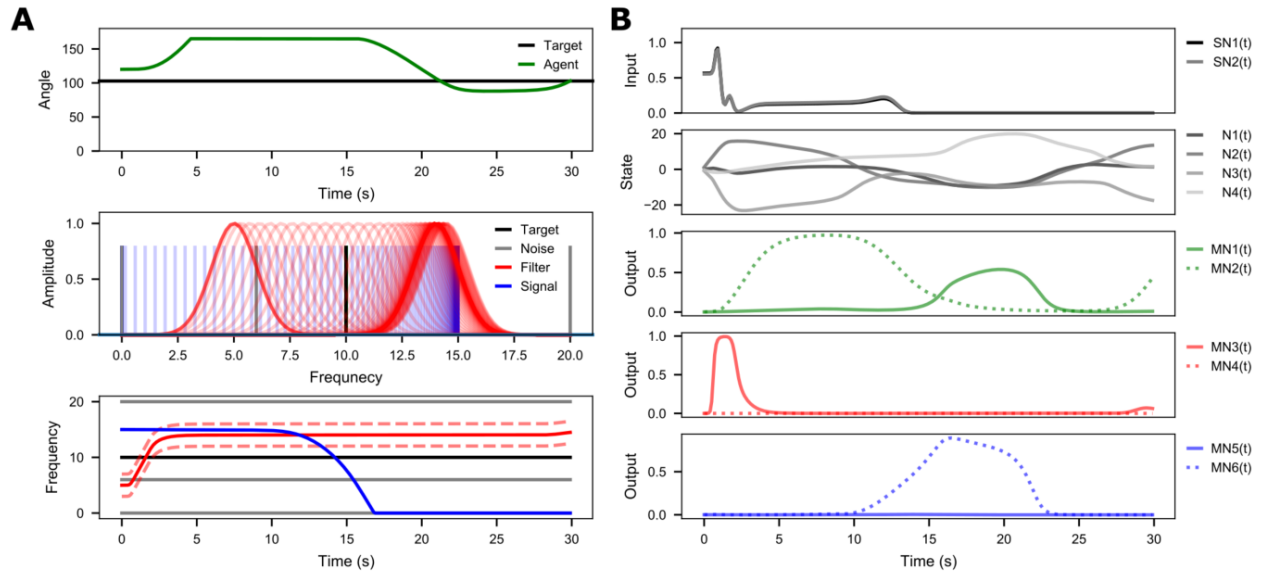


**Figure 5-3. Dynamics of the homeoactive agent evolved under high SNR conditions.** (A) *Top panel*: Trajectories of the angular position for the agent (green) and the target (black). *Middle/Bottom panel*: The agent's filter (red) and signal frequency (blue) in the frequency and the time domain. The frequencies of the target and the three noise sources are shown in black and grey, respectively. The red dotted line shows two standard deviations from the mean for the Gaussian filter shape. (B) Dynamics of each neuron. *Top panel*: Input signal to the sensory neurons. *Second panel*: State of the interneurons. *Bottom panels*: Output of the motor neurons.

### 5.1.3 Low SNR environments facilitate evolution of homeoactive sensing strategies

In the second experiment, a low SNR scenario was modeled using five noise sources with frequencies $f_n = [0, 6, 9, 16, 20]$. Again, the angle of the noise sources $\varphi_{n,i}$ on the semicircle were chosen randomly from seven angles $\varphi_{n,i} = \frac{k\pi}{8}$, where $k = 1, 2, \ldots 7$. The target frequency $f_t$ was the same as in the first experiment and set to 10.

As the evolution of agents turned out to be more challenging in low SNR environments, a hundred agents were evolved using randomized initialization. Only two agents evolved successfully to a fitness value above 0.93. Both agents use homeoactive sensing but use different strategies. One

agent is actively aligning the signal frequency $f_{out}$ with the filter frequency $f_{in}$. The other agent, however, keeps $f_{out}$ stationary while sweeping through the full frequency range with $f_{in}$ to the maximum frequency. The limited time window in which $f_{out}$ and $f_{in}$ overlap seem to be sufficient such that the network can compute the motor response to orient towards the target. The dynamics for this agent are shown in Figure 5-4.
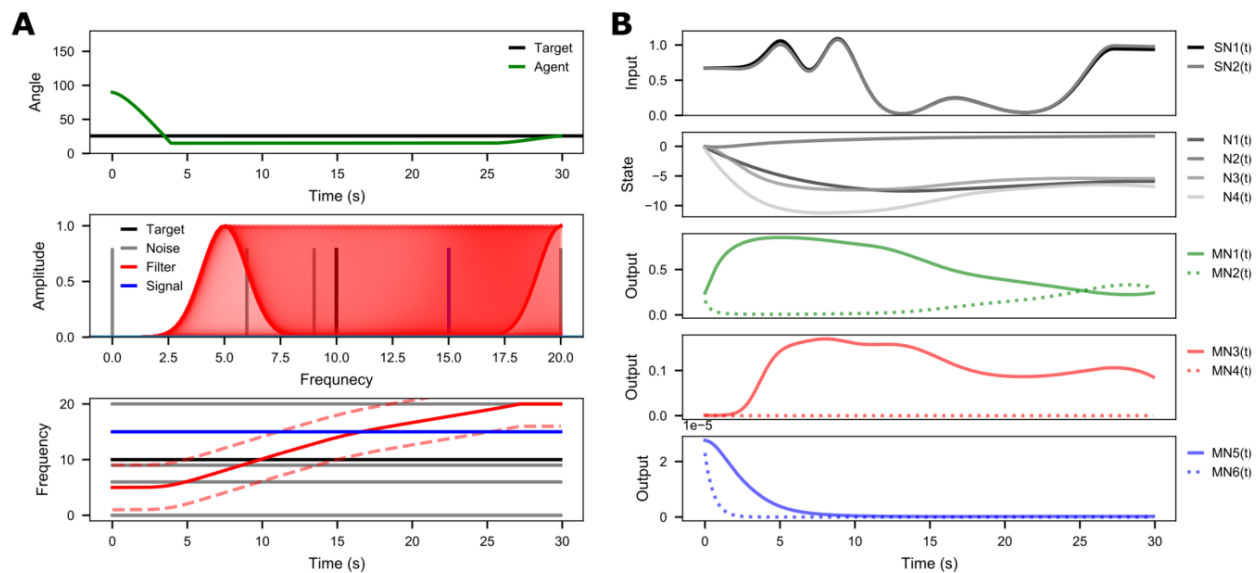


**Figure 5-4. Dynamics of the best homeoactive agent evolved under low SNR conditions.** (A) *Top panel*: Trajectories of the angular position for the agent (green) and the target (black). *Middle/Bottom panel*: The agent's filter (red) and signal frequency (blue) in the frequency and the time domain. The frequencies of the target and the three noise sources are shown in black and grey, respectively. The red dotted line shows two standard deviations from the mean for the Gaussian filter shape. (B) Dynamics of each neuron. *Top panel*: Input signal to the sensory neurons. *Second panel*: State of the interneurons. *Bottom panels*: Output of the motor neurons.

### 5.1.4 Conclusions and future work

The experiments described above are more of a proof of concept rather than an actual study. The experiments showed that the genetic algorithm proposed by (Beer and Gallagher 1992) and continuous-time recurrent neural networks could be used to investigate the theoretical framework presented in chapter 2. However, many factors in those experiments need to be examined further

– network architecture, different noise environments, convergence of the genetic algorithm, and the strategies the agents use to solve the task.

In addition to improving the experiments described in this section, it would be interesting to analyze the predictive power of the neural networks that successfully solve the task and reveal potential analogies to efference copy in the brain. If not found in this implementation, it might be interesting to identify neural network architectures that have predictive capabilities and explore whether these differ for alloactive sensing and homeoactive sensing.

Obviously, the experimental design and the agents used here are vastly simplified and do not capture the complexity of natural behavior and environments. But, if successful, such experiments could reveal potential principles that the brain might use to solve this type of problem, and the computational experiments may offer a tool that could be used to test how constraints affect these principles.

## 5.2 From the mechanics to neurons

In chapter 3, we developed a dynamical model of the rat vibrissal system that can simulate the mechanical signals at the whisker base of each whisker in response to contact with objects in the environment. The model not only simulates the sensory input but also allows for control of sensor movements, thereby enabling researchers to close the sensorimotor loop for an active sensing system. To close the loop, the model of the vibrissal system can be extended with a neural model that generates the neural signals from the mechanical responses elicited by the deflection of the whiskers.

Such a neural model may include a mechanoreceptor model to convert the mechanical signals into a neural signal followed by a neural model to generate individual spikes or a spike rate. A possible

approach was proposed by Mitchinson, Gurney et al. 2004, who use an integrate-and-fire model (Mitchinson, Gurney et al. 2004). Another possibility is to use a generalized linear model as in (Bush, Schroeder et al. 2016, Bush, Solla et al. 2021). While the latter has only been tested in a quasi-static scenario, some preliminary work using a variation of the Mitchinson model showed promising results. Alec Lei, a Neurobiology Master student I supervised and mentored for his Master Thesis, adapted the model proposed by Mitchinson (Mitchinson, Gurney et al. 2004) and fitted it to the mechanical signals generated by the *WHISKiT Physics* Simulator (Zweifel, Bush et al. 2021) based on data collected in (Bush, Solla et al. 2021). The dataset used in this study included extracellular recordings from 90 trigeminal ganglion neurons from 22 female rats. During the recording, the whiskers were deflected manually with a probe in eight cardinal directions with different distances along the whiskers and different magnitudes. Using high-speed cameras, the whiskers were tracked during each trial. The recorded trajectories, specifically the three-dimensional velocities, were then used to compute the three-dimensional mechanical moments $(M_x, M_y, M_z)$ and forces $(F_x, F_y, F_z)$ at the whisker base with *WHISKiT Physics* (Zweifel, Bush et al. 2021).

For the leaky integrate-and-fire (LIF) model adapted from Mitchinson, Gurney et al. 2004 (Mitchinson, Gurney et al. 2004), $M_y$ and $M_z$ and their derivatives were used as the model input. The model allowed for four free parameters to represent the four most prominent properties of Vg neuron: (1) magnitude threshold, to control the sensitivity of the neuron to bending magnitude of the whisker; (2) adaptation, to control the ratio between bending moment and its derivatives; (3) response nonlinearity $\gamma$, to control squashing or amplification behavior of the nonlinearity $x^\gamma$; (4) angular preference, to control the sensitive of the neuron to a specific angular direction. Details of the model can be found in APPENDIX A.

The results of Alec's study show reasonably good fit of the firing rate generated by the neural model to that of real neurons. The advantage of the LIF model is that the fitted parameters have physiological meaning and can be investigated accordingly. For example, the distribution of the neural adaptation parameter shows that there are clearly two populations of neurons: one that primarily responds to the bending moment and one that primarily responds to its derivative. This divides the fitted neurons into groups of slowly adapting and rapidly adapting neurons, consistent with previous research (Zucker and Welker 1969, Gibson and Welker 1983, Gibson and Welker 1983). In contrast, the distribution of the direction preference of the neurons is nearly uniform, suggesting that across the population the neurons do not prefer a specific direction but rather span the entire space. This is consistent with experimental results described in (Bush, Solla et al. 2021) and with the fact that mechanoreceptors are distributed uniformly around the whisker follicle (Hemelt, Kwegyir-Afful et al. 2010).

A K-means cluster algorithm applied to the full parameter space revealed three distinct groups of neurons. Because the distribution of angular preference is uniform, these three groups can be attributed to the properties of threshold magnitude, adaptation, and response nonlinearity. Prototype neurons constructed from these groups suggest that there are three types of neurons: rapidly adapting neurons, slowly adapting neurons with high threshold, and slowly adapting neurons with low threshold. No such clustering was found for the same dataset when quasi-static mechanics and a generalized linear model for the neural response was used (Bush, Solla et al. 2021). While this may seem contradictory, one should keep in mind the differences in the two studies.

First, the LIF model used in this preliminary study only considers the bending moment and its derivatives as input variables. The generalized linear model on the other hand, considered not only

all mechanical variables and their derivatives but also the rotation angle (Bush, Solla et al. 2021). Limiting the input variables to only the bending moment and its derivative may omit important information that trigeminal ganglion neurons may respond to. Further simulation experiments and analysis is needed to determine whether the two models yield different results.

Second, the clusters identified in Figure A 3 are based on the parameter choice of the LIF model. The LIF model used in this study was simple, using only four free parameters. Using more parameters that possibly result in a better fit to the neural data may change how and how many such clusters can be identified. One should also consider that K-means requires to define the number of clusters manually, and assigns datapoints to each cluster based on this number and the centroids found for each cluster. While techniques are available to find the number of clusters that separates the datapoints best, the algorithm ultimately finds the boundaries for the chosen number of clusters. In Figure A 3, one can see that several data points are very close to the boundary and the separation between the clusters may be rather gradual than distinct. Different parametrizations of the LIF model should be explored to gain more insights about the properties of the artificial neurons.

Third, while the parameters of the LIF represent meaningful properties of the artificial neurons, it would be interesting to characterize the simulated spikes using metrics that allow for a fair comparison between the two studies. For example, adaption as defined by the LIF parameter may not be quite the same as the adaptation index that was measured in (Bush, Solla et al. 2021).

Lastly, because the *WHISKiT Physics* simulator requires very smooth input data for successful simulation of the dynamics, discontinuities in the tracking data of the probe used to deflect the whisker in the original experiment (Bush, Solla et al. 2021) required the omission of some of the

data from the set used to fit the LIF model. Further analysis is necessary to determine how omitting these data may have affected the final fit of the LIF model and the fitted parameter values.

Despite its limitations, Alec's work is an important first step to extend *WHISKiT Physics* with a neural model, and brings us one step closer to closing the sensorimotor loop for the rat vibrissal system in simulation.

### 5.3 Quantifying the natural tactile scene and beyond

In chapter 4, we quantified the natural tactile scene in terms of distance, slope, and curvature at the scale of a human fingertip by analyzing close to a hundred natural objects. Applying independent component analysis (ICA) on the least processed dataset (distance) revealed that basis vectors associated with $2^{nd}$-order filters are more informative than those associated with $1^{st}$ or $3^{rd}$-order filters. We then showed that directly using curvature information yields basis vectors that are similar to Gabor filters, as have been found in the primary somatosensory cortex (S1). Using these filters in a simple neural model confirmed those similarities in terms of orientation selectivity of cortical neurons in S1.

In our analysis we used ICA, a comparatively old technique in the field. The FastICA algorithm we used in the study finds linear combinations of basis vectors that best reconstruct the input under the constraint of minimizing mutual information (maximizing negentropy) between the components (Hyvärinen and Oja 2000). This is equivalent to reducing redundancy or decorrelating the input signal, consistent with the "efficient coding" or "predictive coding" theory (Huang and Rao 2011, Chalk, Marre et al. 2018). Because ICA finds linear combinations of basis vectors to reconstruct the input, it can be viewed as a generative model under the assumption that the input signal is stationary. While this is still a "predictive coding" scheme, in reality input statistics are

not stationary, as pointed out by several (Huang and Rao 2011, Chalk, Marre et al. 2018, Mlynarski and Hermundstad 2021).

It is also unlikely that sensory signals are processed in a linear fashion; therefore ICA cannot give much insight about neural function other than providing some evidence that the neural code may optimally process incoming sensory information. Much more work is needed to dissect how and why the brain may achieve such an efficient neural code, and under which condition and constraints this may be the case (Chalk, Marre et al. 2018). Chalk, Marre et al. 2018 examined efficient coding under the constraint that the codes are predictive about future sensory events, thus considering the temporal component likely relevant to neural processing.

In the present work, we only investigated efficient codes in the context of spatial and stationary sensory input; future work should focus on including the temporal nature of touch – moving the sensor over a surface rather than indenting onto an object. Furthermore, animals sample the environment with a goal in mind, such as discrimination or categorization of objects. Thus, the sampled location of a surface is not random but guided by information acquired in the recent past and information expected in near future. More experiments are thus needed on how humans or animals explore natural objects. The dataset collected in the present study and current 3D printing technology would provide the means to conduct such experiments not only in humans but also in animals under controlled conditions.

While the study described in chapter 4 analyzed the geometrical properties of the 3D world, the next step would be to examine the statistics of the variables that are accessible to the animal. A major drawback of the study in chapter 4 is that it does not consider the mapping that takes place between the physical world and the sensory surface. The simulation tool *WHISKiT Physics*

presented in chapter 3 provides the means to model this mapping for the rat vibrissal system, and to generate mechanical signals in response to contact with 3D objects like those used in chapter 4. One could thus generate a dataset of the natural tactile scene in terms of the mechanical information acquired by the rat vibrissal system. Such a dataset offers the opportunity to explore models of sensory processing and receptive fields at the different stages of the somatosensory pathways in the rat. A first step could simply be applying the methods used in chapter 4 on the mechanical data and compare the results with experimental measurements of receptive fields in the barrel cortex (Simons 1983, Ito 1985, Simons 1985, Armstrong-James and Fox 1987, Moore, Nelson et al. 1999, Fox, Wright et al. 2003, Jacob, Le Cam et al. 2008, Ollerenshaw, Zheng et al. 2014, Fox 2018).

## 5.4 Unifying it all

My thesis laid the groundwork for many exciting avenues this research could take. Combining the work described in the three previous chapters has the potential of answering important research questions about early sensory processing. Chapter 2 outlines a theory about active sensing strategies and offers hypotheses about possible differences in the algorithms the brain may use to predict the sensory consequences of executed motor actions. Chapter 3 describes a tool to simulate an agent that has an active sensing system. The developed software can easily be extended with a model that can test the hypotheses posed in chapter 2. And finally, chapter 4 provides the means to generate a dataset needed to conduct these computational studies as well as to design experiments that can verify the results.

While it was beyond the scope of this dissertation to unify the three chapters in a computational study, I hope that future students may have the opportunity to do so and thus shed light on the early processing stages of tactile information.

# References

Adams, R. A., K. E. Stephan, H. R. Brown, C. D. Frith and K. J. Friston (2013). "The computational anatomy of psychosis." Frontiers in Psychiatry **4**: 47.

Adibi, M. and E. Arabzadeh (2011). "A comparison of neuronal and behavioral detection and discrimination performances in rat whisker system." J Neurophysiol **105**(1): 356-365.

Adineh, V. R., B. Liu, R. Rajan, W. Yan and J. Fu (2015). "Multidimensional characterisation of biomechanical structures by combining Atomic Force Microscopy and Focused Ion Beam: A study of the rat whisker." Acta Biomater **21**: 132-141.

Ahissar, E. and E. Assa (2016). "Perception as a closed-loop convergence process." Elife **5**.

Ahissar, E., R. Sosnik and S. Haidarliu (2000). "Transformation from temporal to rate coding in a somatosensory thalamocortical pathway." Nature **406**(6793): 302-306.

Akbarinia, R. and B. Cloez (2019). "Efficient matrix profile computation using different distance functions." arXiv preprint arXiv:1901.05708.

Arabzadeh, E., R. S. Petersen and M. E. Diamond (2003). "Encoding of whisker vibration by rat barrel cortex neurons: implications for texture discrimination." The Journal of Neuroscience **23**(27): 9146 –9154.

Arbib, M. A. (1989). The metaphorical brain 2: neural networks and beyond. New York, N.Y., Wiley.

Armstrong-James, M. and K. Fox (1987). "Spatiotemporal convergence and divergence in the rat S1 "Barrel" cortex." Journal of Comparative Neurology **263**(2): 265-281.

Ashwell, K. W. (1982). "The adult mouse facial nerve nucleus: morphology and musculotopic organization." Journal of Anatomy **135**(OCT): 531-538.

Atick, J. J. and A. N. Redlich (1992). "What does the retina know about natural scenes?" Neural computation **4**: 196-210.

Attneave, F. (1954). "Some informational aspects of visual perception." Psychological Review **61**(3): 183-193.

Axelrad, H., R. Verley and E. Farkas (1976). "Responses evoked in mouse and rats S1 cortex by vibrissa stimulation." Neuroscience Letters **3**(5-6): 265-274.

Bagdasarian, K., M. Szwed, P. M. Knutsen, D. Deutsch, D. Derdikman, M. Pietr, E. Simony and E. Ahissar (2013). "Pre-neuronal morphological processing of object location by individual whiskers." Nat Neurosci **16**(5): 622-631.

Bajcsy, R. (1988). "Active perception." Proceedings of the IEEE **76**(8): 996-1005.

Bajcsy, R., Y. Aloimonos and J. K. Tsotsos (2017). "Revisiting active perception." Autonomous Robots **42**(2): 177-196.

Ballard, D. H. (1991). "Animate vision." Artificial Intelligence **48**(1): 57-86.

Barlow, H. B. (1961). "Possible principles underlying the transformations of sensory messages." Sensory communication **6**(2): 57-58.

Barnett, P. D., K. Nordstrom and D. C. O'Carroll (2010). "Motion adaptation and the velocity coding of natural scenes." Current Biology **20**(11): 994-999.

Bates, C. A. and H. P. Killackey (1985). "The organization of the neonatal rat's brainstem trigeminal complex and its role in the formation of central trigeminal patterns." Journal of Comparative Neurology **240**(3): 265-287.

Bates, M. E., S. A. Stamper and J. A. Simmons (2008). "Jamming avoidance response of big brown bats in target detection." Journal of Experimental Biology **211**(Pt 1): 106-113.

Beer, R. D. (1995). "A dynamical systems perspective on agent-environment interaction." Artificial Intelligence **72**(1): 173-215.

Beer, R. D. (1995). "On the dynamics of small continuous-time recurrent neural networks." Adaptive Behavior **3**(4): 469-509.

Beer, R. D. (1997). "The dynamics of adaptive behavior: A research program." Robotics and Autonomous Systems **20**: 257-289.

Beer, R. D. (2006). "Parameter space structure of continuous-time recurrent neural networks." Neural Computation **18**(12): 3009-3051.

Beer, R. D. and J. C. Gallagher (1992). "Evolving dynamical neural networks for adaptive behavior." Adaptive Behavior **1**(1): 91-122.

Beleyur, T. and H. R. Goerlitz (2019). "Modeling active sensing reveals echo detection even in large groups of bats." Proceedings of the National Academy of Sciences.

Bell, A. J. and T. J. Sejnowski (1995). "An information-maximization approach to blind separation and blind deconvolution." Neural Computation **7**(6): 1129-1159.

Bell, A. J. and T. J. Sejnowski (1997). "The "independent components" of natural scenes are edge filters." Vision Research **37**(23): 3327-3338.

Bell, C. C. (1982). "Properties of a modifiable efference copy in an electric fish." Journal of Neurophysiology **47**(6): 1043-1056.

Bellavance, M. A. (2017). "Parallel inhibitory and excitatory trigemino-facial feedback circuitry for reflexive vibrissa movement." Neuron **95**: 673-682.

Belli, H. M., C. S. Bresee, M. M. Graff and M. J. Z. Hartmann (2018). "Quantifying the three-dimensional facial morphology of the laboratory rat with a focus on the vibrissae." PLoS One **13**(4): e0194981.

Belli, H. M., A. E. T. Yang, C. S. Bresee and M. J. Z. Hartmann (2017). "Variations in vibrissal geometry across the rat mystacial pad: base diameter, medulla, and taper." Journal of Neurophysiology **117**(4): 1807-1820.

Benda, J., L. Maler and A. Longtin (2010). "Linear versus nonlinear signal transmission in neuron models with adaptation currents or dynamic thresholds." Journal of Neurophysiology **104**(5): 2806-2820.

Bensmaia, S. J., P. V. Denchev, J. F. Dammann, J. C. Craig and S. S. Hsiao (2008). "The representation of stimulus orientation in the early stages of somatosensory processing." The Journal of Neuroscience **28**(3): 776.

Berg, R. W. and D. Kleinfeld (2003). "Rhythmic whisking by rat: Retraction as well as protraction of the vibrissae is under active muscular control." Journal of Neurophysiology **89**(1): 104-117.

Berger, T., A. Borgdorff, S. Crochet, F. B. Neubauer, S. Lefort, B. Fauvet, I. Ferezou, A. Carleton, H.-R. Lüscher and C. C. Petersen (2007). "Combined voltage and calcium epifluorescence imaging in vitro and in vivo reveals subthreshold and suprathreshold dynamics of mouse barrel cortex." Journal of Neurophysiology **97**(5): 3751-3762.

Bergstra, J., B. Komer, C. Eliasmith and D. Warde-Farley (2014). Preliminary evaluation of hyperopt algorithms on HPOLib. ICML workshop on AutoML.

Birdwell, J. A., J. H. Solomon, M. Thajchayapong, M. A. Taylor, M. Cheely, R. B. Towal, J. Conradt and M. J. Hartmann (2007). "Biomechanical models for radial distance determination by the rat vibrissal system." J Neurophysiol **98**(4): 2439-2455.

Birdwell, J. A., J. H. Solomon, M. Thajchayapong, M. A. Taylor, M. Cheely, R. B. Towal, J. Conradt and M. J. Z. Hartmann (2007). "Biomechanical models for radial distance determination by the rat vibrissal system." Journal of Neurophysiology **98**(4): 2439-2455.

Blakemore, S. J., S. J. Goodbody and D. M. Wolpert (1998). "Predicting the consequences of our own actions: The role of sensorimotor context estimation." The Journal of Neuroscience **18**(18): 7511-7518.

Bodegård, A., S. Geyer, C. Grefkes, K. Zilles and P. E. Roland (2001). "Hierarchical processing of tactile shape in the human brain." Neuron **31**(2): 317-328.

Boubenec, Y., D. E. Shulz and G. Debrégeas (2012). "Whisker encoding of mechanical events during active tactile exploration." Frontiers in Behavioral Neuroscience **6**(November): 1-16.

Bowers, J. M., D. Beeman and M. Hucka (2000). The GENESIS Simulation System. Pasadina, CA, California Institute of Technology.

Brady, N. and D. Field (2000). "Local contrast in natural images: normalisation and coding efficiency." Perception **29**(9): 1041-1055.

Brecht, M., B. Preilowski and M. M. Merzenich (1997). "Functional architecture of the mystacial vibrissae." Behav Brain Res **84**(1-2): 81-97.

Brecht, M., B. Preilowski and M. M. Merzenich (1997). "Functional architecture of the mystacial vibrissae." Behavioural Brain Research **84**(1-2): 81-97.

Brecht, M., B. Preilowski and M. M. Merzenich (1997). "Functional architecture of the mystacial vibrissae." Behavioural Brain Research.

Bremen, P., M. M. van Wanrooij and A. J. van Opstal (2010). "Pinna cues determine orienting response modes to synchronous sounds in elevation." The Journal of Neuroscience **30**(1): 194-204.

Brinkløv, S., E. K. V. Kalko and A. Surlykke (2010). "Dynamic adjustment of biosonar intensity to habitat clutter in the bat Macrophyllum macrophyllum (Phyllostomidae)." Behavioral Ecology and Sociobiology **64**(11): 1867-1874.

Brooks, J. X., J. Carriot and K. E. Cullen (2015). "Learning to expect the unexpected: Rapid updating in primate cerebellum during voluntary self-motion." Nature Neuroscience **18**(9): 1310-1317.

Brooks, J. X. and K. E. Cullen (2019). "Predictive sensing: The role of motor signals in sensory processing." Biological Psychiatry: Cognitive Neuroscience and Neuroimaging **4**(9): 842-850.

Brunel, N. and S. Sergi (1998). "Firing frequency of leaky intergrate-and-fire neurons with synaptic current dynamics." Journal of Theoretical Biology **195**(1): 87-95.

Bullock, T. H. (1973). "Seeing the world through a new sense: electroreception in fish." American Scientist **61**(3): 316-325.

Burge, J. and W. S. Geisler (2015). "Optimal speed estimation in natural image movies predicts human performance." Nature Communications **6**: 7900.

Burkitt, A. N. (2006). "A review of the integrate-and-fire neuron model: I. Homogeneous synaptic input." Biol Cybern **95**(1): 1-19.

Bush, N. E., C. L. Schroeder, J. A. Hobbs, A. E. Yang, L. A. Huet, S. A. Solla and M. J. Hartmann (2016). "Decoupling kinematics and mechanics reveals coding properties of trigeminal ganglion neurons in the rat vibrissal system." Elife **5**.

Bush, N. E., S. A. Solla and M. J. Z. Hartmann (2021). "Continuous, multidimensional coding of 3D complex tactile stimuli by primary sensory neurons of the vibrissal system." Proceedings of the National Academy of Sciences **118**(32).

Caputi, A. A. (2004). "Contributions of electric fish to the understanding of sensory processing by reafferent systems." J Physiol Paris **98**(1-3): 81-97.

Caputi, A. A. (2004). "Contributions of electric fish to the understanding sensory processing by reafferent systems." Journal of Physiology-Paris **98**(1): 81-97.

Carl, K., W. Hild, J. Mämpel, C. Schilling, R. Uhlig and H. Witte (2012). "Characterization of statical properties of rat's whisker system." IEEE Sensors Journal **12**(2): 340-349.

Catenacci Volpi, N., J. C. Quinton and G. Pezzulo (2014). "How active perception and attractor dynamics shape perceptual categorization: a computational model." Neural Networks **60**: 1-16.

Cessac, B., P. Kornprobst, S. Kraria, H. Nasser, D. Pamplona, G. Portelli and T. Vieville (2017). "PRANAS: A New Platform for Retinal Analysis and Simulation." Frontiers in Neuroinformatics **11**: 49.

Chalk, M., O. Marre and G. Tkacik (2018). "Toward a unified theory of efficient, predictive, and sparse coding." Proceedings of the National Academy of Sciences **115**(1): 186-191.

Chapman, C. E. (1994). "Active versus passive touch: factors influencing the transmission of somatosensory signals to primary somatosensory cortex." Canadian Journal of Physiology and Pharmacology **72**(5): 558-570.

Chapman, C. E. and E. Beauchamp (2006). "Differential controls over tactile detection in humans by motor commands and peripheral reafference." Journal of Neurophysiology **96**(3): 1664-1675.

Chapman, C. E., M. C. Bushnell, D. Miron, G. H. Duncan and J. P. Lund (1987). "Sensory perception during movement in man." Experimental Brain Research **68**(3): 516-524.

Charlton, B. D., M. A. Owen and R. R. Swaisgood (2019). "Coevolution of vocal signal characteristics and hearing sensitivity in forest mammals." Nature Communications **10**(1): 2778.

Cheeseman, J. R., J. F. Norman and A. M. Kappers (2016). "Dynamic cutaneous information is sufficient for precise curvature discrimination." Scientific Reports **6**: 25473.

Cheung, Y.-m. and L. Xu (2001). "Independent component ordering in ICA time series analysis." Neurocomputing **41**(1): 145-152.

Chiaia, N. L., C. A. Bennett-Clarke and R. W. Rhoades (1991). "Effects of cortical and thalamic lesions upon primary afferent terminations, distributions of projection neurons, and the cytochrome oxidase pattern in the trigeminal brainstem complex." J Comp Neurol **303**(4): 600-616.

Clack, N. G., D. H. O'Connor, D. Huber, L. Petreanu, A. Hires, S. Peron, K. Svoboda and E. W. Myers (2012). "Automated tracking of whiskers in videos of head fixed rodents." PLoS Comput Biol **8**(7): e1002591.

Clark, A. (2013). "Whatever next? Predictive brains, situated agents, and the future of cognitive science." Behavioral and Brain Sciences **36**(03): 181-204.

Clements, T. N. and C. D. Rahn (2006). "Three-dimensional contact imaging with an actuated whisker." IEEE Transactions on Robotics and Automation **22**(4): 844-848.

Concha-Miranda, M., J. Rios, J. Bou, J. L. Valdes and P. E. Maldonado (2019). "Timing Is of the essence: Improvement in perception during active sensing." Frontiers in Behavioral Neuroscience **13**: 96.

Coubard, O. A. (2013). "Saccade and vergence eye movements: a review of motor and premotor commands." European Journal of Neuroscience **38**(10): 3384-3397.

Coumans, E. (2015). Bullet Physics Simulation. ACM SIGGRAPH 2015 Courses. New York, NY, USA, ACM.

Cunningham, J. P., V. Gilja, S. I. Ryu and K. V. Shenoy (2009). "Methods for estimating neural firing rates, and their application to brain–machine interfaces." Neural Networks **22**(9): 1235-1246.

Das, A. and R. Alagirusamy (2011). Improving tactile comfort in fabrics and clothing. Improving Comfort in Clothing, Elsevier**:** 216-244.

De Maesschalck, R., D. Jouan-Rimbaud and D. L. Massart (2000). "The mahalanobis distance." Chemometrics and intelligent laboratory systems **50**(1): 1-18.

Delp, S. L., F. C. Anderson, A. S. Arnold, P. Loan, A. Habib, C. T. John, E. Guendelman and D. G. Thelen (2007). "OpenSim: open-source software to create and analyze dynamic simulations of movement." IEEE Trans Biomed Eng **54**(11): 1940-1950.

Deutsch, D., M. Pietr, P. M. Knutsen, E. Ahissar and E. Schneidman (2012). "Fast feedback in active sensing: touch-induced changes to whisker-object interaction." PLoS ONE **7**(9).

Diamond, M. E. and E. Arabzadeh (2013). "Whisker sensory system - From receptor to decision." Progress in Neurobiology **103**: 28-40.

Diamond, M. E., M. von Heimendahl and E. Arabzadeh (2008). "Whisker-mediated texture discrimination." PLoS Biol **6**(8): e220.

Diamond, M. E., M. von Heimendahl, P. M. Knutsen, D. Kleinfeld and E. Ahissar (2008). "'Where' and 'what' in the whisker sensorimotor system." Nature Reviews Neuroscience **9**(8): 601-612.

DiCarlo, J. J. and K. O. Johnson (2000). "Spatial and tomporal structure of receptive fields in primate somatosensory area 3b: Effects of stimulus scanning direction and orientation." The Journal of Neuroscience 20(1): 495.

Dodds, E. M. and M. R. DeWeese (2019). "On the sparse structure of natural sounds and natural images: Similarities, differences, and implications for neural coding." Frontiers in Computational Neuroscience 13: 39.

Dong, D. W. and J. J. Atick (1995). "Temporal decorrelation: a theory of lagged and nonlagged responses in the lateral geniculate nucleus." Network: Computation in Neural Systems 6(2): 159-178.

Dorfl, J. (1982). "The musculature of mystacial vibrissae of the white mouse." Journal of Anatomy 135(AUG): 147-154.

Douglas, R. H., J. C. Partridge, K. S. Dulai, D. M. Hunt, C. W. Mullineaux and P. H. Hynninen (1999). "Enhanced retinal longwave sensitivity using a chlorophyll-derived photosensitiser in Malacosteus niger, a deep-sea dragon fish with far red bioluminescence." Vision Research 39(17): 2817-2832.

Dubrovskii, N. A. (1976). "Critical interval of active hearing in dolphins." Acoustical Physics 22(4): 351-352.

Durham, D. and T. A. Woolsey (1984). "Effects of neonatal whisker lesions on mouse central trigeminal pathways." Journal of Comparative Neurology 223(3): 424-447.

Dyakova, O. and K. Nordstrom (2017). "Image statistics and their processing in insect vision." Current Opinion in Insect Science 24: 7-14.

Dykes, R. W. (1975). "Afferent fibers from mystacial vibrissae of cats and seals." Journal of Neurophysiology 38(3): 650-662.

Ebara, S., T. Furuta and K. Kumamoto (2017). "Vibrissal mechanoreceptors." Scholarpedia 12(3): 32372.

Engel, A. K., P. Fries and W. Singer (2001). "Dynamic predictions: oscillations and synchrony in top-down processing." Nature Reviews Neuroscience 2(10): 704-716.

Erez, T., Y. Tassa and E. Todorov (2015). Simulation tools for model-based robotics: Comparison of Bullet, Havok, MuJoCo, ODE and PhysX. Proceedings - IEEE International Conference on Robotics and Automation, IEEE. 2015-June: 4397-4404.

Erickson, C. J. (1995). Perspectives on percussive foraging in the aye-aye (Daubentonia Madagascariensis). Creatures of the Dark: The Nocturnal Prosimians. L. Alterman, G. A. Doyle and M. K. Izard. Boston, MA, Springer US: 251-259.

Erwin, C. and J. McCutchan (2008). Bullet Physics Library.

Erzurumlu, R. S. and H. P. Killackey (1980). "Diencephalic projections of the subnucleus interpolaris of the brainstem trigeminal complex in the rat." Neuroscience 5(11): 1891-1901.

Evans, M., C. W. Fox, M. J. Pearson and T. J. Prescott (2009). "Spectral template based classification of robotic whisker sensor signals in a floor texture discrimination task." Proceedings of Towards Autonomous Robotic Systems(August 2017): 19-24.

Evans, M. H. (2013). Efficient coding in the whisker system: biomimetic pre-processing for robots? Biomimetic and Biohybrid Systems: Second International Conference, Living Machines 2013, London, UK, July 29 -- August 2, 2013. Proceedings. N. F. Lepora, A. Mura, H. G. Krapp, P. F. M. J. Verschure and T. J. Prescott. Berlin, Heidelberg, Springer Berlin Heidelberg: 364-367.

Feng, A. S. and P. M. Narins (2008). "Ultrasonic communication in concave-eared torrent frogs (Amolops tormotus)." Journal of Comparative Physiology A: Neuroethology, Sensory, Neural, and Behavioral Physiology 194(2): 159-167.

Ferezou, I., S. Bolea and C. C. Petersen (2006). "Visualizing the cortical representation of whisker touch: voltage-sensitive dye imaging in freely moving mice." Neuron 50(4): 617-629.

Field, D. J. (1987). "Relations between the statistics of natural images and the response properties of cortical cells." Journal of the Optical Society of America 4(12): 2379-2394.

Field, D. J. (1993). "Scale-invariance and self-similar 'wavelet' transforms: an analysis of natural scenes and mammalian visual systems." Wavelets Fractals and Fourier Transforms: 151-193.

Field, D. J. (1994). "What Is the goal of sensory coding?" Neural computation. 6(4): 559-601.

Field, D. J. (1999). "Wavelets, vision and the statistics of natural scenes." Philosophical Transactions: Mathematical, Physical and Engineering Sciences 357(1760): 2527-2542.

Fine, I., D. I. MacLeod and G. M. Boynton (2003). "Surface segmentation based on the luminance and color statistics of natural scenes." Journal of the Optical Society of America. A, Optics, image science, and vision 20(7): 1283-1291.

Fitzgerald, O. (1940). "Discharges from the sensory organs of the cat's vibrissae and the modification in their activity by ions." The Journal of Physiology 98(2): 163-178.

Ford, J. M. and D. H. Mathalon (2012). "Anticipating the future: automatic prediction failures in schizophrenia." International Journal of Psychophysiology 83(2): 232-239.

Ford, J. M., D. H. Mathalon, T. Heinks, S. Kalba, W. O. Faustman and W. T. Roth (2001). "Neurophysiological evidence of corollary discharge dysfunction in schizophrenia." American Journal of Psychiatry 158(12): 2069-2071.

Forgy, E. W. (1965). "Cluster analysis of multivariate data: efficiency versus interpretability of classifications." Biometrics 21: 768-769.

Fox, K. (2018). "Deconstructing the cortical column in the barrel cortex." Neuroscience 368: 17-28.

Fox, K., N. Wright, H. Wallace and S. Glazewski (2003). "The origin of cortical surround receptive fields studied in the barrel cortex." The Journal of Neuroscience 23(23): 8380.

Friedberg, M. H., S. M. Lee and F. F. Ebner (2004). "The contribution of the principal and spinal trigeminal nuclei to the receptive field properties of thalamic VPM neurons in the rat." Journal of Neurocytology 33(1): 75-85.

Friston, K., J. Kilner and L. Harrison (2006). "A free energy principle for the brain." Journal of Physiology(100): 70-87.

Friston, K. J., J. Daunizeau, J. Kilner and S. J. Kiebel (2010). "Action and behavior: A free-energy formulation." Biological Cybernetics.

Ge, M., Y. Jia, J. B. Kirunda, Y. Xu, J. Shen, L. Lu, Y. Liu, Q. Pei, X. Zhan and L. Yang (2018). "Propagation of firing rate by synchronization in a feed-forward multilayer Hindmarsh–Rose neural network." Neurocomputing **320**: 60-68.

Geisler, W. S. (2008). "Visual perception and the statistical properties of natural scenes." Annual Review of Psychology **59**: 167-192.

Geisler, W. S. and J. S. Perry (2009). "Contour statistics in natural images: grouping across occlusions." Visual Neuroscience **26**(1): 109-121.

Geisler, W. S., J. S. Perry, Super B.J. and G. D.P. (2001). "Edge co-occurrence in natural images predicts contour grouping performance." Vision Research **41**: 711–724.

Gewaltig, M. and M. Diesmann (2007). "NEST (NEural Simulation Tool)." Scholarpedia **2**: 1430.

Gibson, J. J. (1950). "The perception of the visual world." Psychological Bulletin **48**(4): 1-259.

Gibson, J. J. (1962). "Observations on active touch." Psychological Review **69**(6): 477-491.

Gibson, J. J. (1966). The senses considered as perceptual systems. Boston, Houghton Mifflin.

Gibson, J. J. (1976). "The myth of passive perception: A reply to Richards." Philosophy and Phenomenological Research **37**: 234-238.

Gibson, J. M. and W. I. Welker (1983). "Quantitative studies of sitmulus coding in 1st-order vibrissa afferents of rats 1: Receptive field properties and threshold distributions." Somatosensory Research **1**(1): 51-67.

Gibson, J. M. and W. I. Welker (1983). "Quantitative studies of sitmulus coding in 1st-order vibrissa afferents of rats 2: Adaptation and coding of stimluus parameters." Somatosensory Research **1**(2): 95-117.

Gibson, J. M. and W. I. Welker (1983). "Quantitative studies of stimulus coding in first-order vibrissa afferents of rats. 1. Receptive field properties and threshold distributions." Somatosens Res **1**(1): 51-67.

Gibson, J. M. and W. I. Welker (1983). "Quantitative studies of stimulus coding in first-order vibrissa afferents of rats. 2. Adaptation and coding of stimulus parameters." Somatosens Res **1**(2): 95-117.

Girard, B. and A. Berthoz (2005). "From brainstem to cortex: Computational models of saccade generation circuitry." Progress in Neurobiology **77**(4): 215-251.

Goeckel, D., B. A. Bash, A. Sheikholeslami, S. Guha and D. Towsley (2017). Covert active sensing of linear systems. 2017 51st Asilomar Conference on Signals, Systems, and Computers.

Goodwin, A. W., V. G. Macefield and J. W. Bisley (1997). "Encoding of object curvature by tactile afferents from human fingers." Journal of Neurophysiology **78**(6): 2881-2888.

Guicrobles, E., W. M. Jenkins and H. Bravo (1992). "Vibrissal roughness discrimination is barrelcortex-dependent." Behavioural Brain Research **48**(2): 145-152.

Hafner, V., M. Fend and K. P. Kording (2004). "Predicting properties of the rat somatosensory system by sparse coding." Neural Information Processing - Letters and Reviews **4**(1): 11-18.

Hafner, V. V., M. Fend, M. Lungarella, R. Pfeifer, P. König and K. P. Kording (2003). "Optimal coding for naturally occurring whisker deflections." Artificail Neural Networks and Neural Information Processing - Ican/Iconip 2003 **2714**: 805-812.

Hahn, J. F. (1971). "Stimulus-response relationships in first-order sensory fibres from cat vibrissae." The Journal of Physiology **213**(1): 215-226.

Halata, Z., M. Grim and K. I. Baumann (2003). "The Merkel cell: morphology, developmental origin, function." Casopis Lékaru Ceských **142**(1): 4-9.

Hancock, P., R. Baddeley and L. Smith (1992). "The principal components of natural images." Network: Computation In Neural Systems **3**: 61-70.

Hartmann, M. J. (2009). "Active touch, exploratory movements, and sensory prediction." Integrative and Comparative Biology **49**(6): 681-690.

Hartmann, M. J., N. J. Johnson, R. B. Towal and C. Assad (2003). "Mechanical Characteristics of Rat Vibrissae : Resonant Frequencies and Damping in Isolated Whiskers and in the Awake Behaving Animal." **23**(16): 6510-6519.

Hase, K., Y. Kadoya, Y. Maitani, T. Miyamoto, K. I. Kobayasi and S. Hiryu (2018). "Bats enhance their call identities to solve the cocktail party problem." Communications Biology - Nature **1**: 39.

Hausler, C., A. Susemihl and M. P. Nawrot (2013). "Natural image sequences constrain dynamic receptive fields and imply a sparse code." Brain Research **1536**: 53-67.

Hemelt, M. E., E. E. Kwegyir-Afful, R. M. Bruno, D. J. Simons and A. Keller (2010). "Consistency of angular tuning in the rat vibrissa system." Journal of Neurophysiology **104**(6): 3105-3112.

Henninger, J., R. Krahe, F. Kirschbaum, J. Grewe and J. Benda (2018). "Statistics of natural communication signals observed in the wild identify important yet neglected stimulus regimes in weakly electric fish." The Journal of Neuroscience **38**(24): 5456-5465.

Herrmann, J. (2001). "Dynamical systems for predictive control of autonomous robots." Theory in Biosciences **120**(3): 241-252.

Heth, G., E. Frankenberg, A. Raz and E. Nevo (1987). "Vibrational communication in subterranean mole rats (Spalax ehrenbergi)." Behavioral Ecology and Sociobiology **21**(1): 31-33.

Hines, M. L. and N. T. Carnevale (1997). "The NEURON Simulation Environment." Neural Computation **9**(6): 1179-1209.

Hipp, J., E. Arabzadeh, E. Zorzin, J. Conradt, C. Kayser, M. E. Diamond and P. König (2006). "Texture signals in whisker vibrations." Journal of Neurophysiology **95**(3): 1792-1799.

Hobbs, J. A., R. B. Towal and M. J. Hartmann (2015). "Probability distributions of whisker-surface contact: quantifying elements of the rat vibrissotactile natural scene." Journal of Experimental Biology **218**(Pt 16): 2551-2562.

Hobbs, J. A., R. B. Towal and M. J. Z. Hartmann (2016). "Evidence for functional groupings of vibrissae across the rodent mystacial pad." PLoS Computational Biology **12**(1): 1-36.

Hobbs, J. A., R. B. Towal and M. J. Z. Hartmann (2016). "Spatiotemporal patterns of contact across the rat vibrissal array during exploratory behavior." Frontiers in Behavioral Neuroscience **9**(January): 1-18.

Hofmann, V., J. I. Sanguinetti-Scheck, S. Kunzel, B. Geurten, L. Gomez-Sena and J. Engelmann (2013). "Sensory flow shaped by active sensing: sensorimotor strategies in electric fish." Journal of Experimental Biology **216**(Pt 13): 2487-2500.

Horev, G., A. Saig, P. M. Knutsen, M. Pietr, C. Yu and E. Ahissar (2011). "Motor-sensory convergence in object localization: a comparative study in rats and humans." Philosophical Transactions of the Royal Society B: Biological Sciences **366**(1581): 3070-3076.

Hoyer, P. O. and A. Hyvärinen (2000). "Independent component analysis applied to feature extraction from colour and stereo images." Network: Computation in Neural Systems **11**(3): 191--210.

Huang, J., A. B. Lee and D. Mumford (2000). Statistics of range images. **1:** 324-331 vol.321.

Huang, J., A. B. Lee and D. B. Mumford (2001). "Occlusion models for natural images: A statistical study of a scale-invariant dead leaves model." International Journal of Computer Vision **41**(1).

Huang, N. and M. Elhilali (2017). "Auditory salience using natural soundscapes." The Journal of the Acoustical Society of America **141**(3): 2163.

Huang, Y. and R. P. N. Rao (2011). "Predictive coding." Wiley Interdisciplinary Reviews: Cognitive Science **2**(5): 580-593.

Huckvel, M. (2019). CochSim, University College London.

Huet, L. A., J. W. Rudnicki and M. J. Hartmann (2017). "Tactile sensing with whiskers of various shapes: determining the three-dimensional location of object contact based on mechanical signals at the whisker base." Soft robotics **4**(2): 88-102.

Huet, L. A., C. L. Schroeder and M. J. Z. Hartmann (2015). "Tactile signals transmitted by the vibrissa during active whisking behavior." Journal of Neurophysiology **113**(10): 3511-3518.

Hyvärinen, A. (2010). "Statistical models of natural images and cortical visual representation." Topics in Cognitive Science **2**(2): 251-264.

Hyvarinen, A., M. Gutmann and P. O. Hoyer (2005). "Statistical model of natural stimuli predicts edge-like pooling of spatial frequency channels in V2." BMC Neurosci **6**: 12.

Hyvärinen, A. and P. Hoyer (2000). "Emergence of phase- and shift-invariant features by decomposition of natural images into independent feature subspaces." Neural Computation **12**(7): 1705--1720.

Hyvärinen, A. and P. O. Hoyer (2001). "A two-layer sparse coding model learns simple and complex cell receptive fields and topography from natural images." Vision Research **41**(18): 2413-2423.

Hyvärinen, A. and E. Oja (2000). "Independent component analysis: algorithms and applications." Neural Networks **13**(4): 411-430.

Ito, M. (1985). "Processing of vibrissa sensory information within the rat neocortex." Journal of Neurophysiology **54**(3): 479-490.

Jacob, V., L. Estebanez, J. Le Cam, J. Y. Tiercelin, P. Parra, G. Parésys and D. E. Shulz (2010). "The Matrix: A new tool for probing the whisker-to-barrel system with natural stimuli." Journal of Neuroscience Methods **189**(1): 65-74.

Jacob, V., J. Le Cam, V. Ego-Stengel and D. E. Shulz (2008). "Emergent properties of tactile scenes selectively activate barrel cortex neurons." Neuron **60**(6): 1112-1125.

Jacquin, M. F., W. E. Renehan, R. W. Rhoades and W. M. Panneton (1993). "Morphology and topography of identified primary afferents in trigeminal subnuclei principalis and oralis." J Neurophysiol **70**(5): 1911-1936.

Jadhav, S. P., J. Wolfe and D. E. Feldman (2009). "Sparse temporal coding of elementary tactile features during active whisker sensation." Nature Neuroscience **12**(6): 792-800.

Jones, L. M., S. Lee, J. C. Trageser, D. J. Simons and A. Keller (2004). "Precise temporal responses in whisker trigeminal neurons." Journal of Neurophysiology **92**(1): 665-668.

Juusola, M. and A. S. French (1997). "The efficiency of sensory information coding by mechanoreceptor neurons." Neuron **18**(6): 959-968.

Kaliuzhna, M., T. Stein, T. Rusch, M. Sekutowicz, P. Sterzer and K. J. Seymour (2019). "No evidence for abnormal priors in early vision in schizophrenia." Schizophrenia Research **210**: 245-254.

Kaller, O., L. Bolecek, L. Polak and T. Kratochvil (2016). "Depth map improvement by combining passive and active scanning methods." Radioengineering **25**(3): 536-547.

Kaloti, A. S., E. C. Johnson, C. S. Bresee, S. N. Naufel, M. G. Perich, D. L. Jones and M. J. Hartmann (2016). "Representation of stimulus speed and direction in vibrissal-sensitive regions of the trigeminal nuclei: A comparison of single unit and population responses." PLoS One **11**(7): e0158399.

Kan, Q., R. Rajan, J. Fu, G. Kang and W. Yan (2013). "Elastic modulus of rat whiskers—A key biomaterial in the rat whisker sensory system." Materials Research Bulletin **48**: 5026-5032.

Kaneko, M., N. Kanayama, T. Tsuji and A. Member (1998). "Active antenna for contact sensing." IEEE Transactions on Robotics **14**(2): 278-291.

Karklin, Y. and M. S. Lewicki (2005). "A hierarchical Bayesian model for learning nonlinear statistical regularities in nonstationary  natural signals." Neural Computation **17**(2): 397--423.

Kass, R. E., V. Ventura and C. Cai (2003). "Statistical smoothing of neuronal data." Network **14**(1): 5-15.

Katz, D. (1925). Der Aufbau der Tastwelt. Leipzig, Verlag von Johann Ambrosius Barth.

Kayaert, G., I. Biederman, H. P. Op de Beeck and R. Vogels (2005). "Tuning for shape dimensions in macaque inferior temporal cortex." European Journal of Neuroscience **22**(1): 212-224.

Kenton, B., L. Kruger and M. Woo (1971). "Two classes of slowly adapting mechanoreceptor fibres in reptile cutaneous nerve." The Journal of Physiology **212**(1): 21-44.

Kepecs, A., N. Uchida and Z. F. Mainen (2006). "The sniff as a unit of olfactory processing." Chemical Senses **31**(2): 167-179.

Ketchen, D. J. and C. L. Shook (1996). "The application of cluster analysis in strategic management research: an analysis and critique." Strategic management journal **17**(6): 441-458.

Khalsa, P. S., R. M. Friedman, M. A. Srinivasan and R. H. Lamotte (1998). "Encoding of shape and orientation of objects indented into the monkey fingerpad by populations of slowly and rapidly adapting mechanoreceptors." Journal of Neurophysiology **79**(6): 3238-3251.

Kilteni, K., B. J. Andersson, C. Houborg and H. H. Ehrsson (2018). "Motor imagery involves predicting the sensory consequences of the imagined movement." Nature Communications **9**(1): 1617.

Kilteni, K., C. Houborg and H. H. Ehrsson (2019). "Rapid learning and unlearning of predicted sensory delays in self-generated touch." Elife **8**.

Kim, D. E. and R. Möller (2007). "Biomimetic whiskers for shape recognition." Robotics and Autonomous Systems **55**(3): 229-243.

Kimchi, T., M. Reshef and J. Terkel (2005). "Evidence for the use of reflected self-generated seismic waves for spatial orientation in a blind subterranean mammal." Journal of Experimental Biology **208**(Pt 4): 647-659.

Kiss, G. (1991). Autonomous agents, AI and chaos theory. From Animals to Animats: Proceedings of the First International Conference on Simulation of Adaptive Behavior, MITP**:** 518-524.

Kitazawa, T. and F. M. Rijli (2018). "Barrelette map formation in the prenatal mouse brainstem." Curr Opin Neurobiol **53**: 210-219.

Kleinfeld, D., E. Ahissar and M. E. Diamond (2006). "Active sensation: insights from the rodent vibrissa sensorimotor system." Current Opinion in Neurobiology **16**(4): 435-444.

Kleinfeld, D., R. W. Berg and S. M. O'Connor (1999). "Anatomical loops and their electrical dynamics in relation to whisking by rat." Somatosensory and Motor Research **16**(2): 69-88.

Knutsen, P. M. (2016). Whisking Kinematics. Scholarpedia of Touch. T. Prescott, E. Ahissar and E. Izhikevich. Paris, Atlantis Press**:** 615-625.

Knutsen, P. M., A. Biess and E. Ahissar (2008). "Vibrissal kinematics in 3D: Tight coupling of azimuth, elevation, and torsion across different whisking modes." Neuron **59**(1): 35-42.

Knutsen, P. M., D. Derdikman and E. Ahissar (2005). "Tracking whisker and head movements in unrestrained behaving rodents." Journal of Neurophysiology **93**(4): 2294-2301.

Konda, V. R. and J. N. Tsitsiklis (1999). Actor-critic algorithms. Advances in neural information processing systems 12: Proceedings of the 1999 conference. S. A. Solla, T. K. Leen and K. Müller. Denver, CO, MIT Press. **12:** 1008-1014.

Krakauer, J. W., A. A. Ghazanfar, A. Gomez-Marin, M. A. MacIver and D. Poeppel (2017). "Neuroscience needs behavior: Correcting a reductionist bias." Neuron **93**(3): 480-490.

Krupa, D. J., M. S. Matell, A. J. Brisben, L. M. Oliveira and M. A. L. Nicolelis (2001). "Behavioral properties of the trigeminal somatosensory system in rats performing whisker-dependent tactile discriminations." The Journal of Neuroscience **21**(15): 5752.

Kwegyir-Afful, E. E., S. Marella and D. J. Simons (2008). "Response properties of mouse trigeminal ganglion neurons." Somatosens Mot Res **25**(4): 209-221.

Lamotte, R. H., M. A. Srinivasan, C. Lu and A. Klusch-Petersen (1994). "Cutaneous neural codes for shape." Canadian Journal of Physiology and Pharmacology **72**(5): 498-505.

Laughlin, S. B. (1981). "A simple coding procedure enhances a neuron's information capacity." Zeitschrift Naturforschung **36**: 910-912.

Lee, A., J. Huang and D. Mumford (2000). "Random-collage model for natural images." International Journal of Computer Vision.

Lee, K. J. and T. A. Woolsey (1975). "A proportional relationship between peripheral innervation density and cortical neuron number in the somatosensory system of the mouse." Brain Research **99**(2): 349-353.

Lefevre, L., E. Courtiol, S. Garcia, M. Thevenet, B. Messaoudi and N. Buonviso (2016). "Significance of sniffing pattern during the acquisition of an olfactory discrimination task." Behavioural Brain Research **312**: 341-354.

Leszczynski, M. and C. E. Schroeder (2019). "The role of neuronal oscillations in visual active sensing." Frontiers in Integrative Neuroscience **13**: 32.

Lewicki, M. S. (2002). "Efficient coding of natural sounds." Nature neuroscience **5**(4): 356-363.

Lewicki, M. S., B. A. Olshausen, A. Surlykke and C. F. Moss (2014). "Scene analysis in the natural environment." Frontiers in Psychology **5**(APR): 1-21.

Li, C., M. Gunther and T. E. Boult (2018). Eclipse: Ensembles of centroids leveraging iteratively processed spatial eclipse clustering. 2018 IEEE Winter Conference on Applications of Computer Vision (WACV), IEEE.

Lichtenstein, S. H., G. E. Carvell and D. J. Simons (1990). "Responses of rat trigeminal ganglion neurons to movements of vibrissae in different directions." Somatosens Mot Res **7**(1): 47-65.

Liu, Y. H. and X. J. Wang (2001). "Spike-frequency adaptation of a generalized leaky integrate-and-fire model neuron." J Comput Neurosci **10**(1): 25-45.

Lo, F. S. and R. S. Erzurumlu (2016). "Sensory Activity-Dependent and Sensory Activity-Independent Properties of the Developing Rodent Trigeminal Principal Nucleus." Dev Neurosci **38**(3): 163-170.

Loomis, J. M. and S. J. Lederman (1986). Tactual perception. Handbook of perception and human performance, Vol. 2: Cognitive processes and performance. Oxford, England, John Wiley & Sons**:** 1-41.

Lottem, E. and R. Azouz (2011). "A unifying framework underlying mechanotransduction in the somatosensory system." Journal of Neuroscience **31**(23): 8520-8532.

Lu, L., Y. Jia, J. B. Kirunda, Y. Xu, M. Ge, Q. Pei and L. Yang (2019). "Effects of noise and synaptic weight on propagation of subthreshold excitatory postsynaptic current signal in a feed-forward neural network." Nonlinear Dynamics **95**(2): 1673-1686.

Lucianna, F. A., A. L. Albarracín, S. M. Vrech, F. D. Farfán and C. J. Felice (2016). "The mathematical whisker: A review of numerical models of the rat's vibrissa biomechanics." Journal of Biomechanics **49**(10): 2007-2014.

Ma, P. M. and T. A. Woolsey (1984). "Cytoarchitectonic correlates of the vibrissae in the medullary trigeminal complex of the mouse." Brain Res **306**(1-2): 374-379.

Maloney, L. T. and B. A. Wandell (1986). "Color constancy: a method for recovering surface spectral reflectance." Journal of the Optical Society of America A **3**(1): 29-29.

Manfredi, L. R., H. P. Saal, K. J. Brown, M. C. Zielinski, J. F. Dammann, V. S. Polashock and S. J. Bensmaia (2014). "Natural scenes in tactile texture." Journal of neurophysiology **111**: 1792-1802.

Marder, E. (2011). "Variability, compensation, and modulation in neurons and circuits." Proceedings of the National Academy of Sciences **108 Suppl 3**: 15542-15548.

Marr, D. (1982). "VISION." 41.

Mashlakov, A., V. Tikka, L. Lensu, A. Romanenko and S. Honkapuro (2019). Hyper-parameter optimization of multi-attention recurrent neural network for battery state-of-charge forecasting. EPIA Conference on Artificial Intelligence, Springer.

Mason, W. P. (1962). "Uses of ultrasonics in radio, radar and sonar systems." Proceedings of the IRE **50**(5): 1374-1384.

Matthews, D. W., M. Deschênes, T. Furuta, J. D. Moore, F. Wang, H. J. Karten and D. Kleinfeld (2015). "Feedback in the brainstem: An excitatory disynaptic pathway for control of whisking." Journal of Comparative Neurology **523**(6): 921-942.

Mehta, S. B. and D. Kleinfeld (2004). "Frisking the whiskers: patterned sensory input in the rat vibrissa system." Neuron **41**(2): 181-184.

Melaragno, H. P. and W. Montagna (1953). "The tactile hair follicles in the mouse." The Anatomical Record **115**(2): 129-149.

Mihaylova, L., T. Lefebvre, H. Bruyninckx, G. K. and D. S. J. (2002). Active sensing for robotics – A survey. Proc. 5 th Int'l Conf. On Numerical Methods and Applications.

Mitchinson, B., R. A. Grant, K. Arkley, V. Rankov, I. Perkon and T. J. Prescott (2011). "Active vibrissal sensing in rodents and marsupials." Philosophical Transactions of the Royal Society B: Biological Sciences **366**(1581): 3037-3048.

Mitchinson, B., K. N. Gurney, P. Redgrave, C. Melhuish, A. G. Pipe, M. Pearson, I. Gilhespy and T. J. Prescott (2004). "Empirically inspired simulated electro-mechanical model of the rat mystacial follicle-sinus complex." Proceedings of the Royal Society B: Biological Sciences **271**(1556): 2509-2516.

Mitchinson, B., C. J. Martin, R. a. Grant and T. J. Prescott (2007). "Feedback control in active sensing: rat exploratory whisking is modulated by environmental contact." Proceedings. Biological sciences / The Royal Society **274**(1613): 1035-1041.

Mlynarski, W. and J. Jost (2014). "Statistics of natural binaural sounds." PLoS One **9**(10): e108968.

Mlynarski, W. F. and A. M. Hermundstad (2021). "Efficient and adaptive sensory codes." Nature Neuroscience **24**(7): 998-1009.

Montemurro, M. A., S. Panzeri, M. Maravall, A. Alenda, M. R. Bale, M. Brambilla and R. S. Petersen (2007). "Role of precise spike timing in coding of dynamic vibrissa stimuli in somatosensory thalamus." Journal of Neurophysiology **98**(4): 1871-1882.

Moore, C. I., S. B. Nelson and M. Sur (1999). "Dynamics of neuronal processing in rat somatosensory cortex." Trends in Neurosciences **22**(11): 513-520.

Morley, S. K., T. V. Brito and D. T. Welling (2018). "Measures of model performance based on the log accuracy ratio." Space Weather **16**(1): 69-88.

Moss, C. F. and A. Surlykke (2010). "Probing the natural scene by echolocation in bats." Frontiers in Behavioral Neuroscience **4**: 1-16.

Moutoussis, M., P. Fearon, W. El-Deredy, R. J. Dolan and K. J. Friston (2014). "Bayesian inferences about the self (and others): a review." Consciousness and Cognition **25**: 67-76.

Muniak, M. A., S. Ray, S. S. Hsiao, J. F. Dammann and S. J. Bensmaia (2007). "The neural coding of stimulus intensity: linking the population response of mechanoreceptive afferents with psychophysical behavior." J Neurosci **27**(43): 11687-11699.

Nascimento, S. M. C., K. Amano and D. H. Foster (2016). "Spatial distributions of local illumination color in natural scenes." Vision Research **120**: 39-44.

Neimark, M. A., M. L. Andermann, J. J. Hopfield and C. I. Moore (2003). "Vibrissa resonance as a transduction mechanism for tactile encoding." The Journal of neuroscience : the official journal of the Society for Neuroscience **23**(16): 6499-6509.

Neisser, U. (1976). Cognition and reality: Principles and implications of cognitive psychology. New York, NY, US, W H Freeman/Times Books/ Henry Holt & Co.

Nelson, M. E. and M. A. MacIver (2006). Sensory acquisition in active sensing systems. Journal of Comparative Physiology A: Neuroethology, Sensory, Neural, and Behavioral Physiology. **192:** 573-586.

Nguyen, Q.-T. and D. Kleinfeld (2005). "Positive Feedback in a Brainstem Tactile Sensorimotor Loop." Neuron **45**: 447-457.

Nollet, J. A. (1743). Leçons de physique expérimentale par M. l'Abbé Nollet, Chez les Frères Guérin.

Okorokova, E. V., Q. He and S. J. Bensmaia (2018). "Biomimetic encoding model for restoring touch in bionic hands through a nerve interface." Journal of Neural Engineering **15**(6): 066033.

Ollerenshaw, D. R., H. J. V. Zheng, D. C. Millard, Q. Wang and G. B. Stanley (2014). "The adaptive trade-off between detection and discrimination in cortical representations and behavior." Neuron **81**(5): 1152-1164.

Olshausen, B. A. and D. J. Field (1996). Emergence of simple-cell receptive field properties by learning a sparse code for natural images. **381:** 607-609.

Olshausen, B. A. and D. J. Field (1996). Emergence of simple-cell receptive field properties by learning a sparse code for natural images. Nature. **381:** 607-609.

Olshausen, B. A. and D. J. Field (1996). "Natural image statistics and efficient coding." Network: Computation in Neural Systems **7**(2): 333-339.

Olshausen, B. A. and D. J. Field (1997). "Strategy Employed by V1 ?" Vision Research **37**(23): 3311-3325.

Parise, C. V., K. Knorre and M. O. Ernst (2014). "Natural auditory scene statistics shapes human spatial hearing." Proceedings of the National Academy of Sciences **111**(16): 6104-6108.

Park, I. M., S. Seth, A. R. Paiva, L. Li and J. C. Principe (2013). "Kernel methods on spike train space for neuroscience: a tutorial." IEEE Signal Processing Magazine **30**(4): 149-160.

Pasupathy, A., P. J. Fitzgerald, S. S. Hsiao, C. E. Connor, J. M. Yau, A. Pasupathy, P. J. Fitzgerald, S. S. Hsiao and C. E. Connor (2009). "Analogous intermediate shape coding in vision and touch." Proceedings of the National Academy of Sciences **106**(38): 16457-16462.

Patrizi, G. and B. L. Munger (1966). "The ultrastructure and innervation of rat vibrissae." J Comp Neurol **126**(3): 423-435.

Patrizi, G. and B. L. Munger (1966). "The ultrastructure and innervation of rat vibrissae." Journal of Comparative Neurology **126**(3): 423-&.

Petersen, R. S., A. Colins Rodriguez, M. H. Evans, D. Campagner and M. S. E. Loft (2020). "A system for tracking whisker kinematics and whisker shape in three dimensions." PLoS Comput Biol **16**(1): e1007402.

Petersen, R. S. and M. E. Diamond (2000). "Spatial–temporal distribution of whisker-evoked activity in rat somatosensory cortex and the coding of stimulus location." Journal of Neuroscience **20**(16): 6135-6143.

Phillips, K. A., L. M. S. Goodchild, M. E. Haas, M. J. Ulyan and S. Petro (2004). "Use of visual, acoustic, and olfactory information during embedded invertebrate foraging in brown capuchins (Cebus apella)." Journal of Comparative Psychology **118**(2): 200-205.

Polley, D. B., J. L. Rickert and R. D. Frostig (2005). "Whisker-based discrimination of object orientation determined with a rapid training paradigm." Neurobiology of Learning and Memory **83**(2): 134-142.

Poulet, J. F. A. and B. Hedwig (2003). "A corollary discharge mechanism modulates central auditory processing in singing crickets." Journal of Neurophysiology **89**(3): 1528-1540.

Prescott, T. J., M. E. Diamond and A. M. Wing (2011). "Active touch sensing." Philosophical Transactions of the Royal Society B: Biological Sciences **366**(1581): 2989-2995.

Prigg, T., D. Goldreich, G. E. Carvell and D. J. Simons (2002). "Texture discrimination and unit recordings in the rat whisker/barrel system." Physiology & Behavior **77**(4-5): 671-675.

Pubols, B. H., Jr., P. J. Donovick and L. M. Pubols (1973). "Opossum trigeminal afferents associated with vibrissa and rhinarial mechanoreceptors." Brain, Behavior and Evolution **7**(5): 360-381.

Pye, J. D. (1960). "A theory of echolocation by bats." The Journal of Laryngology & Otology **74**(10): 718-729.

Quist, B. W., R. A. Faruqi and M. J. Z. Hartmann (2011). "Variation in Young's modulus along the length of a rat vibrissa." Journal of Biomechanics.

Quist, B. W. and M. J. Hartmann (2012). "Mechanical signals at the base of a rat vibrissa: the effect of intrinsic vibrissa curvature and implications for tactile exploration." Journal of Neurophysiology **107**(9): 2298-2312.

Quist, B. W., V. Seghete, L. A. Huet, T. D. Murphey and M. J. Hartmann (2014). "Modeling forces and moments at the base of a rat vibrissa during noncontact whisking and whisking against an object." The Journal of Neuroscience **34**(30): 9828-9844.

Ramirez, A., E. A. Pnevmatikakis, J. Merel, L. Paninski, K. D. Miller and R. M. Bruno (2014). "Spatiotemporal receptive fields of barrel cortex revealed by reverse correlation of synaptic input." Nature Neuroscience **17**(6): 866-875.

Randi, F. and A. M. Leifer (2020). "Measuring and modeling whole-brain neural dynamics in Caenorhabditis elegans." Current Opinion in Neurobiology **65**: 167-175.

Rao, R. P. N. and D. H. Ballard (1999). "Predictive coding in the visual cortex: a functional interpretation of some extra-classical receptive-field effects." Nature Neuroscience **2**(1): 79–87.

Renehan, W. E. and B. L. Munger (1986). "Degeneration and regeneration of peripheral nerve in the rat trigeminal system. I. Identification and characterization of the multiple afferent innervation of the mystacial vibrissae." Journal of Comparative Neurology **246**(1): 129-145.

Rice, F. L., A. Mance and B. L. Munger (1986). "A comparative light microscopic analysis of the sensory innervation of the mystacial pad. I. Innervation of vibrissal follicle-sinus complexes." Journal of Comparative Neurology **252**(2): 154-174.

Risoud, M., J. N. Hanson, F. Gauvrit, C. Renard, P. E. Lemesre, N. X. Bonne and C. Vincent (2018). "Sound source localization." European Annals of Otorhinolaryngology, Head and Neck Diseases **135**(4): 259-264.

Ritt, J. T., M. L. Andermann and C. I. Moore (2008). "Embodied information processing: vibrissa mechanics and texture features shape micromotions in actively sensing rats." Neuron **57**(4): 599-613.

Rousseeuw, P. J. (1987). "Silhouettes: a graphical aid to the interpretation and validation of cluster analysis." Journal of computational and applied mathematics **20**: 53-65.

Ruderman, D. L. (1994). "The statistics of natural images." Network: Computation in Neural Systems **5**: 517-548.

Ruderman, D. L., T. W. Cronin and C.-C. Chiao (1998). "Statistics of cone responses to natural images: implications for visual coding." Journal of the Optical Society of America A **15**(8): 2036-2045.

Saal, H. P., B. P. Delhaye, B. C. Rayhaun and S. J. Bensmaia (2017). "Simulating tactile signals from the whole hand with millisecond precision." Proceedings of the National Academy of Sciences of the United States of America: 201704856-201704856.

Sakamoto, M. and J. Watanabe (2017). "Exploring tactile perceptual dimensions using materials associated with sensory vocabulary." Frontiers in Psychology **8**: 569.

Samonds, J. M., W. S. Geisler and N. J. Priebe (2018). "Natural image and receptive field statistics predict saccade sizes." Nature Neuroscience **21**: 1591-1599.

Schenkman, B. N. (2017). "Human echolocation in different situations and rooms." The Journal of the Acoustical Society of America **141**(5): 3452.

Scholz, G. R. and C. D. Rahn (2004). "Profile sensing with an actuated whisker." IEEE Transactions on Robotics and Automation **20**(1): 124-127.

Schroeder, C. E., D. A. Wilson, T. Radman, H. Scharfman and P. Lakatos (2010). "Dynamics of active sensing and perceptual selection." Current Opinion in Neurobiology **20**(2): 172-176.

Schuller, G. (1979). "Vocalization influences auditory processing in collicular neurons of the CF-FM-bat,Rhinolophus ferrumequinum." Journal of comparative physiology **132**(1): 39-46.

Schütz, A. C., D. I. Braun and K. R. Gegenfurtner (2011). "Eye movements and perception: A selective review." Journal of Vision **11**(5): 1-30.

Schwarz, C. (2016). "The Slip Hypothesis: Tactile perception and its neuronal bases." Trends in Neurosciences **39**(7): 449-462.

Seon M. Han, H. B., Timothy Wei (1999). "Dynamics of transversely vibrating beams using four engineering theories." Journal of Sound and Vibration **5**(255): 935-988.

Shao, F., X. J. Chen, C. J. Barnes and B. Henson (2010). "A novel tactile sensation measurement system for qualifying touch perception." Proceedings of the Institution of Mechanical Engineers, Part H **224**(1): 97-105.

Sherman, D., T. Oram, D. Deutsch, G. Gordon, E. Ahissar and D. Harel (2013). "Tactile modulation of whisking via the brainstem loop: statechart modeling and experimental validation." PLoS One **8**(11): e79831.

Shipley, M. T. (1974). "Response characteristics of single units in rats trigeminal nuclei to vibrissa displacements." Journal of Neurophysiology **37**(1): 73-90.

Shuler, M. G., D. J. Krupa and M. A. L. Nicolelis (2002). "Integration of bilateral whisker stimuli in rats: Role of the whisker barrel cortices." Cerebral Cortex **12**(1): 86-97.

Simoncelli, E. P. and B. A. Olshausen (2001). "Natural image statistics and neural representation." Annual Review of Neuroscience **24**: 1193-1216.

Simons, D. J. (1978). "Response properties of vibrissa units in rat SI somatosensory neocortex." Journal of Neurophysiology **41**(3): 798-820.

Simons, D. J. (1983). "Multi-whisker stimulation and its effects on vibrissa units in rat SML Barrel Cortex." Brain Research **276**(1): 178-182.

Simons, D. J. (1985). "Temporal and spatial integration in the rat SI vibrissa cortex." Journal of Neurophysiology **54**(3): 615-635.

Smith, E. C. and M. S. Lewicki (2006). "Efficient auditory coding." Nature **439**(7079): 978-982.

Sohangir, S. and D. Wang (2017). "Improved sqrt-cosine similarity measurement." Journal of Big Data **4**(1): 25.

Solomon, J. H. and M. J. Z. Z. Hartmann (2010). "Extracting object contours with the sweep of a robotic whisker using torque information." The International Journal of Robotics Research **29**(9): 1233-1245.

Srinivasan, M. V. and R. H. Lamotte (1991). Encoding of shape in cutaneous mechanoreceptors. Information processing in the somatosensory system. O. Franzen and J. Westman, Macmillan International Higher Education. **57**.

Stamper, S. A., G. E. Carrera, E. W. Tan, V. Fugere, R. Krahe and E. S. Fortune (2010). "Species differences in group size and electrosensory interference in weakly electric fishes: implications for electrosensory processing." Behavioural Brain Research **207**(2): 368-376.

Stamper, S. A., M. S. Madhav, N. J. Cowan and E. S. Fortune (2019). Using control theory to characterize active sensing in weakly electric fishes. Electroreception: Fundamental Insights from Comparative Approaches. B. Carlson, J. Sisneros, A. P. AN and R. Fay. New York, Springer Science+Business Media, LLC. **70**.

Stansbury, D. E., T. Naselaris and J. L. Gallant (2013). "Natural scene statistics account for the representation of scene categories in human visual cortex." Neuron **79**(5): 1025-1034.

Starostin, E. L., R. A. Grant, G. Dougill, G. H. M. van der Heijden and V. G. A. Goss (2020). "The Euler spiral of rat whiskers." Science Advances **6**(3): eaax5145.

Steinbuch, J. G. (1811). Beytrag zur Physiologie der Sinne. Nürnberg, Johann Leonhard Schrag.

Stuttgen, M. C., S. Kullmann and C. Schwarz (2008). "Responses of rat trigeminal ganglion neurons to longitudinal whisker stimulation." Journal of Neurophysiology **100**(4): 1879-1884.

Su, C. C., A. C. Bovik, L. K. Cormack and Ieee (2011). Natural scene statistics of color and range. 18th IEEE International Conference on Image Processing (ICIP), Brussels, BELGIUM.

Surlykke, A., K. Ghose and C. F. Moss (2009). "Acoustic scanning of natural scenes by echolocation in the big brown bat, Eptesicus fuscus." Journal of Experimental Biology **212**(Pt 7): 1011-1020.

Sussillo, D. (2014). "Neural circuits as computational dynamical systems." Current Opinion in Neurobiology **25**: 156-163.

Tal, D. and E. L. Schwartz (1997). "Computing with the Leaky Integrate-and-Fire Neuron: Logarithmic Computation and Multiplication." Neural Computation **9**(2): 305-318.

Tan, E. W., J. M. Nizar, G. E. Carrera and E. S. Fortune (2005). "Electrosensory interference in naturally occurring aggregates of a species of weakly electric fish, Eigenmannia virescens." Behavioural Brain Research **164**(1): 83-92.

The, L., M. L. Wallace, C. H. Chen, E. Chorev and M. Brecht (2013). "Structure, function, and cortical representation of the rat submandibular whisker trident." The Journal of Neuroscience **33**(11): 4815-4824.

Timofeeva, E., P. Lavallee, D. Arsenault and M. Deschenes (2004). "Synthesis of multiwhisker-receptive fields in subcortical stations of the vibrissa system." Journal of Neurophysiology **91**(4): 1510-1515.

Torralba, A. and A. Oliva (2003). "Statistics of natural image categories." Network: Computation in Neural Systems **14**(3): 391-412.

Towal, R. B., B. W. Quist, V. Gopal, J. H. Solomon and M. J. Hartmann (2011). "The morphology of the rat vibrissal array: a model for quantifying spatiotemporal patterns of whisker-object contact." PLoS Comput Biol **7**(4): e1001120.

Towal, R. B., B. W. Quist, V. Gopal, J. H. Solomon and M. J. Z. Hartmann (2011). "The morphology of the rat vibrissal array: A model for quantifying spatiotemporal patterns of whisker-object contact." PLoS Computational Biology **7**(4).

Traer, J. and J. H. McDermott (2016). "Statistics of natural reverberation enable perceptual separation of sound and space." Proceedings of the National Academy of Sciences **113**(48): E7856-E7865.

Ulanovsky, N., M. B. Fenton, A. Tsoar and C. Korine (2004). "Dynamics of jamming avoidance in echolocating bats." Proceedings of the Royal Society B: Biological Sciences **271**(1547): 1467-1475.

Uyanik, I., S. A. Stamper, N. J. Cowan and E. S. Fortune (2019). "Sensory cues modulate smooth pursuit and active sensing movements." Frontiers in Behavioral Neuroscience **13**: 59.

van der Horst, B. J. and A. M. Kappers (2008). "Using curvature information in haptic shape perception of 3D objects." Experimental brain Research **190**(3): 361-367.

Van Hateren, J. H. and D. L. Ruderman (1998). "Independent component analysis of natural image sequences yields spatio-temporal filters similar to simple cells in primary visual cortex." Proceeding The Royal Society **265**: 2315-2320.

van Hateren, J. H. and A. van der Schaaf (1998). "Independent component filters of natural images compared with simple cells in primary visual cortex." Proceedings of the Royal Society B-Biological Sciences **265**(1394): 359-366.

van Kuilenburg, J., M. A. Masen and E. van der Heide (2013). "A review of fingerpad contact mechanics and friction and how this affects tactile perception." Proceedings of the Institution of Mechanical Engineers, Part J: Journal of Engineering Tribology **229**(3): 243-258.

Vaxenburg, R., I. Wyche, K. Svoboda, A. L. Efros and S. A. Hires (2018). "Dynamic cues for whisker-based object localization: An analytical solution to vibration during active whisker touch." PLOS Computational Biology **14**(3): e1006032-e1006032.

Victor, J. D. and K. P. Purpura (1996). "Nature and precision of temporal coding in visual cortex: a metric-space analysis." Journal of Neurophysiology **76**(2): 1310-1326.

Victor, J. D. and K. P. Purpura (1997). "Sensory coding in cortical neurons. Recent results and speculations." Annals of the New York Academy of Sciences **835**: 330-352.

Vilankar, K. P., J. R. Golden, D. M. Chandler and D. J. Field (2014). "Local edge statistics provide information regarding occlusion and nonocclusion edges in natural scenes." Journal of Vision **14**(9).

Vincent, S. B. (1912). The functions of the vibrissae in the behavior of the white rat. Cambridge, Mass.

Vincent, S. B. (1913). "The tactile hair of the white rat." Journal of Comparative Neurology **23**(1): 1-34.

Von Helmholtz, H. (1867). Handbuch der physiologischen Optik, Voss.

von Helmholtz, H. (1879). Die Thatsachen in der Wahrnehmung: Rede gehalten zur Stiftungfeier der Friedrich-Wilhelms-Universität zu Berlin am 3. August 1878, A. Hirschwald.

Waite, P. M. and B. G. Cragg (1982). "The peripheral and central changes resulting from cutting or crushing the afferent nerve supply to the whiskers." Proceedings of the Royal Society B: Biological Sciences **214**(1195): 191-211.

Wang, R., M. Veloso and S. Seshan (2016). Active sensing data collection with autonomous mobile robots. **2016-:** 2583-2588.

Wang, X. J. (1998). "Calcium coding and adaptive temporal computation in cortical pyramidal neurons." Journal of Neurophysiology **79**(3): 1549-1566.

Ward, R. and R. Ward (2009). "Representation in dynamical agents." <u>Neural Networks</u> **22**(3): 258-266.

Warren, W. H. (2006). "The dynamics of perception and action." <u>Psychological Review</u> **113**(2): 358-389.

Weber, A. I., H. P. Saal, J. D. Lieber, J.-W. Cheng, L. R. Manfredi, J. F. Dammann and S. J. Bensmaia (2013). "Spatial and temporal codes mediate the tactile perception of natural textures." <u>Proceedings of the National Academy of Sciences</u>.

Wellnitz, S. A., D. R. Lesniak, G. J. Gerling and E. A. Lumpkin (2010). "The regularity of sustained firing reveals two populations of slowly adapting touch receptors in mouse hairy skin." <u>Journal of Neurophysiology</u> **103**(6): 3378-3388.

Wohrer, A. and P. Kornprobst (2009). "Virtual Retina: a biological retina model and simulator, with contrast gain control." <u>Journal of Computational Neuroscience</u> **26**(2): 219-249.

Wolfe, J., D. N. Hill, S. Pahlavan, P. J. Drew, D. Kleinfeld and D. E. Feldman (2008). "Texture coding in the rat whisker system: slip-stick versus differential resonance." <u>PLoS Biol</u> **6**(8): e215.

Woolsey, T. A. and H. Van der Loos (1970). "The structural organization of layer IV in the somatosensory region (S I) of mouse cerebral cortex: The description of a cortical field composed of discrete cytoarchitectonic units." <u>Brain Research</u> **17**(2): 205-242.

Wundt, W. M. (1902). <u>Outlines of psychology</u>. Leipzig, W. Englemann.

Y.I. Li, A. S. W. W. (2006). "Neurophysiology of sensory perceptions." <u>Clothing Biosensory Engineering</u>: 28-59.

Yan, W., Q. Kan, K. Kergrene, G. Kang, X. Q. Feng and R. Rajan (2013). "A truncated conical beam model for analysis of the vibration of rat whiskers." <u>Journal of Biomechanics</u> **46**(12): 1987-1995.

Yang, A. E., H. M. Belli and M. J. Z. Hartmann (2019). "Quantification of vibrissal mechanical properties across the rat mystacial pad." <u>Journal of Neurophysiology</u> **121**(5): 1879-1895.

Yang, S. C., M. Lengyel and D. M. Wolpert (2016). "Active sensing in the categorization of visual patterns." <u>Elife</u> **5**.

Yang, S. C., D. M. Wolpert and M. Lengyel (2018). "Theoretical perspectives on active sensing." <u>Current Opinion in Behavioral Sciences</u> **11**: 100-108.

Yu, N., G. Hupe, A. Longtin and J. E. Lewis (2019). "Electrosensory contrast signals for interacting weakly electric fish." <u>Frontiers in Integrative Neuroscience</u> **13**: 36.

Zhuang, C., J. Kubilius, M. J. Z. Hartmann and D. Yamins (2017). <u>Toward goal-driven neural network models for the rodent whisker-trigeminal system</u>. NIPS.

Zucker, E. and W. I. Welker (1969). "Coding of somatic sensory input by vibrissae neurons in rats trigeminal ganglion." <u>Brain Research</u> **12**(1): 138-&.

Zucker, E. and W. I. Welker (1969). "Coding of somatic sensory input by vibrissae neurons in the rat's trigeminal ganglion." <u>Brain Res</u> **12**(1): 138-156.

Zweifel, N. O., N. E. Bush, I. Abraham, T. D. Murphey and M. J. Z. Hartmann (2021). "A dynamical model for generating synthetic data to quantify active tactile sensing behavior in the rat." Proceedings of the National Academy of Sciences **118**(27).

# APPENDIX A

## Computational models of the early stages of neural processing in the rat vibrissal system

Tianhao Lei[1], Nadina O. Zweifel[2], Mitra J. Z. Hartmann[2,3]

[1]Department of Neurobiology, Northwestern University, Evanston, IL, 60208, USA
[2]Department of Biomedical Engineering, Northwestern University, Evanston, IL, 60208, USA
[3]Department of Mechanical Engineering, Northwestern University, Evanston, IL, 60208, USA

## A.1 Abstract

Rats use vibrissae (whiskers) heavily to sense the surrounding environment. The information of whisker deflection is transduced into mechanics at the whisker base. Mechanoreceptors in the whisker follicles receive this mechanical information and transduce it into neural activity. These neural signals are further transmitted into trigeminal nuclei in the brainstem for processing by trigeminal ganglion neurons. In the early stages of neural processing in rat vibrissal system, it is unclear how the neurons encode the mechanosensory stimulation into neural activity. Here, we constructed a computational model of the trigeminal ganglion (Vg) neuron of the rat's primary vibrissal system which receives two-dimensional bending moments and their derivatives as inputs. The model contains four free parameters which represents four properties of each neuron: magnitude threshold ($\alpha$), neural adaptation ($\beta$), response nonlinearity ($\gamma$), and angular preference ($\theta$). By fitting the firing rate elicited by free whisker deflection under various conditions, the model successfully identifies the population distributions of some of the most important properties of realistic Vg neurons and predicts the neural behavior in the SpVi, a downstream structure in which neurons receive multi-whisker input during passive sensing. The cluster center of the parameters may indicate three typical classification of Vg neurons: slowly adapting with low threshold, slowly adapting with high threshold, and rapidly adapting with high threshold. This result provides an

interesting insight about a heuristic approach to approximating the behavior of neurons in the central neural pathway of the vibrissal system.

## A.2 Introduction

Rodents extensively use their vibrissae (whisker) to sense the surrounding world. These whiskers are long and stiff tapered hairs which grow on both sides (~30 whiskers on each side) of a rodent's snout (Brecht, Preilowski et al. 1997). The natural shape of the whiskers can be well approximated by a parabola (Towal, Quist et al. 2011) or an Euler spiral (Starostin, Grant et al. 2020); the whiskers are arranged in a grid-like manner (The, Wallace et al. 2013).

On the whisker pad, each whisker is embedded in a follicle. The vibrissal shaft is fixed in place by the conical body embedded in the surface of the epidermis. The internal sheath, which wraps around the part of the vibrissal shaft inside the follicle, is innervated by nerve endings and various mechanoreceptors (Melaragno and Montagna 1953, Brecht, Preilowski et al. 1997). These sensitive peripheral neural structures transduce mechanical information gathered from the displacement, bending, and rotation of whiskers (Bagdasarian, Szwed et al. 2013). In fact, they are so sensitive that less than 0.1 degree of rotation of the whiskers can be detected by the nervous system (Gibson and Welker 1983).

Each follicle is innervated by 150-200 trigeminal ganglion neurons that spread their countless neural endings of mechanoreceptors around the sheath (Lee and Woolsey 1975, Waite and Cragg 1982, Renehan and Munger 1986). Trigeminal ganglion (Vg) neurons are the crucial bridge transducing the peripheral sensory inputs to neural spikes. Extensive studies have shown that one Vg neuron only innervates one whisker follicle (Fitzgerald 1940, Zucker and Welker 1969, Lichtenstein, Carvell et al. 1990). Vg neurons consist of a pseudo-unipolar cell body, with one

ending receiving the signals from the attached mechanoreceptors and another ending passing the information to the brainstem trigeminal complex (Erzurumlu and Killackey 1980, Durham and Woolsey 1984, Bates and Killackey 1985). Each Vg neurons is sensitive to certain directions of whisker deflection, its angular preference (Lichtenstein, Carvell et al. 1990, Kwegyir-Afful, Marella et al. 2008), whereas the different types of mechanoreceptors shape the dynamics of Vg neuron firing. Morphologically, the mechanoreceptors can be classified into Merkel cell-neurite complexes (Halata, Grim et al. 2003), lanceolate receptors, Ruffini corpuscles—sometimes referred to as reticular endings, and free nerve endings (Patrizi and Munger 1966, Renehan and Munger 1986, Rice, Mance et al. 1986). These types exhibit different tuning properties and sensitivity to the amplitude, frequency, direction, velocity, and acceleration of the spatial deformation of their microenvironments (Fitzgerald 1940, Zucker and Welker 1969, Hahn 1971, Pubols, Donovick et al. 1973, Dykes 1975, Lichtenstein, Carvell et al. 1990). In addition, they have different levels of adaptation (Gibson and Welker 1983). Research found that the adaptation responses of mechanoreceptors can vary under certain conditions, and that the level of adaptation has a continuous spectrum across all the different types (Gibson and Welker 1983). Recently, Furuta et al. (2016) demonstrated clearly that Merkel endings in vibrissal follicles are slowly adapting when vibrissae are stimulated in a preferred angle but evoke rapid adaptation in non-preferred directions (Ebara, Furuta et al. 2017).

Most sensory afferents, including the Vg neurons, terminate in the brainstem trigeminal complex, where somatosensory information is processed for single whiskers or integrated across multiple whiskers (Erzurumlu and Killackey 1980, Durham and Woolsey 1984, Bates and Killackey 1985). The brainstem trigeminal complex is traditionally subdivided into the spinal nucleus (SpV) and the sensory nucleus (PrV). SpV is further divided into interpolaris (SpVi), caudalis (SpVc), and

oralis (SpVo) (Ma and Woolsey 1984, Chiaia, Bennett-Clarke et al. 1991, Jacquin, Renehan et al. 1993, Lo and Erzurumlu 2016). Neurons in PrV are mostly mono-whisker responsive (Friedberg, Lee et al. 2004, Timofeeva, Lavallee et al. 2004, Kitazawa and Rijli 2018), whereas SpVi and SpVc mainly receive multi-whisker inputs (Kitazawa and Rijli 2018). It has been suggested that the function of SpVi is localization (Ahissar, Sosnik et al. 2000, Kleinfeld, Ahissar et al. 2006), while the putative function of PrV is texture decoding and processing (Adibi and Arabzadeh 2011). In general, due to the technical complexity of extracellular recordings in the brainstem and multi-whisker stimulation, the functions and encoding properties of these sub-nuclei is still poorly understood.

To overcome these technical challenges, we developed a computational model of the vibrissal system in which simulated Vg neurons receive dynamic inputs of whisker bending moments and their derivatives. The model is inspired by a paper published by Mitchinson et al. (Mitchinson, Gurney et al. 2004), who constructed a computational model of both the follicle structure and the mechanoreceptors aiming to transform the kinematics into mechanical inputs from which neural spiking could be simulated. They used static whisker deflection as stimulation; this excludes the whisker's free vibration and acceleration and limits the range of input space to neural characteristics such as angular preference and adaptation. This model approximates the Vg neurons using an leaky integrate and fire model (Burkitt 2006), which models the biological process of generating spikes in terms of the change in membrane potential. In line with this, Lottem et al. (Lottem and Azouz 2011) developed a quasi-static model that receives whisker deflections within an angular range about 20 degrees. Leaky integrate and fire model also included an adaptive current to account for the adaptation properties of the Vg neurons (Liu and Wang 2001, Benda, Maler et al. 2010). While these models are important contributions to our

understanding of neural processing in first-order sensory neurons in the vibrissal system, they are considerably limited by the quasi-static mechanics simulations that neglect essential dynamic properties of stimuli the animal typically encounters.

## A.3 Results

### A.3.1 Simulations typically converge within 1000 iterations

For a given single deflection, we first confirmed that the machine learning algorithm (sequential model-based optimization method with tree-structured Parzen estimator; see section A.5 for more details) converged to a stable solution. Figure A 1a shows the error over 1,000 iterations; the loss converges quickly around 70 steps and slowly drops until it reaches stability around 800 steps. Looking at each parameter separately (Figure A 1b), we see that $\alpha$ fluctuates ~700 times before converging, $\beta$ continues to explores its range and stabilizes around 800 iterations, $\gamma$ converges more slowly and stabilizes around 900 iterations, and $\theta$ stabilizes quickly around 300 iterations.

To determine whether 1000 iterations was sufficient for all deflections, we plotted a histogram of the number of iterations needed for each cell to find its minimal loss for all 90 fittings. Figure A 1c shows that most fits identify their minimal loss around 750 iterations; the steep fall off after 900 indicates that most fittings successfully find their minimal losses within 1000 iterations.

We fit all 90 neurons with our model. Each neuron was stimulated by around 700 deflections. Figure A 1d illustrates fits of 10 single deflections randomly sampled from the population. Those fits show a high degree of similarity to the corresponding neural recording data ($R^2 = 0.78$).
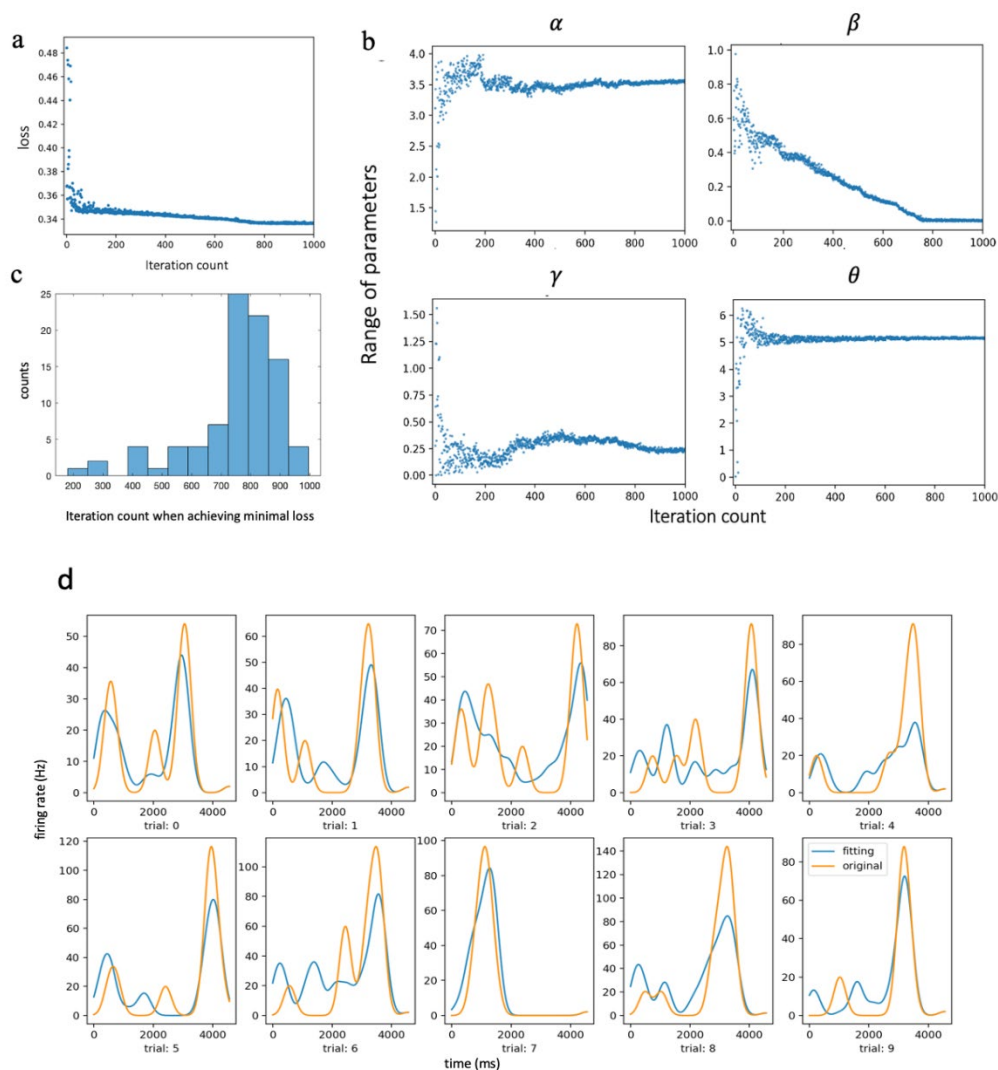
**Figure A 1. Examples of the fitting results.** (a) An example of the change in the value of the loss over 1000 iterations when fitting one neuron. (b) An example the changes in the value of the four model parameters $\alpha, \beta, \gamma, \theta$ over 1000 iterations when fitting one neuron. (c) Distribution of the number of iterations needed for the model to achieve its minimal loss over 90 simulated Vg neurons. (d) Example firing rate time series for 10 whisker deflections drawn from the population randomly without replacement. The x axis is time (ms) and the y axis is firing rate (Hz). Orange curves show the firing rate of the original recording. Blue curves show the firing rate of the fitted model.

## A.3.2 Distribution of model parameters

The distribution values of optimized parameters are shown in the histograms in Figure A 2a. The

first panel shows the distribution of $\alpha$ on a logarithmic scale. One can easily identify two clusters,

with one peak located around $10^{-3}$, with a relatively smaller population, and a second peak with a larger population located around $10^0$. We speculate that these two populations may indicate the different threshold properties of SA neurons. When the deflection magnitude or the velocity of the deflection is increased, SA neurons with lower threshold tend to fire first, meaning they are more sensitive to the magnitude of deflection than SA neurons with higher threshold.

The second panel of Figure A 2a shows that the distribution of $\beta$ also has two peaks, one concentrated around $10^{-3}$ and a second concentrated around $10^{-1}$. Since $\beta$ reflects the preference of the model to the bending moment over its derivatives, small values of $\beta$ indicate a preference for the derivatives; for these neurons, the preferred stimulation is the temporal change of the bending moments. We infer that model neurons with large $\beta$ behave closer to SA type Vg neurons, while those with smaller $\beta$ behave closer to RA type Vg neurons. The bimodal characteristic of the distribution is consistent with observations in previous research showing that the majority of the Vg neurons are classified into rapid adaptive (RA) and slow adaptive (SA) types, and that more Vg neurons are slow adaptive (Zucker and Welker 1969, Gibson and Welker 1983, Gibson and Welker 1983).

The distribution of the nonlinearity factor $\gamma$ also shows two modes (third panel in Figure A 2a), in correspondence with the empirical selection of nonlinearity parameters in Mitchinson et al. (Mitchinson, Gurney et al. 2004). The modes of the distribution are around 0.3 and 1.8. The parameter $\gamma$ may reflect a neuron's sensitivity to stimulation of smaller versus larger amplitude, which may also affect a neuron's threshold to the magnitude of deflection and adaptation.
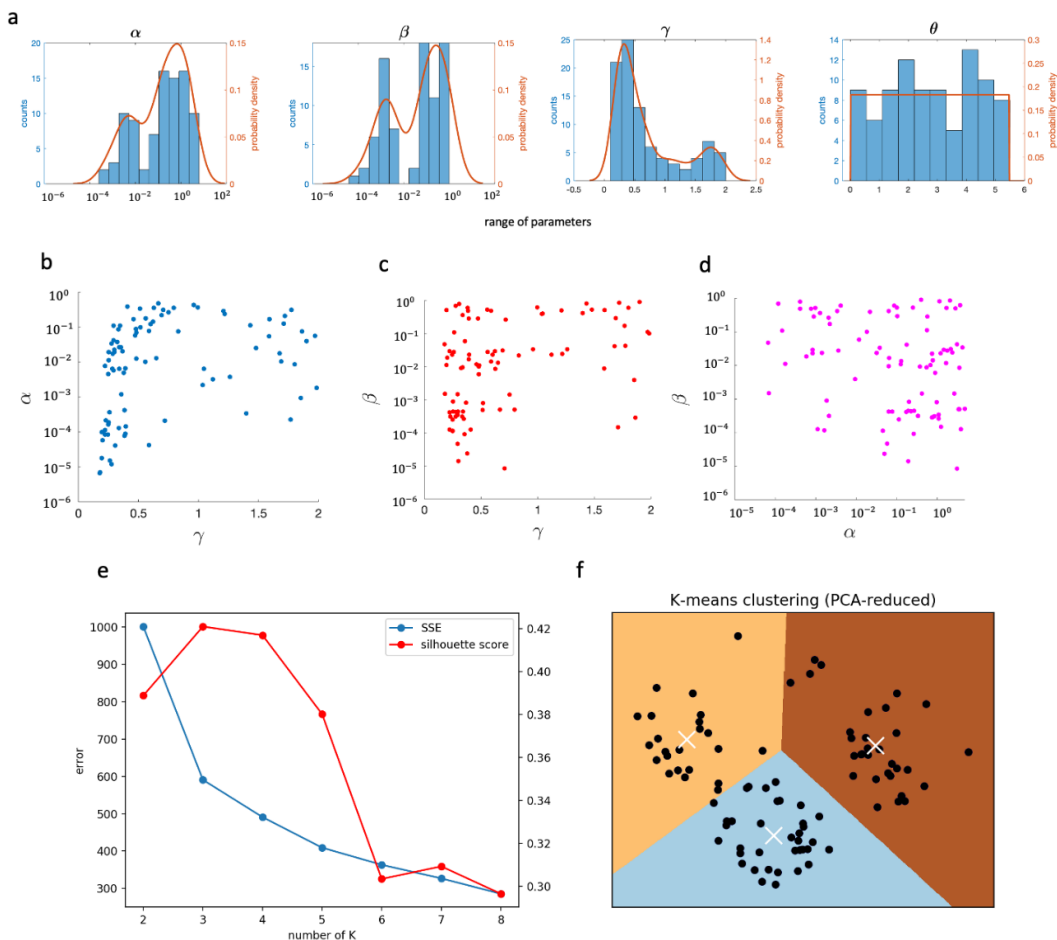
**Figure A 2. Distributions and correlations of the parameters.** (a) The histograms of values for the four model parameters $\alpha, \beta, \gamma, \theta$. Dark orange curves are fits using a Gaussian mixture model (GMM) on $\alpha, \beta, \gamma$ and a uniform distribution fit on $\theta$. (b) Shows the relationship between fitted values of $\gamma$ and $\alpha$. (c) Shows the relationship between fitted values of $\beta$ and $\gamma$. (d) Shows the relationship between fitted values of $\alpha$ and $\beta$. (e) Two metrics to identify the optimal number K of clusters in K-means clustering. The blue curve shows the decrease of SSE as K increases, with an elbow at K=3. The red curve represents the silhouette score as K increases, identifying a maximum score at K=3. (f) An illustration of PCA-reduced K-means cluster results. Neurons are classified into 3 group based on the background color.

In contrast, the parameter $\theta$ conforms to a uniform distribution (Kolmogorov-Smirnov test: n=90, D=0.072, p=0.85). This indicates the continuum of angular tuning strength in the Vg neuron population. This is consistent with Bush et al. (Bush, Solla et al. 2021), who found a uniform distribution of angular preference in actual Vg neurons.

**A.3.3 Correlations between the parameters reveal three clusters**

Since $\theta$ was found to have a uniform distribution across the population, we tried to identify the correlation between the other three parameters by looking at the scatter plots between pairs (Figure A 2b-d). In Figure A 2b, we see that $\gamma$ and $\alpha$ roughly separate the neurons into three groups, and that a similar trend occurs between $\gamma$ and $\beta$ (Figure A 2c). Little correlation or clusters are shown in Figure A 2d between parameter $\alpha$ and $\beta$.

To further investigate the emergence of the clusters we used K-means clustering (Forgy 1965), while using elbow method (Ketchen and Shook 1996) and silhouette score (Rousseeuw 1987) to determine the number of clusters K.

The results of the elbow method (SSE; blue) and the silhouette score (red) are shown in Figure A 2e. We can see that the both the elbow point and the largest silhouette score also occur for K=3. Principal Component Analysis (PCA) is used to project the data onto the two leading principal components, as shown in Figure A 2f. The data is clustered with K=3. The number of neurons within each cluster is 23, 31 and 36, respectively.

**A.3.4 The three clusters may reflect three types of Vg neurons**

To further investigate the neuron properties of the three groups, we used the cluster center as a proxy to represent each cluster and assigned their values to the model to generate three prototype Vg neurons. A step function was used as a deflection stimulus; the mechanical signals and their time derivatives are illustrated in Figure A 3ab. This stimulus was created in *WHISKiT Physics* (Zweifel, Bush et al. 2021) by using a probe to deflect a B3 whisker at constant velocity until the bar detached from the whisker; the deflection approximated a step stimulus on the y axis. The mechanical variables $M_y, M_z, dM_y, dM_z$ were used as the inputs to the three prototype neurons.
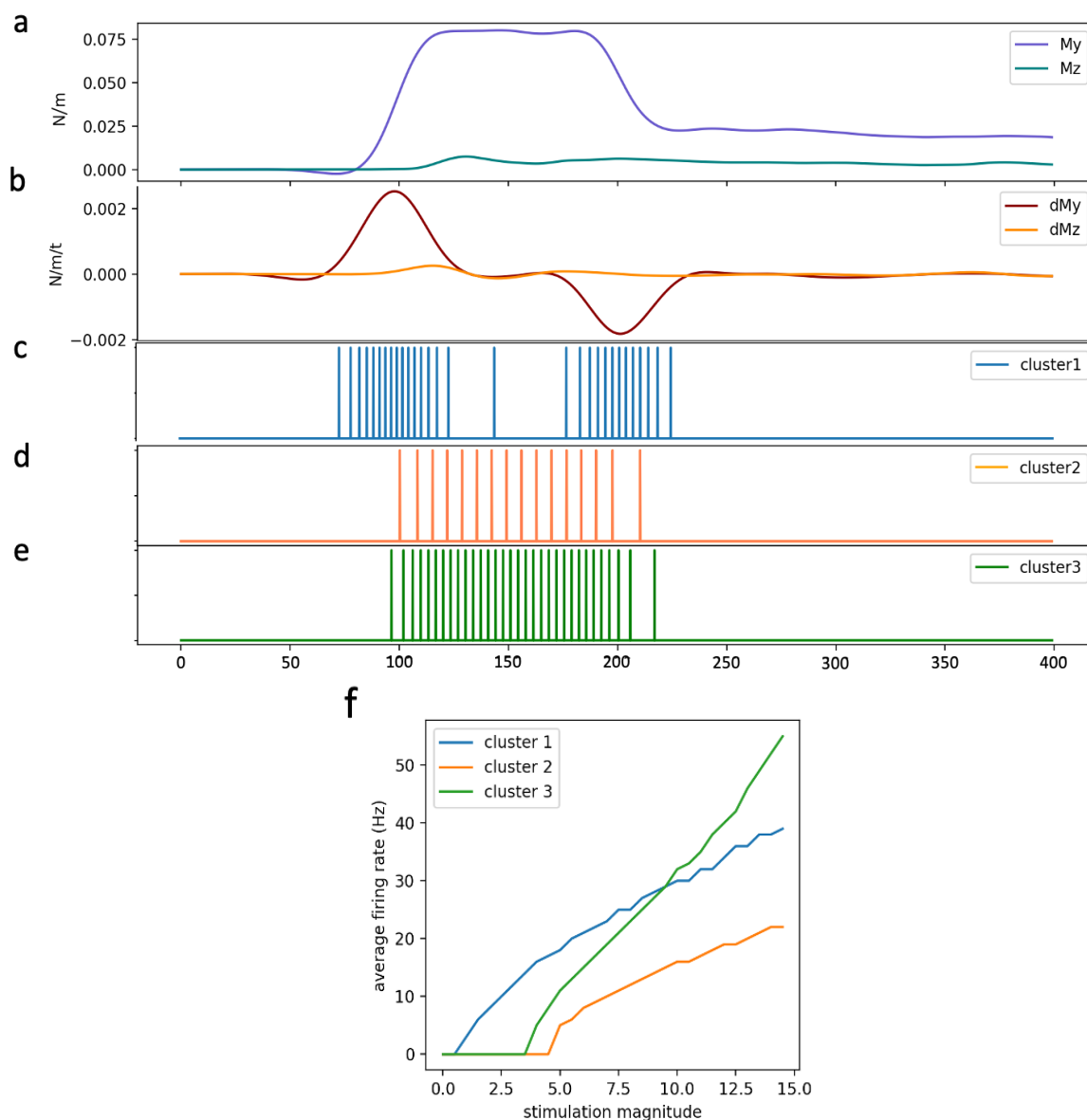
**Figure A 3. Responses of the neuron of K-means clustering centroids.** (a) Shows the values of My and Mz corresponding to a step stimulus. (b) Shows the corresponding time derivatives within the same time interval. (c)(d)(e) Show the firing pattern of the protype neuron for clusters 1, 2, 3 in response to the mechanical variables shown in (a)(b). (f) Shows the average firing rate as a function of stimulus magnitude for each prototype neuron.

The prototype neuron for cluster 1 (N1) shows rapid adaption, since it reacts to the temporal change of the stimulation (Figure A 3c). The prototype neurons for clusters 2 (N2) and 3 (N3) show slow adaption properties, since their responses are persistent throughout the deflection (Figure A 3d-e).

Note that prototype neuron N2 has a lower firing rate than prototype neuron N3. To further investigate this difference, we incremented the magnitude of the input mechanics and looked at the corresponding change in firing rate (Figure A 3f). Note that N1 has a much lower threshold, while N3 also has a lower threshold than N2. The firing rate curve for N3 in Figure A 3f exhibits a rectified-linear relationship with stimulus magnitude, while N2 and N3 increase more slowly and not linearly after threshold is exceeded.

These results validate our observation that the population of 90 Vg neurons contains three cluster groups which can be divided according to the values of $\alpha, \beta,$ and $\gamma$. We speculate that these three clusters may represent three different types of Vg neurons with different adaptation and threshold properties: N1 represents RA neurons, N2 represents high threshold SA neurons, and N3 represents low threshold SA neurons.

### A.3.5 Using a population of simulated Vg responses to predict responses in brainstem nucleus spinal trigeminal interpolaris (SpVi)

The neurons in the trigeminal nucleus interpolaris in the brainstem (SpVi) receive inputs from the Vg neurons. Having characterized the parameters for 90 Vg model neurons, we now assume that these parameter distributions can represent the whole Vg neuron population. By doing this, we can predict the firing response of a Vg neuron population to specific mechanical inputs, and thus characterize the inputs to their downstream neurons.

Here we assume that neurons in SpVi receive a principal input from one whisker, as well as inputs from eight peripheral whiskers with weaker connection, forming a center-surround receptive field including nine whiskers on a 3x3 grid (Friedberg, Lee et al. 2004). Each follicle is assumed to innervate ten Vg model neurons whose parameters are drawn from the parameter distributions of the Vg neuron model. There are no connections between the Vg neurons, and the entire network

is purely feed-forward. The proposed connectivity from Vg Neurons to SpVi neurons follows from the observation that SpVi receives multi-whisker excitatory inputs from an average of nine whiskers with a principal input from the center whisker (Friedberg, Lee et al. 2004, Timofeeva, Lavallee et al. 2004, Kitazawa and Rijli 2018).

We developed a model for SpVi neurons using a LIF neural model whose receptive field includes nine whiskers. The whisker used in this model are B2, B3, B4, C2, C3, C4, D2, D3, and D4. These whiskers experience simulated deflections generated by moving a pole across the whiskers; the pole causes the whiskers to deflect towards eight different directions on the y-z plane. The angles that characterize the directions of deflection vary in 45° steps. The angle 0° is defined by a vertical pole going across the array from rostral to caudal. The angle 90° is defined by a horizontal pole going across the array from dorsal to ventral. Figure A 4a shows the raster plot of spikes generated by a simulated population of 90 Vg neurons. The peristimulus time histogram in Figure A 4b shows that neuron responses are mostly sustained during contact, indicating that the majority of the simulated neurons are SA type.

Vg neuron spikes within its receptive field are then received by an SpVi neuron through a synapse function (Brunel and Sergi 1998, Lu, Jia et al. 2019) whose equation is:

$$Syn(t, t_0) = \frac{(t - t_0)}{\tau_s} e^{-\frac{(t - t_0)}{\tau_s}} \qquad \text{eq. 1}$$

where $\tau_s$ represents the current decay time constant and $t_0$ is the time of the spike occurrence. The Syn(t) function is applied to the spike train of each Vg neuron that provides inputs to the SpVi neuron being modeled, the outcomes are temporally summed and multiplied by a neuron-specific weight factor to obtain the input current $I_{syn}$ to the SpVi neuron:

$$I_{syn}(t) = \sum_{k=1}^{M} w_k \sum_{t_{k,spike}} Syn_k\left(t, t_{k,spike}\right) \qquad \text{eq. 2}$$
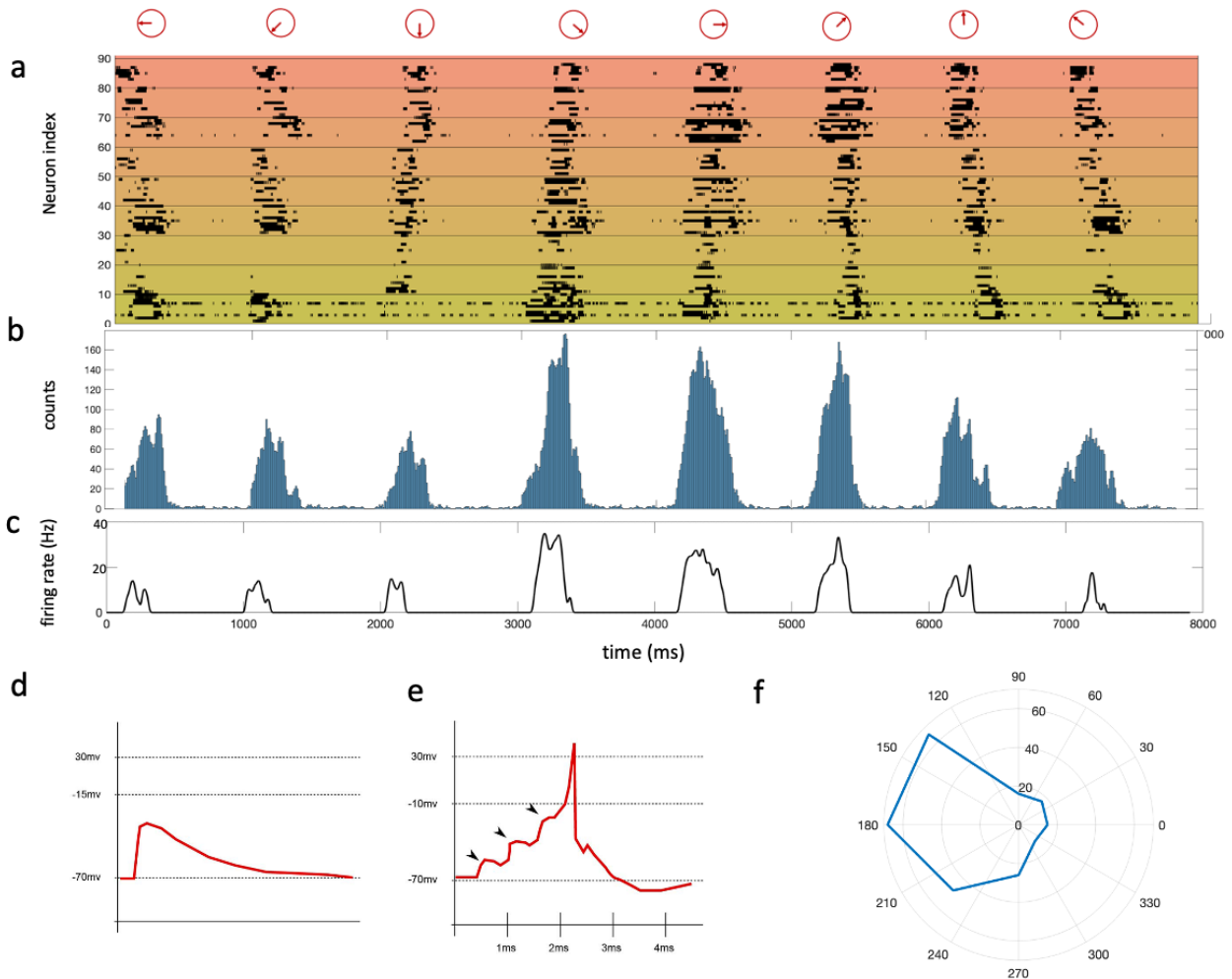


**Figure A 4. Prediction of the firing activity of a population of Vg neurons and a single SpVi neuron.** (a) A raster plot of spikes of all 90 Vg model neurons in response to whisker deflections to eight directions as shown above the raster plot. (b) Peri-stimulus time histogram (PSTH) of the Vg neuron population reacting to whisker deflections to eight directions. (c) The firing rate of the SpVi neuron which receives as inputs the firing rate of the Vg neurons within its receptive field. (d)The post-synaptic current due to one pre-synaptic spike. (e) The post-synaptic current of due to three consecutive pre-synaptic spikes, resulting in a post-synaptic spike. (f) The average response of the model SpVi neuron to deflections in all eight directions.

In equation eq. 2, $M$ is the number of Vg neurons providing input to the model SpVi neuron (here $M = 90$), $k$ is the Vg neuron index, $w_k$ is the weight factor of the $k$th Vg neuron, and $Syn_k$ is the

input current to the SpVi neuron due to each spike emitted by the $k$th Vg neuron. Figure A 4d illustrates the post-synaptic current responding to one pre-synaptic spike. One pre-synaptic spike is not sufficient to drive the current above the firing threshold. Figure A 4e illustrates the post-synaptic current responding to three consecutive pre-synaptic spikes that drive the current above the firing threshold and elicit a post-synaptic spike. Since each SpVi neuron receives one principal input from a central whisker and eight additional peripheral inputs, we assign $w_k = 0.6$ when $k = 1, 2, \ldots, 10$, describing the Vg neurons associated with the central whisker, and $w_k = 0.2$ when $k = 11, 12, \ldots, 90$. The choice of synaptic weights is supported by (Ge, Jia et al. 2018, Lu, Jia et al. 2019) while the authors tested different values. The results of our simulations did not depend strongly on the values assigned to these synaptic weights.

The firing rates of the model SpVi neuron as a function of time is shown in Figure A 4c. Deflections in eight different directions elicit different shapes of firing pattern. Half of them exhibit a two-peak shape.

The amplitudes of firing rates also vary from 30-80 Hz in a manner that depends on the direction of deflection. We plotted the radar graph in Figure A 4f shows the average firing rate for each of the eight directions of deflection. This SpVi neuron shows a preferred direction of 180°, corresponding to the deflections caused by a vertical pole moving from caudal to rostral. This preference in caudal-rostral direction is supported by results published in Kaloti et al. (Kaloti, Johnson et al. 2016).

### A.4  Discussion

We constructed a computational model of the Vg neuron in rat's primary vibrissal system; the neuron receives 2D bending moments and their derivatives as inputs. The model contains four free

parameters which represent four properties of each neuron: threshold ($\alpha$), adaptation ($\beta$), nonlinearity ($\gamma$), and angular preference ($\theta$). We fitted the model with extracellular recordings of 90 Vg neurons, each in response to around 700 deflections in various conditions. We found that (1) the firing patterns of model neurons model show a high similarity to neural recordings; (2) the distribution of all parameters are continuous, in agreement with previous findings (Zucker and Welker 1969, Gibson and Welker 1983, Gibson and Welker 1983, Muniak, Ray et al. 2007, Bush, Solla et al. 2021); (3) the distributions of $\alpha$, $\beta$, and $\gamma$ are similar in shape as those obtained by (Gibson and Welker 1983, Gibson and Welker 1983), who showed the distribution of 51 Vg neurons of rats in vivo based on their adaptation, threshold, and reaction to amplitude of velocity. The distributions of $\alpha, \beta,$ and $\gamma$ exhibit a bimodality suggestive of the presence of separate clusters that can be further characterized using K-means clustering with K=3; (4) the three model neuron prototypes resulting from K-means clustering can be characterized as a low threshold SA neuron, a high threshold SA neuron, and a RA neuron; (5) the distribution of $\theta$ can be regarded as a uniform distribution, in agreement with (Bush, Solla et al. 2021), whose model also found a uniformly distributed angular preference across the Vg neuron population.

Given the mechanics dataset, the model fitting results of 90 Vg neurons agree with physiological experiments (Kenton, Kruger et al. 1971, Wellnitz, Lesniak et al. 2010) as well as with previous computational modelling results (Mitchinson, Gurney et al. 2004, Lottem and Azouz 2011) based on 2D bending moments and their derivatives as inputs. In addition, we constructed an SpVi model neuron innervated by 9 whiskers arranged in 3x3 square grid on the whisker pad; there were 10 model Vg neurons associated with each whisker in the grid, each providing synaptic input to the model SpVi neuron. Given eight directional stimuli, the SpVi neuron showed a strong response to

whisker deflections caused by a vertical pole moving in the caudal to rostral direction, consistent with (Kaloti, Johnson et al. 2016).

By fitting the Vg model to match the firing rate trace elicited by free whisker deflection under various conditions, our model successfully identifies the population distributions of some of the most important properties of realistic Vg neurons and is able to predict the response of a neuron in the SpVi, a downstream structure in which neurons receive multi-whisker input during passive sensing. The centers of the three clusters in parameter space suggest a classification of Vg neurons into three classes: low threshold SA, high threshold SA, and RA.

### A.4.1 Level of approximation of data

We smoothed the mechanics data before feeding into the Vg model neurons by using a low-pass filter with a 20Hz cut-off frequency. This procedure filters out the both noise and whisker resonance frequency (Mehta and Kleinfeld 2004), while preserving enough input information to fit the Vg model. Although some type of mechanoreceptors such as Pacinian corpuscles are able to detect vibration of up to 1500 Hz and Meissner corpuscles can detect a 20-200 Hz input (Das and Alagirusamy 2011), most Vg neurons that detect steady deformation and displacement of the follicles rely on Merkel cells and Ruffini endings. These receptors are sensitive to vibrations below 50 Hz (Y.I. Li 2006); Merkel cells only transduce 5-15 Hz vibrations (Das and Alagirusamy 2011). Researchers believe that receptors sensitive to higher frequencies may serve the function of sensing texture and fluid flow (Neimark, Andermann et al. 2003, Wolfe, Hill et al. 2008). The choice of cutoff frequency was determined empirically. Though we successfully classified the model neurons into three distinct group, using a 20Hz cut-off frequency potentially would in reality prevent certain types of receptors from spiking and providing input to the corresponding Vg neurons.

In the Methods section, we explain our procedure of convolving spikes with a Gaussian filter to compare firing patterns across instead of directly using distances between spike trains. Studies have found that receptors use sub-millisecond temporal coding for texture sensing in rats (Montemurro, Panzeri et al. 2007), while there is evidence that receptors tend to use population-rate coding for localization (Zucker and Welker 1969). Therefore, the loss function used to fit the Vg model was based on distance between smoothed continuous firing rates (Kass, Ventura et al. 2003).

The goal of using firing rates to estimate the loss is two-fold: first, the Gaussian filter provides a smooth firing rate more amenable to analytical efforts than the spiking neural signal. Second, the Gaussian filter denoises the signal by separating meaningful fluctuations in the firing rate from the noise introduced by the spiking process. The window size $\sigma$ of the Gaussian filter is usually chosen *ad hoc* (Kass, Ventura et al. 2003, Park, Seth et al. 2013). In neural engineering, the choice of $\sigma$ is often greater than 50 ms (Cunningham, Gilja et al. 2009). Here, since the time duration of most deflections is less than 2s, we chose $\sigma = 20$ ms to include more temporal features in the firing rate.

## A.4.2 Interpretation of Vg model parameters and their distributions

The distribution of $\alpha$ is similar to the results in (Gibson and Welker 1983), where the authors plotted the histograms for 51 Vg neurons in rats based on bending magnitude and angular velocity thresholds. In the article, magnitude threshold was defined as "the minimum pulse magnitude that evokes a response on 50% of the trials presented." Occasionally, thresholds were found to drift slightly with time; in such cases, they determined and recorded the lowest threshold that occurred within a reasonable time period. The article also defined a velocity threshold as the minimum angular change within any one second interval. In our simulations, the stimuli are step signals of bending moments; the higher magnitude of bending moments requires higher change in velocity.

Thus, we argue that the parameter $\alpha$ measures both the bending magnitude and velocity change. In either case, there consistently exists two types of Vg neurons in the population based on their thresholds.

Also, the distribution of $\beta$ is similar to the results in (Gibson and Welker 1983), where the authors plotted the histograms for 51 Vg neurons in rats based on their adaptation index. Gibson et al.(Gibson and Welker 1983) defined the adaptation index as "the ratio of mean discharge rate during the period between 0.2 and 0.3 sec to that during the first 0.1 sec of stimulation." This definition ignored the spikes that happen after the removal of the stimulation (offset response), characteristic of RA neurons that react to temporal changes in the amplitude of stimulation. Here, we used the degree of preference to the derivative inputs driving the model neuron as a measure of adaptation that measures the excess firing rate during both stimulus onset and offset.

The nonlinear responses of Vg neurons are usually fitted using three possible choices: a  logarithm function, a power law, and a linear function (Gibson and Welker 1983). Among these, power laws include a linear function and provide a good approximation to the logarithm function within specific ranges. In our model, the parameter $\gamma$ described this degree and type of nonlinearity. The function is linear for  $\gamma=1$, power law for $\gamma > 1$, and approximates a logarithmic function f $1 > \gamma > 0$. However, Kenton et al. (Kenton, Kruger et al. 1971) also found an asymmetrical relationship between stimulus intensity and spike rates during 'ascending' series and 'descending' series; this asymmetry is not captured by our model.

### A.4.3 Implementation of adaptation

Adaptation is usually approximated and implemented in one of four ways.

(1) The first way is to insert an adaptive current (AC) in the LIF neuron model (Wang 1998). During stimulation, the adaptive hyperpolarizing current increases and stabilizes to a value large enough to prevent the membrane potential from reaching threshold. This strategy is observed in many neurons; the AC is an approximation of different ion channels. This method is biologically accurate, but it includes two additional parameters and requires considerably long computation times.

(2) The second way is to include a dynamic threshold (DT) in the LIF neuron mode; (Benda, Maler et al. 2010). During stimulation, the firing threshold increases and stabilizes to value chosen such that it takes the model neuron longer to depolarize its membrane potential to the new threshold. The major pitfall of this method is that although the threshold increase can temporarily prevent the neuron from firing, the neuron can still fire if stimulation persist for a long enough period of time. This results in a scenario where the post-adaptation firing rate cannot be zero.

(3) The third way is to use an adaptation filter (AF) (Mitchinson, Gurney et al. 2004). This filter is implemented on the signal instead of the neuron. The input signal is processed by a temporally decaying function that diminishes it over time. Although the computational cost of this method is negligible, it only operates at stimulus onset. Another downfall is that the filter does not "reset"; the method treats a whole trial containing hundreds of deflections as one deflection and causes the model to ignore deflections at the end of the trial.

(4) The fourth way is to adjust the relative proportion of the temporal derivative input and the persistent input. A Vg neuron that is RA type prefers to react to the temporal change of the stimulus, while SA type neurons prefer a sustained stimulus. Though this is not so good at

imitating the actual adaptation behavior in neurons, it captures both onset and offset response with negligible computational time.

### A.4.4 The model exhibits a weak ability to generalize when applied to a validation set of deflections

To measure the generalization ability of the models, we further tested the fitted models on a validation set. A comparison between the optimal training set loss and the validation set loss is shown in Figure A 5. The average validation loss is significantly larger (Wilcoxon signed rank test, p=0.004), which indicates poor generalization ability of the fitted model. To identify if the model is underfitted or overfitted, more analysis in terms of how the loss evolves during training is required.
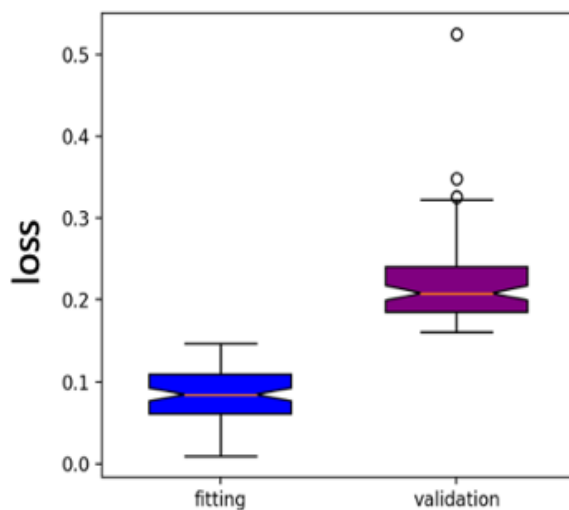


**Figure A 5. Boxplots of the losses of 90 neurons on the testing set and validation set.** Boxplots of the losses of 90 neurons on testing set (blue box) and on validation set (purple box). Lower and upper box boundaries show 25th and 75th percentiles, respectively; the line inside box shows the median; lower and upper error lines show the 10th and 90th percentiles, respectively; hollow circles show data outside the 10th to 90th percentiles interval.

**A.4.5 Selection of model inputs: why only including bending moments?**

Birdwell et al. (Birdwell, Solomon et al. 2007) first discovered four variables at the whisker base that provide sufficient information to Vg neurons. These variables are angular position, angular velocity, bending moment, and time derivative of the bending moment. Later on, Huet et al. (Huet, Rudnicki et al. 2017) highlighted the importance of the bending moment and its derivative along with the forces detected at the whisker base in representing the deflection mechanics. Recently, Perterson et al. (Petersen, Colins Rodriguez et al. 2020) argued that the bending moment is a primary driver of contact-related mechanotransduction. All these findings emphasize the significance of the bending moment and its time derivative. Our results further confirm that bending moment and its time derivative are sufficient to induce the model to exhibit a similar spiking behavior as that of real Vg neurons, as well as to induce the angular preference of SpVi neurons.

**A.4.6 Deficiencies of the model**

As mentioned previously, the model is limited in predicting certain aspects of the response of real Vg neurons:

(1) Inaccurate representation of adaptation. A more biologically realistic adaptation function needs to be constructed to represent dynamic reactions to stimulation in a computationally efficient manner. The approach might include combining the time derivatives term to the adaptive current while using a more efficient algorithm.

(2) The asymmetric relationship between stimulus intensity and spike rates during "ascending" and "descending" series is not included.

(3) Lack of a relation between adaptation and preferred angle results in Vg model neurons that fail to capture that real Vg neurons exhibit completely different adaptation property when

the whisker is deflected in different direction. This feature could be introduced by adding a preferred angle for the derivative term in the input, without affecting the input term for bending moment.

(4) Bending moments and their time derivatives along the y and z axis may not contain sufficient information about whisker deflections to provide accurate predictions of Vg neuron responses. This could be addressed by including additional inputs such as forces and rotation angles (Bush, Solla et al. 2021). A more dynamic model would also have to include the Vg neuron response to mechanics along the whisker longitude (Stuttgen, Kullmann et al. 2008).

(5) The model lacks information about physiological attributes of Vg neurons in rats such as average resting potentials, firing threshold, and membrane constant. We urge for more intracellular recordings in response to deflections to provide additional data that can be incorporated in the model.

## A.5 Methods

### A.5.1 Data Collection

All data were obtained by Bush et al. (Bush, Solla et al. 2021). As described in their paper, neural recordings were obtained from 90 whisker-responsive Vg neurons in 22 female, Long-Evans rats between 3 to 6 months in age. Animals were anesthetized by ketamine-xylazine hydrochloride combination. Recordings were made with single tungsten electrodes. Whiskers not associated with the neuron being recorded from were trimmed or held against the skin, and surrounding fur was removed to make space for the stimulation of recorded whiskers.

Single Vg neuron spikes were recorded in response to deflections delivered manually using a hand-held graphite probe. During stimulation, high-speed video (300 or 500 fps) was used to record

whisker motion from two perpendicular views (Figure A6). The deflection was delivered in 8 cardinal directions, at 2-3 distances out along the whisker length. Deflections and neural activity were recorded for an average of ~500s per neuron, with an average of 684 whisker deflections per neuron across all conditions. These procedures yielded a dataset of ~67,000 deflections across all recorded neurons.

Three-dimensional (3D) whisker shape and stimulus contact point were reconstructed from the two-camera video tracking. All signals, including spike times, were quadratic-interpolated and binned at 10kHz.
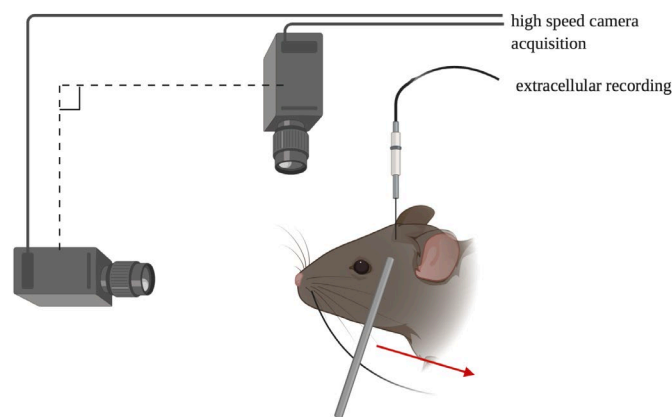


**Figure A 6. A schematic of the experimental setup.** The activity of a Vg neuron is recorded using a tungsten electrode while its corresponding whisker is manually deflected by a graphite probe. The movement of the whisker is traced by two perpendicularly located high-speed cameras.

### A.5.2 Simulations of mechanosensory input in response to whisker deflection

The whisker deflection and corresponding neural response data were recorded in a previous study; the available tracking data of the deflected whisker and deflecting probe were insufficient to allow for accurate reconstruction of the whisker and probe in simulation. Therefore, we approximated the mechanics generated at the whisker base by using an average model of the whisker array

already incorporated in the simulation software *WHISKiT Physics* (Zweifel, Bush et al. 2021).

From the experimental tracking data, we extracted the whisker identity, the three-dimensional

velocity vector of the probe stimulating the whisker, as well as the point and time of contact

between whisker and probe. Based on these data, we simulated the experiment by moving the

whisker according to the velocity profile of the probe during contact, after which the whisker

oscillated freely as determined by the simulated dynamics. For each whisker and corresponding

neuron, the simulations were performed for ~700 deflections; the three-dimensional mechanical

signals generated at the whisker base were recorded in terms of moments ($M_x$, $M_y$, $M_z$) and forces

($F_x$, $F_y$, $F_z$) with millisecond precision. Finally, the simulated mechanics were upsampled to match

the sampling frequency required to simulate the neural spikes.

### A.5.3 Neural model

Inspired by the model of Mitchinson, Gurney et al. 2004 (Mitchinson, Gurney et al. 2004), we

developed a leaky integrate-and-fire (LIF) model to simulate the firing characteristics of a Vg

neuron. The inputs to the model are two bending moments ($M_y$ and $M_z$, shown in Figure A 7), and

their derivatives. The output of the model is a simulated spike train. We assumed that the

mechanoreceptors receive only mechanical moments at the whisker base, and thus neglected the

complexities of the mechanics of the follicle and surrounding tissue. A schematic overview of the

model is illustrated in Figure A 7.

In whisker-centered coordinates (Bush, Solla et al. 2021), the time series of bending moments

consisting of y-axis ($M_y$) and z-axis ($M_z$) components and their derivatives ($\frac{dM_y}{dt}, \frac{dM_z}{dt}$) are filtered

with a 2nd order low pass filter with a cutoff frequency = 20Hz to minimize the effect of noise.
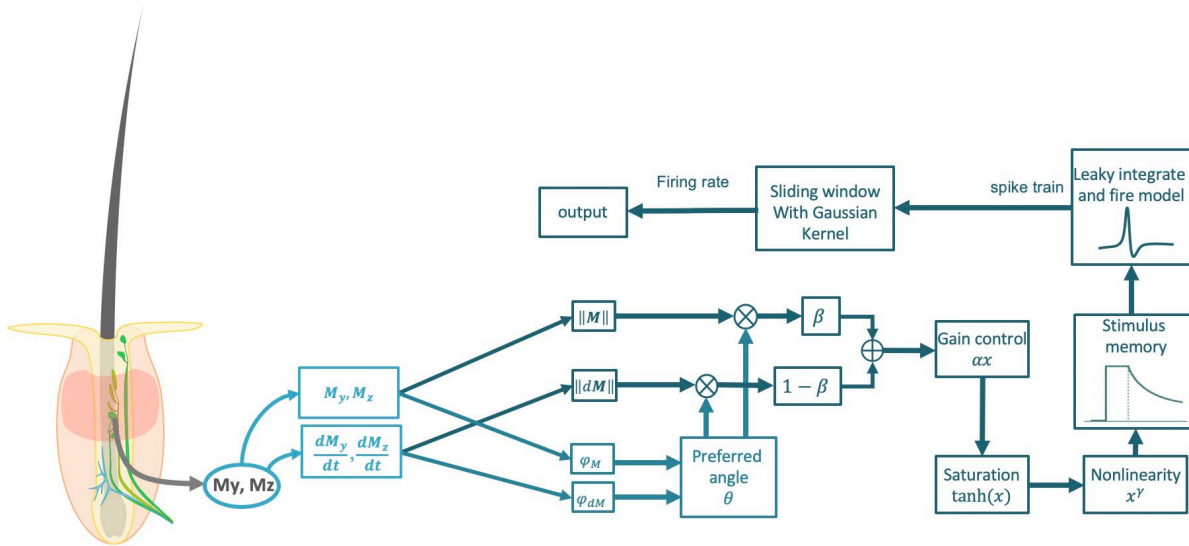
**Figure A 7. A flow chart of the Vg neuron model.** The angle $\varphi_M$ between $(M_y, M_z)$ and the angle $\varphi_{dM}$ between $(\frac{dM_y}{dt}, \frac{dM_z}{dt})$ are measured relative to the assumed preferred angle $\theta$ to obtain a direction dependent gain that acts on the norm of the bending moment and the norm of its derivative. The results are added together proportionally to $\beta$ and multiplied by a gain control $\alpha$. The signal is then transformed sequentially by processing units representing saturation, nonlinearity $\gamma$, and stimulus memory; the result is regarded as the electrical input current that drives a conventional leaky integrate and fire model. Additional details about the various components can be found in text.

Vg neurons are direction selective (Shipley 1974). Therefore, the direction of the mechanical response was calculated for the moments $(\varphi_M)$ and their derivatives $(\varphi_{dM})$.

$$\varphi_M = \arctan\left(\frac{M_y}{M_z}\right) \qquad \text{eq. 3}$$

$$\varphi_{dM} = \arctan\left(\frac{dM_y}{dM_z}\right) \qquad \text{eq. 4}$$

To include direction selectivity in the neural model, we used a circular gain function with a maximally effective angle $\theta$ and a directional-dependent gain $\zeta$ ranging from zero to one (eq. 5 and eq. 6). We assumed that every Vg neuron intrinsically has a strong directional preference and set the maximal gain to one for all Vg neurons. The circular function yields the angle dependent gain $b_M$ for the norm of the moment, controlled by the angular difference between $\theta$ and $\varphi_M$, and the angle dependent gain $b_{dM}$ for the norm of the moment derivative, controlled by the angular difference between $\theta$ and $\varphi_{dM}$:

$$b_M = \zeta \cos(\varphi_M - \theta) \qquad \text{eq. 5}$$

$$b_{dM} = \zeta \cos(\varphi_{dM} - \theta) \qquad \text{eq. 6}$$

From $b_M$ and $b_{dM}$, the directional response to the moment $\boldsymbol{M}_{pref}$ and the derivative $\boldsymbol{dM}_{pref}$ were calculated by multiplying the circular function by the corresponding $L_2$ norm $|\boldsymbol{M}|$ and $|\boldsymbol{dM}|$ as follows.

$$\boldsymbol{M}_{pref} = |\boldsymbol{M}| \frac{\sqrt{b_M{}^2 - b_M}}{2} \qquad \text{eq. 7}$$

$$\boldsymbol{dM}_{pref} = |\boldsymbol{dM}| \frac{\sqrt{b_{dM}{}^2 - b_{dM}}}{2} \qquad \text{eq. 8}$$

$$|\boldsymbol{M}| = \sqrt{M_y{}^2 + M_z{}^2} \qquad \text{eq. 9}$$

$$|\boldsymbol{dM}| = \sqrt{\left(\frac{dM_y}{dt}\right)^2 + \left(\frac{dM_z}{dt}\right)^2} \qquad \text{eq. 10}$$

These directional responses were combined using the parameter $\beta$ which determines the mixing proportion between $\boldsymbol{M}_{pref}$ and $\boldsymbol{dM}_{pref}$.

$$V = \beta \boldsymbol{M}_{pref} + (1 - \beta)\boldsymbol{dM}_{pref} \qquad \text{eq. 11}$$

To control the cell's response range, we used a global gain control $\alpha$ such that $W = \alpha V$. A non-linear function was used to control the cell's saturation behavior, $X = \tanh(W)$, which limits firing rates to below 500Hz. A nonlinearity $Y = X^{\gamma}$ is added to control the response profile of the Vg neuron to fit the observations. For $\gamma > 1$, this filter amplifies strong signals and dims weak signals, whereas for $\gamma < 1$, the filter squashes strong signals and magnifies weak signals. A stimulus memory unit is added to represent that Vg neurons continue to fire for a certain period after the stimulus is removed. For every time step $i$ there is:

$$Z_i = \begin{cases} Y_i, & Y_i > \lambda Z_{i-1} \\ \lambda Z_{i-1}, & otherwise \end{cases} \qquad \text{eq. 12}$$

$$\lambda = e^{\frac{-F_S}{\tau}} \qquad \text{eq. 13}$$

Here, $F_s$ is the time step of integration. In practice, $F_s$ will be regarded as sample period globally chosen to be 0.1ms. We set the value of $\lambda = 5\ ms$. The distributions and ranges of the model parameters shown in Table A 1are based on both Mitchinson (Mitchinson, Gurney et al. 2004) and observation. A basic assumption is that these parameters are treated as intrinsic properties of each neuron. Hence, for each neuron, there exists a set of optimal parameters whose initial values are drawn from their distributions.

**Table A 1. Choices of range and distribution of the parameters.**

| $\theta$ | $\alpha$ | $\beta$ | $\gamma$ |
|---|---|---|---|
| Unif(0, $2\pi$) | Unif(0, 4) | Unif(0, 1) | Unif(0, 3) |

The time series Z forms the input current $I_{input}$ to a leaky integrate-and-fire (LIF) model (Tal and Schwartz 1997). The membrane potential of the neuron is modeled as follows:

$$\tau_m \frac{dv}{dt} = -(v - v_{rest}) + (I_{input} + I_{bias})R_m \qquad \text{eq. 14}$$

where $v$ is the membrane potential, $v_{rest}$ is the resting potential, $\tau_m$ is the membrane time constant, and $R_m$ is the membrane leak resistance. When current is injected to the neuron, the membrane charges and $v$ increases. When $v$ reaches threshold $v_{th}$, a spike is generated and recorded, and simultaneously $v$ is reset to $v_{reset}$. $I_{bias}$ is a constant bias. The LIF neuron is a single compartment model that neglects spatial structures and ion channels. The LIF neuron is leaky because the current contributions that charge the membrane potential decay with a time constant $\tau_m$. Table A 2 gives the parameters that characterize the LIF neuron, based on (Burkitt 2006).

**Table A 2. Choices of parameters in the LIF model.**

| $\tau_m$ | $v_{rest}$ | $v_{reset}$ | $v_{th}$ | $R_m$ | $I_{bias}$ |
|---|---|---|---|---|---|
| 5 ms | -70 mV | -80 mV | -55 mV | $2.6 \times 10^6$ $\Omega$ | 0.1 nA |

Spike trains $S(t)$ are generated based on the membrane potential $v(t)$ and transformed into firing rates $F(t)$ for further comparison to the responses of real Vg neurons. A gaussian sliding window with $\sigma = 20$ ms is used to calculate $F(t)$ from $S(t)$. The gaussian filter has the form of $G(t) = \frac{1}{\sqrt{2\pi}\sigma} e^{-\frac{t^2}{2\sigma^2}}$, and it is applied through convolution:

$$F(t) = (S * G)(t) = \sum_{m=0}^{N} S(m)G(t-m) \qquad \text{eq. 15}$$

An example of the transformation from bending moments and their derivatives to neural firing rates is illustrated in Figure A 8.
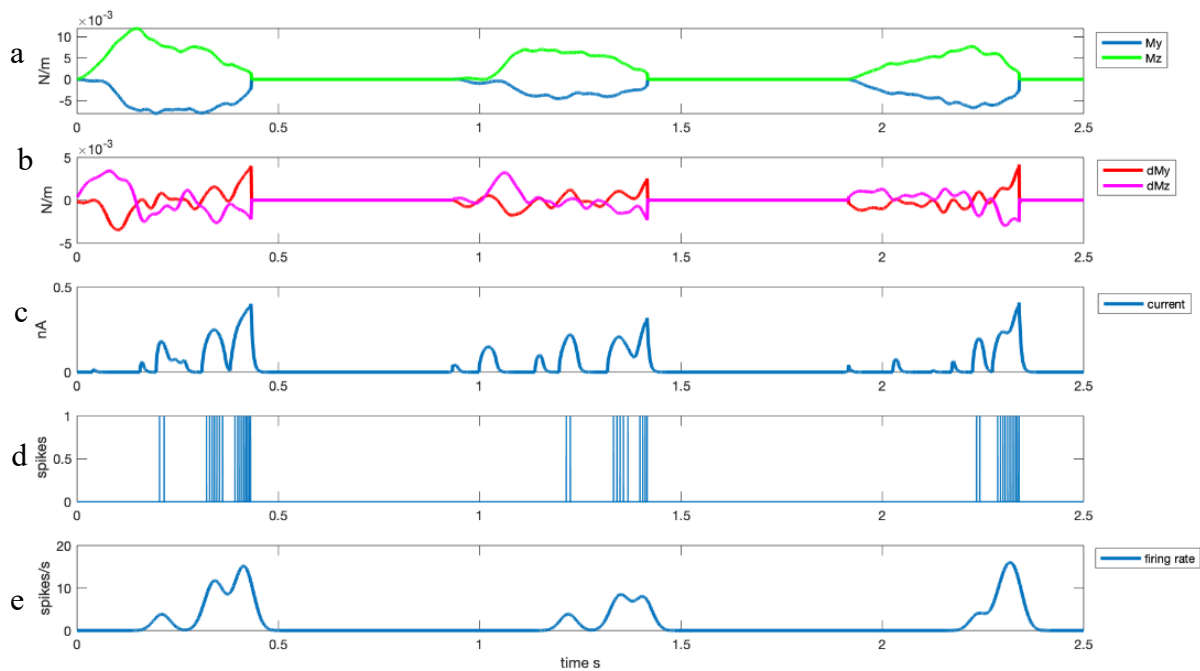


**Figure A 8. Transformation of mechanical signals into firing rates: an example.** (a), (b) Show the time series of bending moments and their derivatives, respectively, during a period of 2.5 seconds. (c) Shows the time series of the current that provides the input to the LIF model of the Vg neuron. (d) Shows the spike trains generated by the LIF model neuron. Each vertical bar represents a spike. (e) Shows firing rate time series calculated by convolving the spike train in (d) with a gaussian window.

### A.5.4 Model optimization

After acquiring mechanical data from *WHISKiT Physics* (Zweifel, Bush et al. 2021) and combining it with the firing rate data recorded on the corresponding Vg neurons, we tuned the four parameters characterizing each of the 90 Vg neurons using a sequential model-based optimization (SMBO) method with tree-structured Parzen estimator (TPE) (Mashlakov, Tikka et al. 2019). The algorithm was implemented in the python package *hyperopt*.

The initial set of parameters were drawn from the original parameter space $\mathcal{X} = \{\theta \in (0, 2\pi), \alpha \in (0, \ 4), \beta \in (0, 1), \gamma \in (0,3)\}$ (Table A 1). For a given setting of the model parameters, the simulated firing rates were compared to experimental firing rates to generate a loss value. The loss was used by the regression algorithm to generate another set of parameters more likely to yield a better fit with lower loss. The new set of parameters provided be the initial setting for the next iteration. In our simulation, the total number of iterations was set to 1000, based on (Bergstra, Komer et al. 2014, Li, Gunther et al. 2018).

The training and validation sets were created such that for each neuron, 50 deflections were randomly sampled without replacement from all the deflections of that neuron for the validation set. The rest of deflections were used as training set.

### A.5.4.1 Loss function

The loss function measures the dissimilarity between the model output $\hat{y}$ and corresponding actual experiment data $y$; here this metric is constructed by combing a normalized sum of square differences (NSSD) (Akbarinia and Cloez 2019) and with a cosine dissimilarity (CosD) (Sohangir and Wang 2017). The resulting loss function is:

$$NSSD = \sqrt{\frac{\sum_{i=1}^{N}(y_i - \hat{y}_i)^2}{N * fr_{max}}} \qquad \text{eq. 16}$$

$$CosD = (1 - (\sum_{i=1}^{N} y_i \hat{y}_i) / \sqrt{\sum_{i=1}^{N} y_i^2 * \sum_{i=1}^{N} \hat{y}_i^2})/2 \qquad \text{eq. 17}$$

$$CosD = \frac{1}{2}\left[1 + \frac{(\sum_{i=1}^{N} y_i \hat{y}_i)}{\sqrt{\sum_{i=1}^{N} y_i^2 * \sum_{i=1}^{N} \hat{y}_i^2}}\right]$$

$$loss = (1 - \mu) * NSSD + \mu * CosD \qquad \text{eq. 18}$$

NSSD in eq. 16 is the normalized squared difference between two time series at each time step $i$; in the denominator, $N$ is the total number of time steps and $fr_{max}$ is the maximum firing rate. This metric is comparable to the Mahalanobis distance (De Maesschalck, Jouan-Rimbaud et al. 2000), and provides an effective way to normalize the sum of squared differences. The CosD in eq. 17 represents the cosine similarity. It is based on calculating the cosine of the angle between $y$ and $\hat{y}$ as vectors, followed by a scaling that restricts its value to the [0,1] interval. The two contributions, NSSD and CosD, are respectively weighted by the factors $(1 - \mu)$ and $\mu$ ($\mu \in (0, 1)$), to control the ratio between the two metrics for the final loss (eq. 18). The parameter $\mu$ was set to 0.3. A smaller loss value indicates a higher similarity between $y$ and $\hat{y}$.

As described in Eq 18, $\mu$ is the weight of the CosD term in the loss function. The value of $\mu$ has a strong effect on fitting performance. We fit the model with a loss function with different values of $\mu$ in the [0,1] interval on 5 randomly sampled deflections from the recorded dataset . The fits for three different values of $\mu$ are shown in Figure A 9a-c.

For $\mu = 1$ there is only the CosD component in the loss function (Figure A 9c); in this case the model output is able to capture the trend of how the firing rate changes, but grossly overestimates the firing rate amplitude. In contrast, for $\mu = 0$ there is only the NSSD component in the loss function, the model output is able to capture the overall firing rate amplitude but fails to capture the trends of firing rate change (Figure A 9a). A balanced combination of CosD and NSSD allows the algorithm to fit both the mean value as well as the trend of firing rate change (Figure A 9b). Figure A 9d shows how $\mu$ changes the fitted value of CosD and NSSD. As $\mu$ increases, the proportion of CosD increases; the models prefer the CosD term in the loss function, resulting in
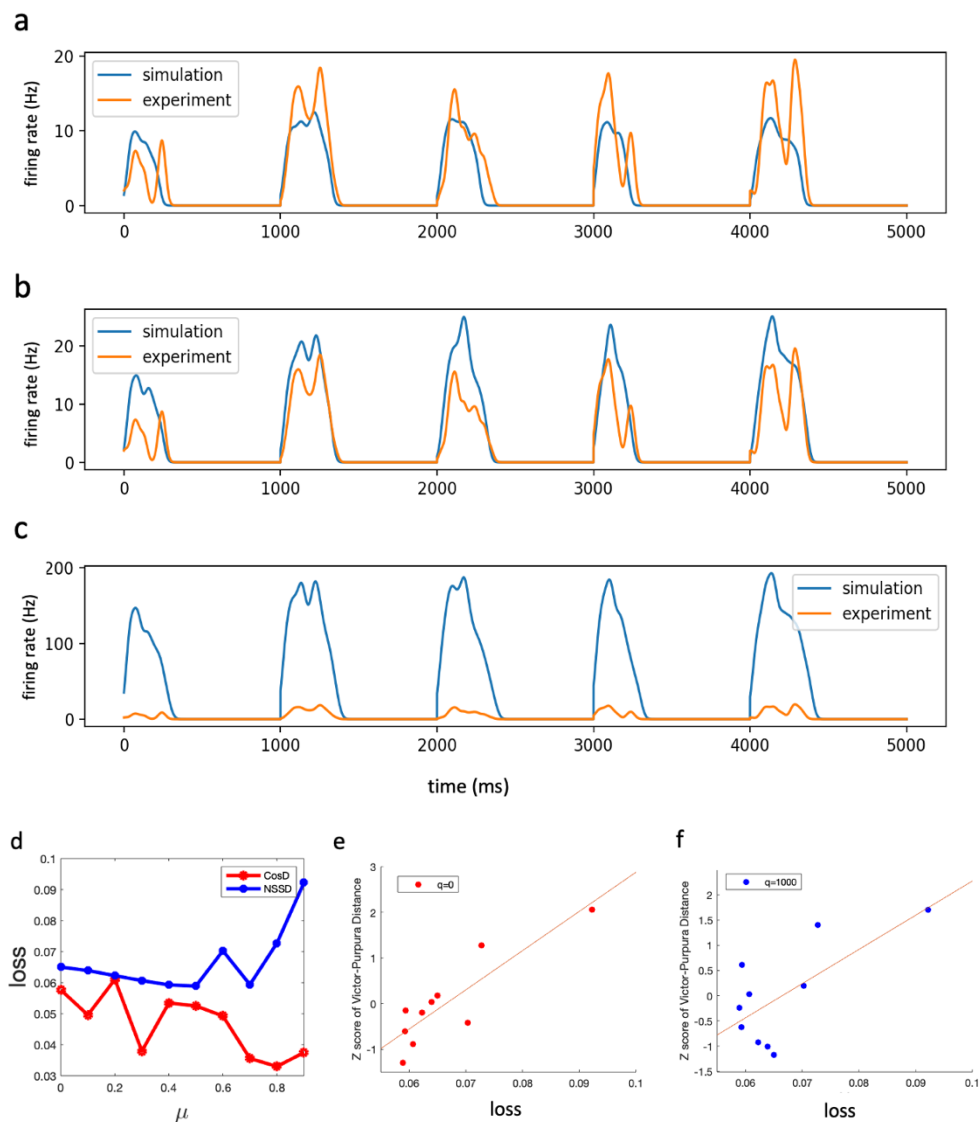
**Figure A 9. Effects of the parameter in loss function.** (a)(b)(c) Show the firing rate time series for a period of 5000 ms. The orange curve shows the recorded firing rate. The blue curve shows the fit using the loss function with (a) $\mu = 0$, (b) $\mu = 0.3$, (c) $\mu = 1$. (d) The fitted values of CosD (red curve) and NSSD (blue curve) as $\mu$ inceases from 0 to 1. (e) Shows the correlation between the fitted loss function and the Z score of Victor-Purpura Distance for q=0 (see text for a definition of q). (f) Shows the poor correlation between the fitted loss function and the Z score of Victor-Purpura Distance for q=1,000.

the decrease of CosD. The increase in $\mu$ also helps to decrease the fitted value of the NSSD term,

but for $\mu$ is larger than 0.7, the influence of the NSSD term in the loss function is very attenuated

and its fitted value increases dramatically as the fitting results in models that prefer to capture the

trend of the firing rates while neglecting their means. This graph indicates that values around $\mu$=0.3 result in a loss function able to balance out the goals of fitting the trend of firing rates versus fitting the mean firing rates.

### A.5.4.2 Spike distance vs loss function

To further evaluate the loss function chosen here, we compared the fitted values of the loss function to the spike distance between the experimental data and model simulation results. The most common metric to measure distance between spike trains is the Victor-Purpura distance (Victor and Purpura 1996, Victor and Purpura 1997). This metric defines the distance between two spike trains in terms of the minimum cost of transforming one spike train into the other by means of three basic operations: spike insertion (cost 1), spike deletion (cost 1), and shifting a spike by some interval $\Delta t$ (cost q$|\Delta t|$). The cost q per time unit sets the time scale of the analysis. For q=0, the metric is equal to the difference in spike counts, while for large q the distance approaches the number of non-coincident spikes, as it becomes more favorable to delete and reinsert all non-coincident spikes rather than shifting them. By increasing the cost q, the Victor-Purpura distance is transformed from a rate distance to a temporal distance. For the system of interest here, researchers believe that mechanoreceptors within the follicle at the whisker's base encode information by firing rate, and that accurate temporal coding is less likely to occur due to the low information capacity of spike transduction (Juusola and French 1997). Thus, we expect Vg neurons to transduce information with rate coding. We set q=0; the comparison of the two metrics in Figure A 9e a shows a positive correlation between the Victor-Purpura distance and the loss function ($R^2 = 0.86$). As we increase q to q=$10^3$, the correlation markedly decreases ($R^2 = 0.53$) (Figure A 9f).